

Research Paper

On the cratonization of the Arabian-Nubian Shield: Constraints from gneissic granitoids in south Eastern Desert, Egypt



Ali A. Khudier^a, Jean-Louis Paquette^b, Kirsten Nicholson^c, Åke Johansson^d, Tyrone O. Rooney^e, Sadiq Hamid^a, Mohamed A. El-Fadly^a, Loretta Corcoran^f, Shawn J. Malone^c, Mohamed Ali Abu El-Rus^{a,*,1}

^a Geology Department, Faculty of Science, Assiut University, 71516, Egypt

^b Université Clermont Auvergne, CNRS, IRD, OPGC, Laboratoire Magmas et Volcans, F-63000 Clermont-Ferrand, France

^c Ball State University, Department of Geological Sciences, 117 Fine Art Building, Muncie, IN 47306, USA

^d Department of Geosciences, Swedish Museum of Natural History, Box 50007, SE-104 05 Stockholm, Sweden

^e Department of Geological Sciences, Michigan State University, East Lansing, MI 48824, USA

^f Notre Dame University, Department of Civil & Environmental Engineering & Earth Sciences, 156 Fitzpatrick Hall, Notre Dame, IN 46556, USA

ARTICLE INFO

Article history:

Received 25 August 2020

Received in revised form 1 January 2021

Accepted 10 January 2021

Available online 26 January 2021

Editor: C.J. Spencer

Keywords:

Arabian-Nubian Shield (ANS)

Cratonization

Fractional crystallization

Partial melting

Subduction zones

Tonalite-Trondhjemite-granodiorite (TTG)

ABSTRACT

The Shaitian granite complex (SGC) spans more than 80 Ma of crustal growth in the Arabian–Nubian Shield in southeast Egypt. It is a voluminous composite intrusion (60 km²) comprising a host tonalite massif intruded by subordinate dyke-like masses of trondhjemite, granodiorite and monzogranite. The host tonalite, in turn, encloses several, fine-grained amphibolite enclaves. U–Pb zircon dating indicates a wide range of crystallization ages within the SGC (800 ± 18 Ma for tonalites; 754 ± 3.9 Ma for trondhjemite; 738 ± 3.8 Ma for granodiorite; and 717 ± 3.2 Ma for monzogranite), suggesting crystallization of independent magma pulses. The high positive ϵ_{Nd}^t (+6–+8) indicate that the melting sources were dominated by juvenile material without any significant input from older crust. Application of zircon saturation geothermometry indicates increasing temperatures during the generation of melts from 745 ± 31 °C for tonalite to 810 ± 25 °C for trondhjemite; 840 ± 10 °C for granodiorite; and 868 ± 10 °C for monzogranite. The pressure of partial melting is loosely constrained to be below the stability of residual garnet (<10 kbar) as inferred from the almost flat HREE pattern ((Gd/Lu)_N = 0.9–1.1), but >3 kbar for the stability of residual amphibole as inferred from the significantly lower Nb_N and Ta_N compared with LREE_N and the sub-chondrite Nb/Ta ratios exhibited by the granitic phases. The inverse relation between the generation temperatures and the ages estimates of the granitoid lithologies argue against a significant role of fractional crystallization. The major and trace element contents indicate the emplacement of SGC within a subduction zone setting. It lacks distinctive features for melt derived from a subducted slab (e.g. high Sr/Y and high (La/Yb)_N ratios), and the relatively low MgO and Ni contents in all granite phases within the SGC suggest melting within the lower crust of an island arc overlying a mantle wedge. Comparison with melts produced during melting experiments indicates an amphibolite of basaltic composition is the best candidate as source for the tonalite, trondhjemite and granodiorite magmas whereas the monzogranite magma is most consistent with fusion of a tonalite protolith. Given the overlapping Nd–Sr isotope ratios as well as several trace element ratios between monzogranite and tonalite samples, it is reasonable to suggest that the renewed basaltic underplating may have caused partial melting of tonalite and the emplacement of monzogranite melt within the SGC. The emplacement of potassic granite (monzogranite) melts subsequent to the emplacement of Na-rich granites (tonalite–trondhjemite–granodiorite) most likely suggests major crustal thickening following arc collision and amalgamation into the over thickened proto-crust of the Arabian–Nubian microcontinent. Eventually, after complete consolidation, the whole SGC was subjected to regional deformation, most probably during accretion to the Saharan Metacraton (arc–continent collisions) in the late Cryogenian–Ediacaran times (650–542 Ma).

© 2021 Elsevier B.V. This is an open access article under the CC BY license (<http://creativecommons.org/licenses/by/4.0/>).

1. Introduction

The continental crust ultimately derives from the subduction and melting of oceanic lithosphere over many millions of years, and related magmatism in convergent margins (Arndt, 2013; Cawood, Hawkesworth, & Dhuime, 2013; Hart, Wolde Gabriel, Walter, &

* Corresponding author.

E-mail address: mmahmad@aun.edu.eg (M.A.A. El-Rus).

¹ Permanent address: Geology Department, Faculty of Science, Taiz University, Taiz, Yemen.

Mertzman, 1989). Within a subduction zone setting, juvenile island-arc crust is formed and transformed into mature continental crust involving processes of collision and accretion of older crustal blocks. These processes are accompanied by folding, thrusting, metamorphism, and partial melting of crust (Yarmolyuk et al., 2012), eventually leading to the compositional differentiation of crust and formation of the stable upper and lower crust (i.e. cratonization of the continental lithosphere; Weaver & Tarney, 1983; Zhai, 2011). During this cratonization process, the mantle provides the necessary energy and materials. The most salient feature of the cratonization of continental crust is the emplacement of tonalite-trondhjemite-granodiorite/granite (TTG) associations (e.g. Zhang et al., 2012). These associations represent a volumetrically important component in Archean terranes (e.g. Jahn, Gikson, Peucat, & Hickman, 1981); however, they are also recorded in many post-Archean terranes (e.g. Martin, Smithies, Rapp, Moyen, & Champion, 2005; Zhang et al., 2009). There is little agreement on the melting sources of the TTG association. While some researchers proposed basaltic material previously underplated beneath thickened crust as the main melting source (e.g. Bédard, 2006; Halla, 2020; Smithies, 2000; Van Kranendonk, 2010), others believe that melting of the subducted oceanic slab at convergent plate boundaries is the main melting source (e.g. Abdel-Rahman, 2019; Martin, 1995; Martin & Moyen, 2002; Rapp, Shimizu, & Norman, 2003). Furthermore, the precise petrogenetic relationship between the rock units within TTGs is not always straightforward. For example, some researchers propose that the tonalite-trondhjemite-granodiorite associations with high-Na content are derived from subducted oceanic crust, while potassium granites are derived from pre-existing continental crust (e.g. Huang, Polat, & Fryer, 2013; Watkins, Clemens, & Treloar, 2007). Other researchers, in contrast, propose that the post-Archean, high-Na granitoids and high-K granites of the TTG associations may form by partial melting from different source rocks in a unified tectonic setting (Zhai, 2011). Further disagreement exists over whether partial melting occurred under fluid-present (e.g. Laurie, Stevens, & Van Hunen, 2013) or fluid-absent (e.g. Moyen & Stevens, 2006; Rapp et al., 2003) conditions. However, discriminating between these (or other) geodynamic scenarios requires accurate linkage of formation of the TTGs with the pressure-temperature (P-T) conditions in the Earth over which sufficient volumes of melt of appropriate composition can be generated from suitable source rocks since the whole Earth was progressively cooling down and the Earth's heat production decreased profoundly by as much as 50% from 4.0 to 2.5 Ga (Brown, 1986).

The emplacement of the Shaitian tonalitic-trondhjemitic-granodioritic-monzogranitic association in the south Eastern Desert of Egypt is one of the best examples of crustal evolution in the Arabian-Nubian-Shield (ANS) as it emplaced over period more than 80 Myr. The present paper presents a comprehensive geochronological, isotopic and geochemical (bulk major and trace elements) characterization of the rock units of the Shaitian granitic complex (SGC), which is the oldest rock unit recognized in the north ANS (e.g. Akaad & Noweir, 1980; El-Gaby, 1975; El-Gaby, List, & Tehrani, 1988; Khudeir, Abu, Hoinkes, Mogessie, & El-Gaby, 1996). The purpose of this study is to (1) discuss the emplacement of TTG-like magmas during evolution of the Arabian-Nubian Shield during the Neoproterozoic, (2) gain new insights into the petrogenesis of the post-Archean TTGs and assess the possible petrogenetic link between Na-rich members and K-rich members within these TTGs, (3) compare the post-Archean TTGs with Archean TTG and modern adakites, and (4) provide new constraints on the processes by which the oceanic lithosphere differentiated into the ANS during the Neoproterozoic. Our findings suggest that the Na-rich members within the TTG-like association in the Arabian-Nubian Shield have resulted from melting of basaltic magmas that crystallized at the crust-mantle boundary (i.e. underplating basaltic layers) during the orogeny, whereas the K-rich members have been generated by subsequent fusion of the solidified Na-rich members at deeper crustal levels. The emplacement of potassic granite melts subsequent to the emplacement of

Na-rich granites most likely defines a major period of crustal thickening that followed arc collision and amalgamation forming the proto-crust of the Arabian-Nubian microcontinent.

2. The Arabian-Nubian shield

The ANS is a clear example of continental crust having originated as a result of assembly and accretion of the island arc terrains (800–670 Ma; Johnson et al., 2011) that formed within the Mozambique Ocean generated from the fragmentation of the Rodinia supercontinent during the Tonian to early Cryogenian (870–800 Ma; Andresen, Abu El-Rus, Myhre, Boghdady, & Corfu, 2009; Johnson et al., 2011; Johansson, 2014). These island arc terranes typically have Neoproterozoic Nd model ages close to their crystallization ages, demonstrating the juvenile origin of the crust (e.g. El-Fadly, Hamid, Abu-El-Rus, & Khudeir, 2018; Johnson et al., 2011; Stern, 2002). U-Pb zircon ages demonstrate their formation over a long-time span (870–710 Ma; Johnson et al., 2011; Fig. 1a). Terranes within the Mozambique Ocean converged and amalgamated as a result of an intraoceanic arc-arc collision and ultimately collision of the arc with the Saharan Metacraton during the assembly of eastern and western Gondwana in the late Cryogenian-Ediacaran (650–542 Ma; Johnson et al., 2011). Most boundaries between assembled terranes are high-strain shear zones that commonly contain dismembered ophiolites and refolded recumbent folds (e.g. Andresen et al., 2010; El-Fadly et al., 2018; El-Gaby et al., 1988). The shear zones are widely interpreted as sutures that formed at the time of terrane amalgamation (e.g. El-Gaby et al., 1988; Khudeir, Abu El-Rus, El-Gaby, & El-Nady, 2006; Khudeir, Bishara, El-Tahlawi, Abu El-Rus, & Bogdadi, 2006; Khudeir, Abu El-Rus, El-Gaby, El-Nady, & Bishara, 2008), although some of them have been modified by later strike-slip movements (e.g. Kusky & Matsah, 2003).

3. Geological setting

The SGC forms an E-W elongate mass covering ~60 km², overthrust from the SE by the Pan-African Gardan ophiolitic mélange (GOM), which builds up an allochthonous tectonic sequence formed of variably deformed slices or nappes of schistose meta-andesites, metabasalts, andesitic and dacitic meta-pyroclastics, meta-agabbros, tuffaceous meta-sediments and rare marls (Fig. 1b). The ophiolitic mélange rocks near the contact with the SGC are locally hybridized with granitic melt. Irregular to subrounded enclaves, up to few kms in diameter, from the country rocks are found within the proximal zone of the SGC, indicating that the intrusion of the SGC into the GOM occurred prior to the regional overthrusting. The SGC was progressively diaphthorized into protomylonites, mylonites and ultramylonites. The mylonitic foliation strikes NE-SW and dips at 20°–45° NW, while the associated lineation trends NW and plunges at 5°–40° NW.

Detailed field work shows that the SGC together with the GOM were subsequently folded into NW trending major anticlinal folds or culmination structure coeval with the intersection of the NE limb by a set of NW trending sinistral faults running parallel to those of the Najd fault system (Stern, 1985). These deformational structures are quite similar to those occurring in the Meatiq, Hafafit and El-Sibai core complexes in the ANS, which owe their origin to (1) the development of fault bend-faults (Greiling et al., 1988, 2) orogen-parallel crustal extension (Fritz et al., 2002; Khudeir et al., 2008; Loizenbauer et al., 2001), (3) emplacement within regional domal structures (Ibrahim & Cosgrove, 2001) followed by extension parallel to their fold axes (e.g. Sibai dome; Fowler, Khamees, & Dowidar, 2007). Occasionally, the planes of the dissecting sinistral faults are locally filled with elongate metabasalt fragments characterized by distinct schistose structure running conformably with that of the nearby GOM slices. On the other hand, the foliation and lineation measurements recorded on the western limb are generally few since most of the western limb was down-faulted

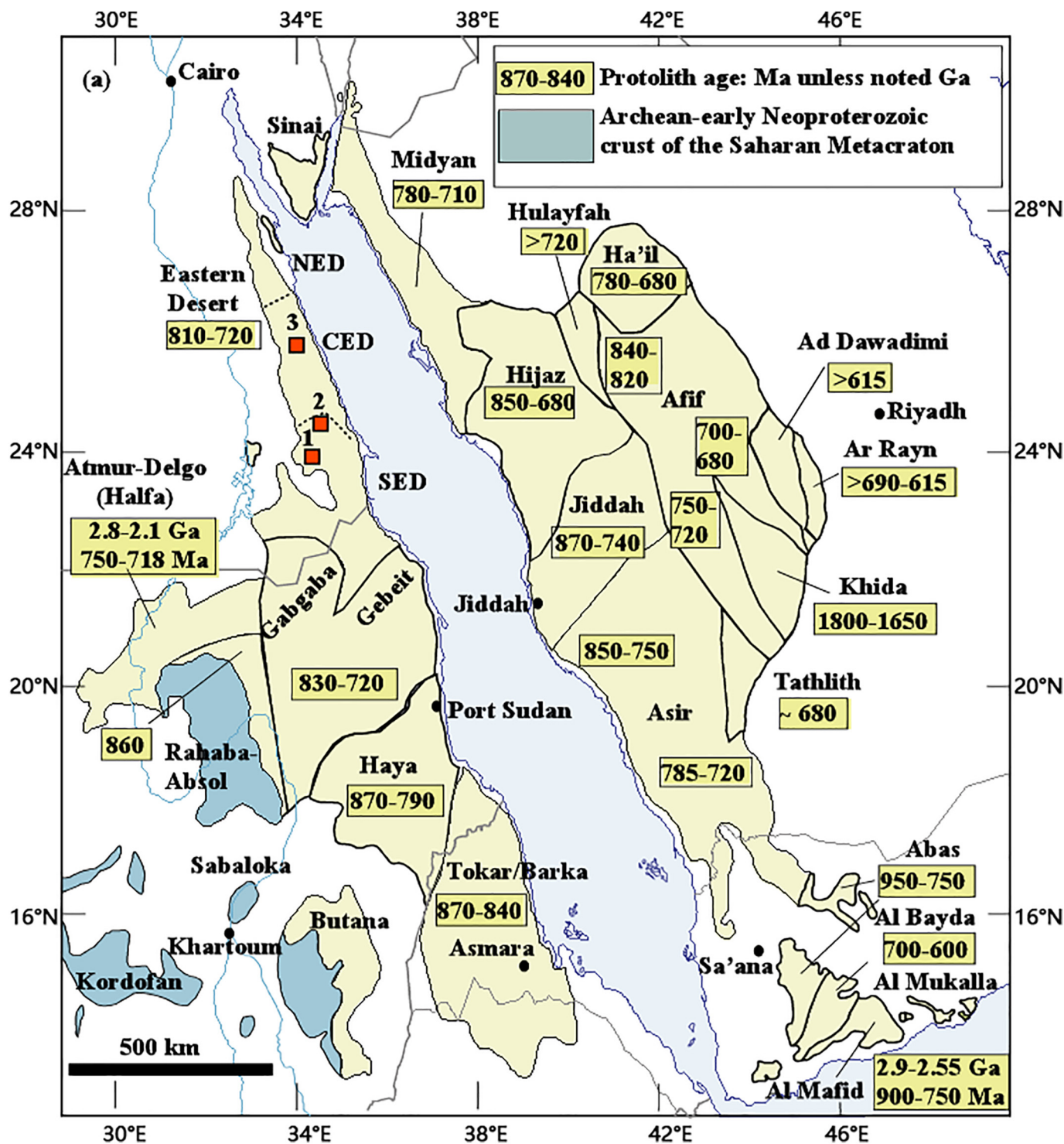
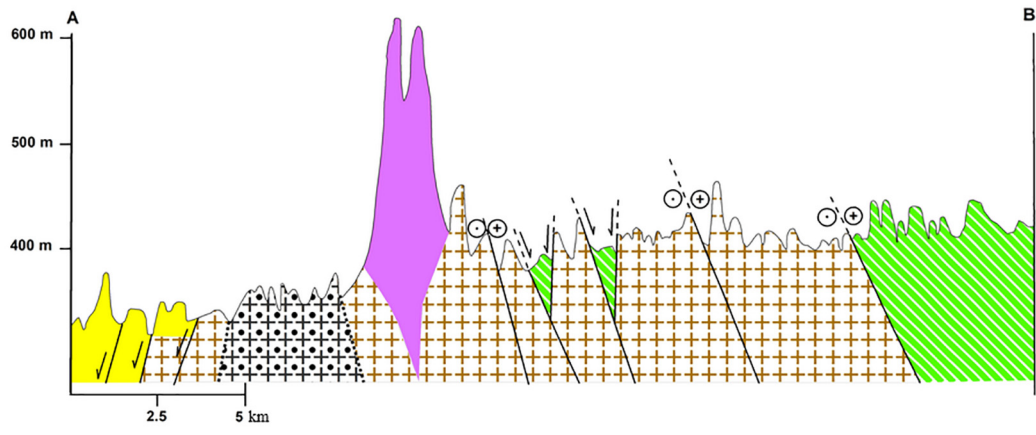
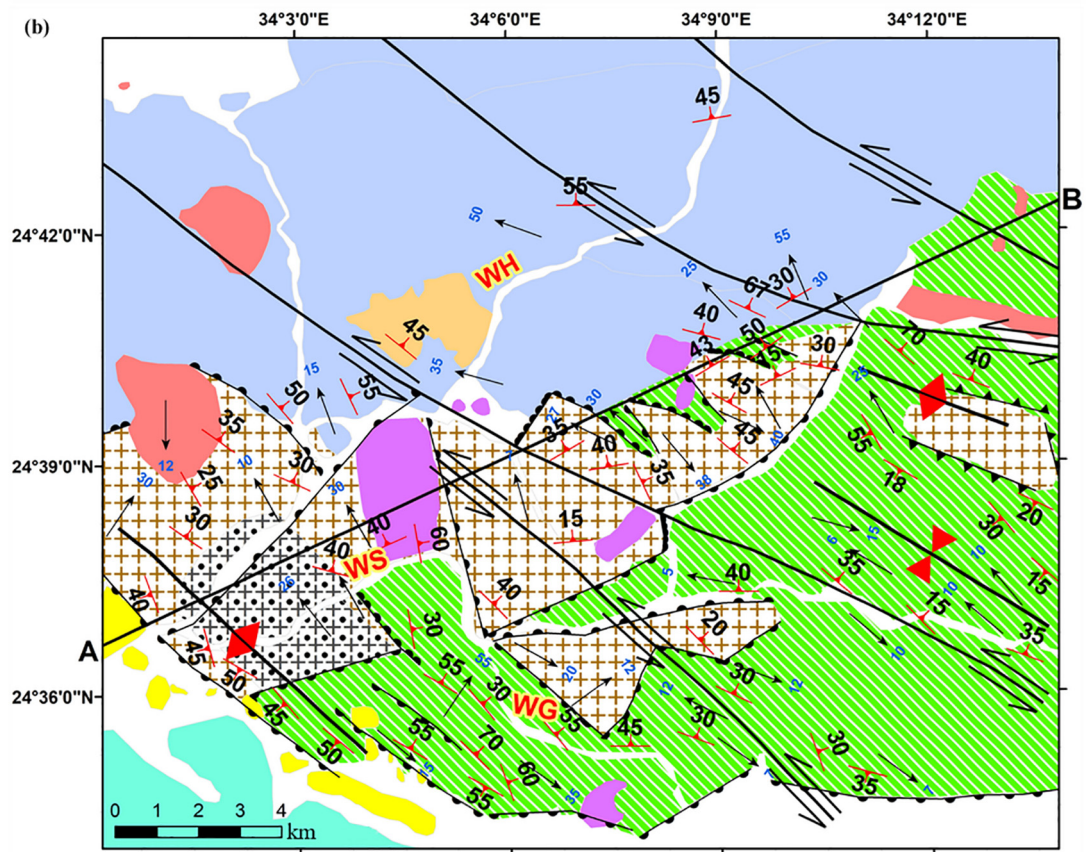


Fig. 1. (a) Sketch map showing the tectono-stratigraphic terranes comprising the Arabian-Nubian Shield (ANS) (after Johnson et al., 2011). Small red boxes labelled 1, 2 and 3 indicate the locations of gneissose granitoids of the Shait (present study), Hafafite and Meatiq areas, respectively. NED, CED and SED are the Northern Eastern Desert, Central Eastern Desert and Southern Eastern Desert terranes in the Nubian Shield in Egypt; respectively. (b) Geological map of the Shaitian granite complex (SGC) modified after El-Gaby and El-Aref (1977) and El-Kalioubi and El-Ramly (1991).

prior to the non-conformable deposition of the overlying Cretaceous bedded Nubian sandstone.

The SGC complex is a tonalite massif, consisting of a coarse-grained mesocratic core containing several microgranular mafic enclaves of various sizes (10 cm in diameter) and degrees of assimilation, and an outer leucocratic rim intruded by small, non-mappable lensoidal and dyke-like masses of trondhjemite, granodiorite and monzogranite (Fig. 2a, b). The contact between the core and rim of the tonalite massif within the

SGC is usually gradational, but locally may be sharp. The core of the tonalite massif is mildly deformed, and frequently dissected by non-oriented fractures occasionally filled by secondary quartz, chlorite, and epidote or calcite associations (Fig. 2c, d). The most extensive exposure of mesocratic core granites occurs in the western part of the SGC (Fig. 1b). The outer zone of the SGC is leucocratic and characterized by fine- to medium-grained tonalite, with pervasive gneissosity and lineation structures (Fig. 2e, f). It is dissected by a set of NW trending sinistral



Legend


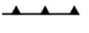

















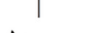
- | | | | | |
|---|------------------------------------|------------------|--|--|
|  | Alkali granite | WS = Wadi Shait |  | Thrust fault |
|  | Dokhan volcanics | WH = Wadi Hamash |  | Withdrawing block during strike-slip fault |
|  | Hamash granodiorite | WG = Wadi Gardan |  | Approaching block during strike-slip fault |
|  | Shait granite core | |  | Synform |
|  | Shait granite margine | |  | Antiform |
|  | Gardan ophiolite | |  | Foliation |
|  | Alluvium deposits | | | |
|  | Trachyte | | | |
|  | Natash volcanics | | | |
|  | Nubian sandstone | | | |
|  | Sinistral strike-slip fault | | | |
|  | Normal faul | | | |
|  | Direction of tectonic transport | | | |
|  | Hanging wall block of normal fault | | | |

Fig. 1 (continued).

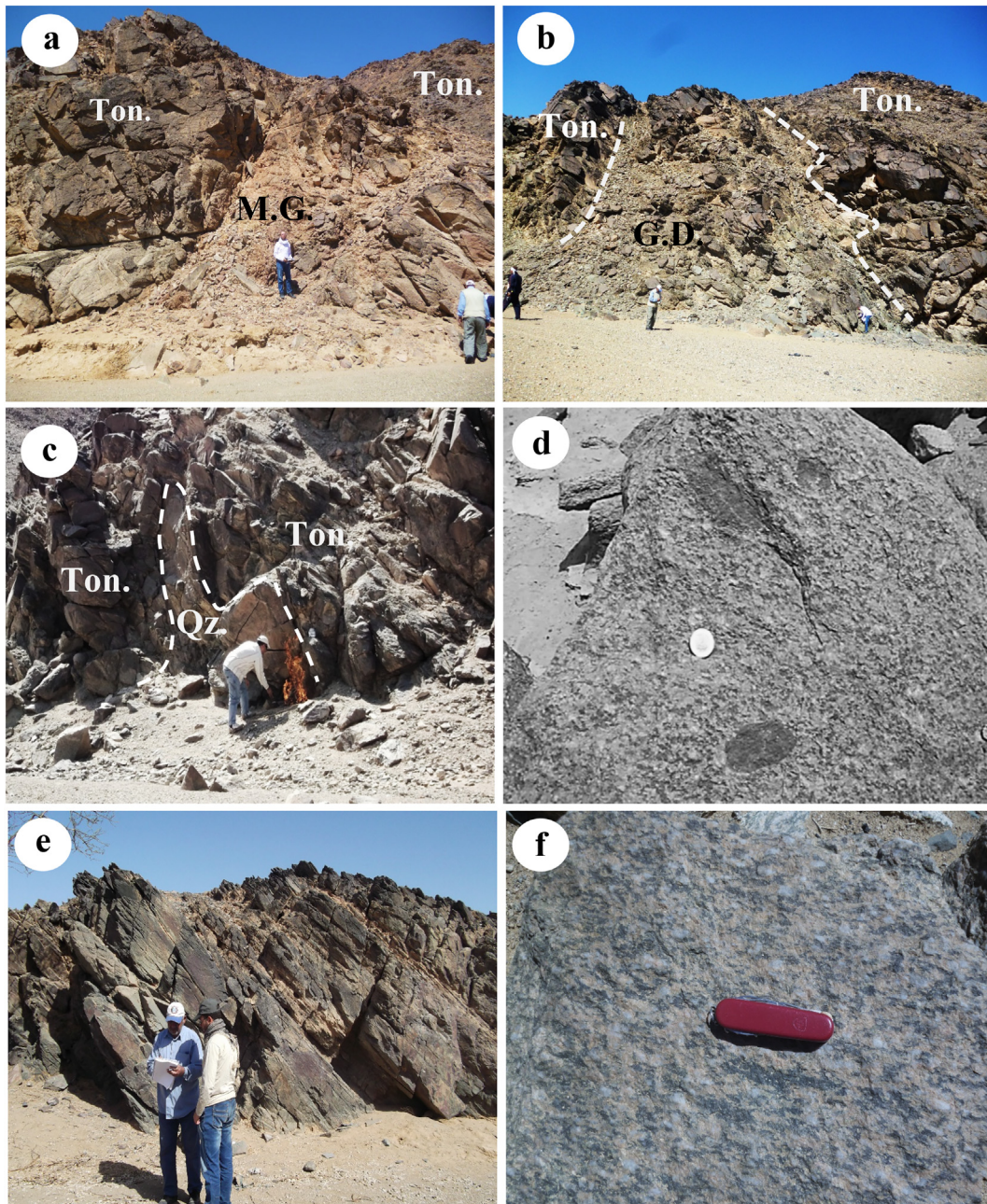


Fig. 2. (a, b) General views showing the intrusions of the monzogranite (M.G.) and granodiorite (G.D.) dyke-like masses into the outer leucocratic rim of tonalites (Ton.). (c) Mildly deformed core of the tonalite massif that is dissected by multiple fractures filled with secondary quartz. (d) Microgranular mafic enclaves of various sizes enclosed within the coarse-grained core of tonalite massif. (e) Highly deformed rim of the tonalite massif that ductility sliced toward the NE dipping of along the Wadi Shait. (f) A close-up view showing the SE plunging pervasive gneissose structures exposed in the outer rim of the tonalite massif along Wadi Shait.

shear zones along which the gneissose granite is overprinted by another pervasive deformation phase, leading to transformation of the gneissose granite rocks into ultramylonites.

The SGC is intruded along its eastern, northern and western margins by minor to large igneous bodies of Hamash granodiorite, and alkali granite dykes, and overlain by the Late Precambrian subaerial Dokhan volcanics (Akaad & Noweir, 1980) and the Mesozoic Natash volcanics. These igneous bodies are occasionally weakly cataclased, but are generally lacking any signs of ductile fabric.

4. Petrography

The SGC is a medium to coarse-grained deformed granite mass composed mainly of variable amount of plagioclase, quartz and

alkali feldspar together with minor amounts of hornblende and biotite. Iron oxides, apatite and zircon are common accessory phases. The tonalite samples usually have more hornblende, but less biotite, compared with trondhjemite, granodiorite and monzogranite samples. The least deformed granites are massive and largely preserve the original hypidiomorphic textures (Fig. 3a), whereas the highly deformed granites contain numerous sub-parallel porphyroclasts of plagioclase, quartz, alkali feldspar and hornblende (Fig. 3b, c), set in a relatively fine-grained groundmass (up to 30%) composed of foliated aggregates of quartz, actinolite, biotite, epidote and chlorite (Fig. 3d). Less deformed monzogranite samples commonly contain quartz and alkali feldspar in characteristic angular intergrowths (i.e. granophyric textures) (Fig. 3e). Plagioclase is partially to entirely altered to aggregates of epidote, zoisite, calcite and quartz.

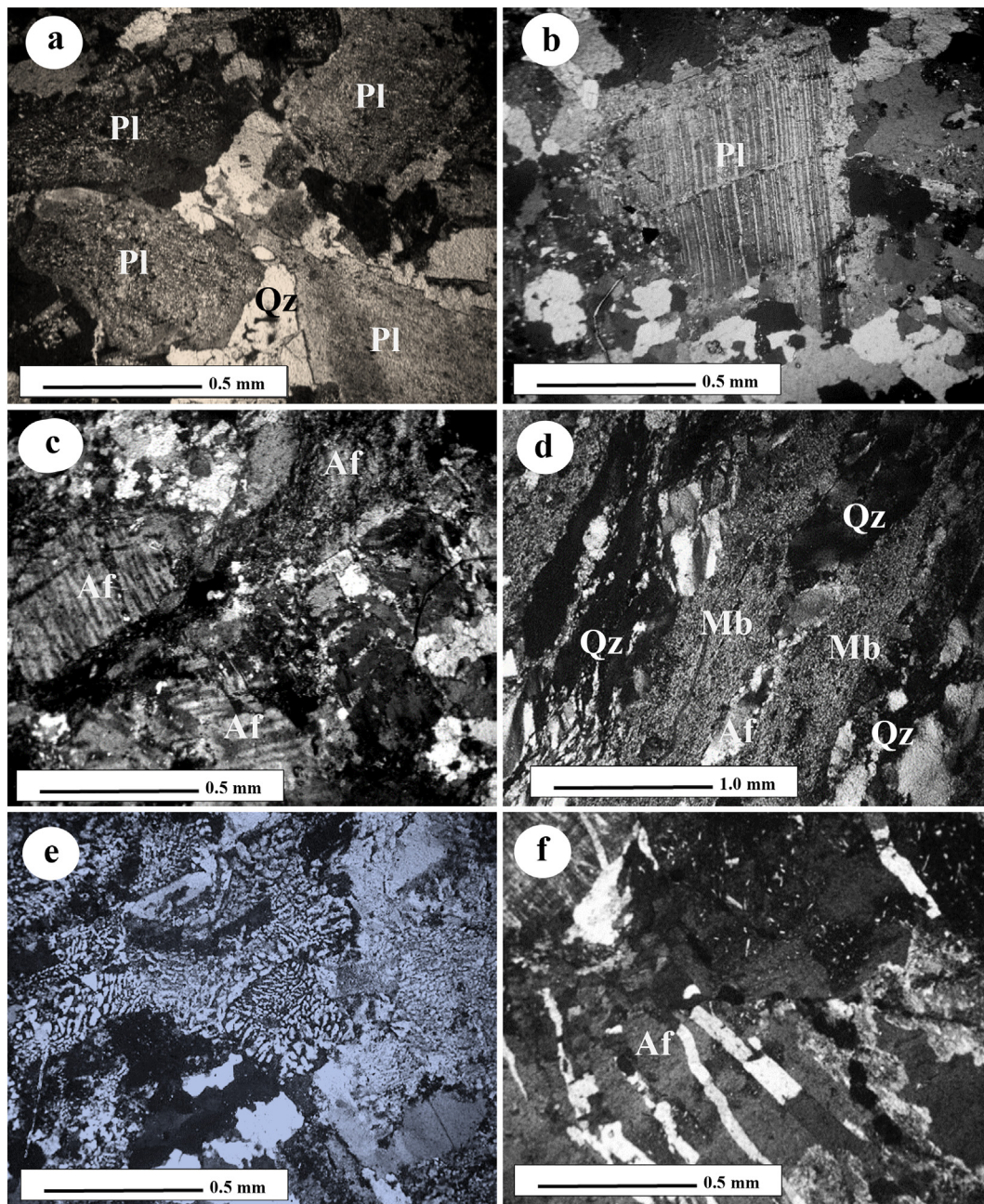


Fig. 3. Main petrographic features of the Shaitian granite complex (SGC): (a) Less deformed trondhjemite sample exhibits hypidiomorphic granular texture. Note the granulation of quartz into fine-grained domains along plagioclase grains. (b) Sample of the cataclased tonalite exhibiting mortar texture formed of strained plagioclase porphyroclast embedded in a groundmass composed of quartz and plagioclase aggregates. Note the marginal granulation of the plagioclase porphyroclast. (c) Cataclased monzogranite with a mortar texture consisting of microcline perthite porphyroclast embedded in a groundmass composed mainly of quartz and plagioclase. (d) A photomicrograph of groundmass in a highly deformed tonalite sample showing banded structures marked by alternating mafic and felsic bands. The mafic bands (Mb) are composed of sericite, epidote and iron oxides, whereas the felsic bands are composed of recrystallized quartz grains. (e) Less deformed monzogranite sample showing granophyric textures. (f) Monzogranite sample with foliation texture resulting from subparallel alignment of the quartz filled fractures that cross-cut alkali feldspar grains. Pl = plagioclase, Af = alkali feldspar; Qz = quartz. All micrographs are between crossed Nicols.

Quartz occurs as water-clear clusters between plagioclase grains and usually has margins recrystallized into fine-grained domains. Alkali feldspar, mostly microcline, is present as sericitized anhedral crystals, usually exhibiting normal and reverse zoning and sometimes has broken margins or crossed by fractures filled with quartz (Fig. 3f). Hornblende is partially replaced, particularly along fractures and boundaries, by uraltite, chlorite, epidote, calcite and iron oxides aggregates. In mesocratic granites within the core of the SGC, hornblende may form large poikilitic grains, sometimes enclosing resorbed clinopyroxene grains. Biotite is found replacing

hornblende in the mesocratic granites, whereas in the more leucocratic granites, it forms fine flakes, frequently gathered in irregular clusters between plagioclase and quartz grains. It is locally replaced by chlorite, sphene and iron oxides.

The mafic enclaves are composed of hornfelsic metabasalt and micro-metagabbro containing blastoporphyratic crystals of hornblende (up to 3×1.8 mm), embedded in a fine-grained granoblastic groundmass composed of altered plagioclase, partly chloritized biotite, actinolite, chlorite, sphene and iron oxides. Occasionally, quartz occurs as subequant grains between the other minerals.

5. Analytical methods

Twenty-nine samples were selected to determine the major and trace element variations within the SGC. Each sample was cut into centimetre-thick slabs to remove weathered surfaces, polished to remove saw marks and ultra-sonically cleaned. The sample slabs were crushed and then powdered in an alumina disc mill. Sample powders were combined with a high purity $\text{Li}_2\text{B}_4\text{O}_7$ flux and fused to form glass disks using procedures described in Rooney et al. (2012). Major element compositions were determined by X-Ray fluorescence (XRF) using a Bruker S4 PIONEER instrument at Michigan State University, USA. Calibration standards included the powder of standards JB-1a and BHVO-1 fused in $\text{Li}_2\text{B}_4\text{O}_7$ (Appendix I, Supplementary Material). The analytical precision for XRF analyses, as calculated from duplicate samples, is better than 1% for most major elements. Trace elements were determined by laser-ablation inductively coupled plasma mass spectrometry (LA-ICP-MS; Photon Machines G2 large-cell excimer laser coupled to a Thermo Scientific iCAP-Q ICP-MS; Appendix II, Supplementary Material) at Michigan State University on the same fused glass following the analytical procedure of Rooney, Morell, Hidalgo, and Franceschi (2015). The precision of the ICP-MS analyses has been calculated from multiple analyses of fused powder of the BHVO-1 and JB-1a standards, and normally stayed within $\pm 5\%$ or better (Appendix I, Supplementary Material). Each sample was run as triplicate analyses, which deviated by less than 5% of each other, with the exception of a few low-concentration Rb and Cs samples which reproduced within 7% and 10% respectively. The major and trace element compositions of the various rock units are shown in Appendix III (Supplementary Material).

Zircon from samples M23A (tonalite), H32A (trondhjemite), S3A (granodiorite) and M40 (monzogranite) (detailed petrographic descriptions are available in Appendix IV, Supplementary Material) were separated using standard techniques of crushing and sieving, followed by Wilfley table, magnetic separation and heavy liquids before handpicking under binocular microscope. They were mounted in epoxy disks (EPO-TEK® 301 from Epoxy Technology Inc.), ground and polished at $0.25\ \mu\text{m}$ to expose crystal interiors. U-Th-Pb isotopic data on zircons from samples H32A, S3A and M40 were obtained by laser ablation inductively coupled plasma spectrometry (LA-ICPMS) at the Laboratoire Magmas et Volcans (LMV Clermont-Ferrand, France, Appendix V, Supplementary Material). The analyses at LMV involved the ablation of minerals with a Resonetics M-50 excimer laser system operating at a wavelength of 193 nm, spot diameters of $27\ \mu\text{m}$, repetition rates of 3 Hz and fluency of $2.5\ \text{J}/\text{cm}^2$. The ablated material was carried into helium and then mixed with nitrogen and argon before injection into the plasma source of a Thermo Element XR sector field high-resolution ICP-MS. Alignment of the instrument and mass calibration were performed before every analytical session using the NIST SRM 612 reference glass, by inspecting the signals of ^{238}U , ^{232}Th and ^{208}Pb by obtaining a Th/U ratio > 0.95 and by minimising the ThO^+/Th^+ ratio to a value lower than 0.4 at the beginning of the analytical session. The analytical method for isotope dating with laser ablation ICPMS is similar to that reported in Hurai, Paquette, Huraiová, and Konečný (2010) and Paquette, Piro, Devidal, Bosse, and Didier (2014). The occurrence of common Pb in the sample can be monitored the $^{204}\text{Pb} + \text{Hg}$ signal intensity, but no common Pb correction was applied owing to the large isobaric interference from Hg. The ^{235}U signal is calculated from ^{238}U on the basis of the ratio $^{238}\text{U}/^{235}\text{U} = 137.818$ (Hiess, Condon, McLean, & Noble, 2012). Single analyses consisted of 30 s of background integration with laser off followed by 1-min integration with the laser firing and a 30 s delay to wash out the previous sample and prepare the next analysis. Data are corrected for U-Pb fractionation occurring during laser ablation of samples and for instrumental mass bias by standard bracketing with repeated measurements of GJ-1 zircon standards (Jackson, Pearson, Griffin, & Belousova, 2004). Repeated analyses of 91500 zircon standard (Wiedenbeck et al., 1995) treated as unknown,

independently control the reproducibility and accuracy of the corrections. 52 analyses of 91,500 zircon standard exclusively yield concordant age at $1065 \pm 3\ \text{Ma}$ ($\text{MSWD}_{(C+E)} = 0.4$) (Paquette, Médard, Francomme, Bachèlery, & Hénot, 2019). Data reduction was carried out with the software package GLITTER® from Macquarie Research Ltd. (Jackson et al., 2004; van Achterbergh, Ryan, Jackson, & Griffin, 2001). Calculated ratios were exported and Concordia ages and diagrams were generated using Isoplot/Ex v. 2.49 software package by Ludwig (2001). The concentrations of U-Th-Pb were calibrated relative to the certified contents of GJ-1 zircon (Jackson et al., 2004).

In-situ U-Th-Pb isotope analyses on zircon from tonalite sample M23A were obtained using an ESI NWR 193 nm laser ablation (LA) system coupled to a Nu Plasma II multiple collector – ICPMS (LA-MC-ICPMS) located within the MITERAC facility at Notre Dame University, USA (Appendix VI, Supplementary Material). Typical data acquisition consisted of 45 s of background followed by 60 s of ablation with a fluence of $10\text{--}12\ \text{J}/\text{cm}^2$, repetition rate of 5 Hz on a spot size of 40 to $55\ \mu\text{m}$. Simultaneous measurements of ^{202}Hg , $^{204}\text{Pb} + \text{Hg}$, ^{206}Pb , ^{207}Pb , ^{208}Pb , ^{232}Th , and ^{238}U were obtained using a combination of ion counters (discrete dynode secondary electron multipliers) and Faraday cups (Simonetti & Neal, 2010). ^{202}Hg was measured to monitor the ^{204}Hg interference on ^{204}Pb using a $^{204}\text{Hg}/^{202}\text{Hg}$ value of 0.229883 (Simonetti & Neal, 2010). A sample-standard bracketing technique using two well established zircon standards, Plešovice (Sláma et al., 2008) and GJ-1 (Jackson et al., 2004), were used to correct for instrumental drift and laser induced elemental fractionation by minimising the oxide production to a value lower than 3% at the beginning of the analytical session. Repeated analyses of Plešovice zircon standard treated as unknown, independently control the reproducibility and accuracy of the corrections. 16 analyses of Plešovice zircon standard exclusively yield concordant age at 336.5 ± 1.5 (2SD, $\text{MSWD} = 0.34$). Lolite (v3.1; Paton et al., 2010) data reduction software was used to correct for down-hole fractionation, instrumental drift, instrumental mass bias, etc. prior to generation of concordia diagrams in Isoplot v3.0 (Ludwig, 2003). The complete data set and calculated apparent ages are listed in Appendix VII (Supplementary Material).

The Sr-Nd isotope analytical work was carried out at the Swedish Museum of Natural History in Stockholm. Between 100 and 200 mg of rock powder from each sample were dissolved in a 10:1 mixture of concentrated HF and HNO_3 , together with a mixed $^{147}\text{Sm}\text{--}^{150}\text{Nd}$ spike, in teflon capsules at $205\ ^\circ\text{C}$ for a few days. After evaporation and redissolution in 6 M HCl, the solutions were passed through Biospin columns filled with 0.5 ml TRU-spec ion exchange resin for separation of Sr and REE as a group using HCl and HNO_3 as solutes (with iron first collected in pre-columns filled with 0.75 ml AG1-X8 cation exchange resin). Strontium was further purified in columns with 0.5 ml Sr-spec resin, using 2 M and 8 M HNO_3 for purification, and warm 0.05 M HNO_3 to elute the Sr. From the REE solutions, Sm and Nd were separated in Eichrom columns with 2 ml Ln-spec resin, using HCl of different concentrations as elution media. Prior to mass spectrometer analysis, the samples were treated with concentrated HNO_3 and 30% H_2O_2 in order to remove any organic residues, and Sm and Nd were dissolved in 1 ml 6 M HCl which was evaporated. Spiked Sm and Nd and unspiked Sr were loaded on double Re filaments and analyzed with a Thermo Triton thermal ionization mass spectrometer in static mode (Appendix VIII, Supplementary Material). Corrections for background, spike addition (Sm and Nd), interference and fractionation were carried out as reported in the footnotes to the data tables. The Sm and Nd concentrations, as well as the Nd isotope compositions, were calculated from the spiked analyses, using the combined $^{147}\text{Sm}\text{--}^{150}\text{Nd}$ spike. For Rb-Sr, the Rb and Sr contents reported in Appendix III (Supplementary Material) were instead used for calculation of initial Sr isotope compositions. The results are reported in Table 1, together with results on the NBS SRM987 Sr standard, the La Jolla Nd standard, and the BCR-2 rock standard.

Table 1
Sr-Nd isotope data for various rock units within the SGC.

| No. | Sample | Rock type | $^{87}\text{Rb}/^{86}\text{Sr}^a$ | $^{87}\text{Sr}/^{86}\text{Sr} (2\sigma)^b$ | Sr_i | ϵ_{Sr}^c | $^{147}\text{Sm}/^{144}\text{Nd}^d$ | $^{143}\text{Nd}/^{144}\text{Nd} (2\sigma)^d$ | ϵ_{Nd}^e | $\epsilon_{\text{Nd}_i}^e$ | $T_{\text{DM-1}}^f$ | $T_{\text{DM-2}}^g$ |
|-----|---------|----------------|-----------------------------------|---|---------------|--------------------------|-------------------------------------|---|--------------------------|----------------------------|---------------------|---------------------|
| 1 | S- 24B | Mafic xenolith | 0.1510 | 0.703467 (5) | 0.70177 | -26 | 0.2187 | 0.513065 (3) | 8.3 | 6.1 | 2.60 | |
| 2 | S- 122A | Mafic xenolith | 0.0192 | 0.702661 (5) | 0.70245 | -16 | 0.2195 | 0.513146 (3) | 9.9 | 7.6 | -0.13 | |
| 3 | S-23 | Host tonalite | 0.5913 | 0.709235 (4) | 0.70259 | -14 | 0.1707 | 0.512837 (3) | 3.9 | 6.5 | 1.11 | 1.00 |
| 4 | S-21 | Host tonalite | 0.5105 | 0.708687 (6) | 0.70295 | -9 | 0.1984 | 0.512981 (3) | 6.7 | 6.5 | 1.70 | 1.00 |
| 5 | S-5 | Host tonalite | 0.4462 | 0.704456 (4) | 0.69944 | -59 | 0.1861 | 0.512926 (2) | 5.6 | 6.7 | 1.25 | 0.98 |
| 6 | S-13 | Host tonalite | 0.1646 | 0.704070 (4) | 0.70222 | -19 | 0.1834 | 0.512911 (5) | 5.3 | 6.7 | 1.21 | 0.98 |
| 7 | S- 24A | Host tonalite | 0.2049 | 0.722008 (5) | 0.71971 | +229 | 0.1489 | 0.512786 (2) | 2.9 | 7.8 | 0.86 | 0.89 |
| 8 | S-30 | Host tonalite | 0.2449 | 0.705493 (4) | 0.70274 | -12 | 0.1915 | 0.512940 (3) | 5.9 | 6.4 | 1.45 | 1.01 |
| 9 | M.51 | Host tonalite | 0.3684 | 0.702729 (6) | 0.69859 | -71 | 0.1524 | 0.512810 (2) | 3.4 | 7.9 | 0.85 | 0.88 |
| 10 | M.58 | Host tonalite | 0.3325 | 0.703541 (5) | 0.69980 | -54 | 0.1911 | 0.512963 (2) | 6.3 | 6.9 | 1.27 | 0.96 |
| 11 | M97 | Host tonalite | 0.2790 | 0.706125 (6) | 0.70299 | -8 | 0.1760 | 0.512887 (2) | 4.9 | 7.0 | 1.07 | 0.96 |
| 12 | S- 3B | Trondhjemite | 1.5096 | 0.718363 (5) | 0.70238 | -18 | 0.1842 | 0.512935 (2) | 5.8 | 7.0 | 1.12 | 0.92 |
| 13 | S- 3A | Granodiorite | 1.2050 | 0.714967 (5) | 0.70249 | -16 | 0.2116 | 0.513072 (2) | 8.5 | 7.1 | 5.82 | 0.90 |
| 14 | S- 8A | Monzogranite | 1.5370 | 0.719295 (5) | 0.70382 | +2 | 0.1492 | 0.512788 (2) | 2.9 | 7.3 | 0.86 | 0.86 |
| 15 | S8-R2 | Monzogranite | 2.2731 | 0.707366 (4) | 0.68448 | -273 | 0.1802 | 0.512882 (2) | 4.8 | 6.3 | 1.23 | 0.95 |
| 16 | BCR-2* | Standard | | 0.705004 (4) | | | 0.1387 | 0.512639 (2) | +0.1 | | | |

^a $^{87}\text{Rb}/^{86}\text{Sr}$ ratios calculated from Rb and Sr concentrations by chemical analyses reported in Appendix III, and measured $^{87}\text{Sr}/^{86}\text{Sr}$ ratios.

^b $^{87}\text{Sr}/^{86}\text{Sr}$ ratios measured on a Thermo Triton thermal ionization mass spectrometer in static mode, corrected for Rb interference and normalized to $^{86}\text{Sr}/^{88}\text{Sr} = 0.1194$. Four runs of the NBS SRM 987 Sr-standard during the measurement periods gave $^{87}\text{Sr}/^{86}\text{Sr}$ ratios of 0.710210 ± 6 , 0.710204 ± 4 , 0.710206 ± 5 and 0.710212 ± 6 ($2\sigma_m$), respectively. Because of the systematically low NBS 987 standard values (not only during these analyses), an additional correction of $+0.000035$ was applied to all measured $^{87}\text{Sr}/^{86}\text{Sr}$ ratios, in order to bring them close to the accepted NBS 987 value of 0.710245. Errors given as 2 standard deviations of the mean from the mass spectrometer run in the last digits.

^c ϵ_{Sr} -values according to McCulloch and Chappell (1982); present-day $^{87}\text{Rb}/^{86}\text{Sr}$ mantle ratio = 0.0827, present-day $^{87}\text{Sr}/^{86}\text{Sr}$ mantle ratio = 0.7045. Initial Sr ratios and ϵ_{Sr} -values calculated using newly revised decay constant for ^{87}Rb of 1.3972×10^{-11} (Villa, De Bièvre, Holden, & Renne, 2015).

^d All Sm and Nd samples measured with a Thermo-Triton thermal ionization mass spectrometer in static mode. $^{147}\text{Sm}/^{144}\text{Nd}$ ratio calculated from isotope dilution (ID) analysis with combined ^{147}Sm - ^{150}Nd tracer. Estimated analytical uncertainty of $^{147}\text{Sm}/^{144}\text{Nd}$ ratio is $\pm 0.5\%$. $^{143}\text{Nd}/^{144}\text{Nd}$ ratios calculated from ID run, corrected for Sm interference and normalized to $^{146}\text{Nd}/^{144}\text{Nd} = 0.7219$. Four runs of the La Jolla Nd-standard during the measurement periods both gave $^{143}\text{Nd}/^{144}\text{Nd}$ ratios of 0.511868 ± 3 , 0.511868 ± 3 , 0.511872 ± 3 and 0.511871 ± 3 ($2\sigma_m$), respectively. Because of the systematically high La Jolla standard values (not only during these analyses), an additional correction of -0.000018 was applied to all measured $^{143}\text{Nd}/^{144}\text{Nd}$ ratios, in order to bring them close to the accepted La Jolla value of 0.511852. Errors given as 2 standard deviations of the mean from the mass spectrometer run in the last digits.

^e Present-day and initial ϵ_{Nd} values calculated using a present-day chondritic $^{147}\text{Sm}/^{144}\text{Nd}$ ratio of 0.1966, and a present-day chondritic $^{143}\text{Nd}/^{144}\text{Nd}$ ratio of 0.512638 (Jacobsen & Wasserburg, 1984; recalculated in Dickin, 1995). Initial ratios and epsilon notations are calculated using 800 Ma, 754 Ma, 737 Ma and 717 Ma for tonalite, trondhjemite, granodiorite and monzogranite, respectively. Initial ratios and epsilon notations for mafic enclaves are calculated at 800 Ma as minimum age that resembles that of the host tonalite. The decay constant used is 6.54×10^{-12} (yr^{-1}) for the decay of ^{147}Sm to ^{143}Nd (Lugmair & Marti, 1978).

^f Single-stage Nd model age (Ga) calculated following the linear depleted mantle model of Goldstein et al. (1984) with present-day $^{147}\text{Sm}/^{144}\text{Nd}$ mantle ratio = 0.2136 and present-day $^{143}\text{Nd}/^{144}\text{Nd}$ mantle ratio = 0.513151 ($\epsilon_{\text{Nd}} = +10$; cf. Milisenda et al., 1994).

^g Two-stage depleted mantle model age (Ga) following Milisenda et al. (1994). The calculations were run in two-steps: (1) calculating the Nd evolution line back to the magmatic age of the rock using the measured $^{147}\text{Sm}/^{144}\text{Nd}$ ratio, (2) calculating the Nd evolution line of the sample prior to the crystallization age using an assumed (not the measured) $^{147}\text{Sm}/^{144}\text{Nd}$ ratio of 0.134, equivalent to the lower crustal of the Arabian-Nubian Shield. $T_{\text{DM-2}}$ are not calculated for mafic enclaves because they resulted directly from melting of mantle wedge.

* BCR-2 is the Columbia River Basalt standard.

6. Geochemistry

6.1. Whole-rock chemistry

Despite the variably altered nature of the samples, the loss on ignition (LOI) values of the analyzed samples (with the exception of mafic enclaves) are less than 2 wt% (Appendix III, Supplementary Material) and do not show any correlation with mobile elements (e.g. K, Na, Rb and U). These features, together with the uniform ratios of highly mobile element ratios (e.g. U/Th, Cs/Rb, and Rb/Ba, Appendix III, Supplementary Material) as well as the systematic variation between SiO_2 and most major and trace elements as shown in Figs. 4 and 5 indicate that the bulk composition of the analyzed samples have not been subjected to significant modifications during low-temperature alteration and deformation. The mafic enclave samples, on the other hand, are profoundly altered and the mafic minerals are largely converted into chlorite and actinolite. Therefore, only immobile elements such as high field strength elements (e.g. HFSE: Zr, Hf, Nb, Ta) and transitional elements (e.g. Ni, Cr, Sc, Ti), which are conservative over a wide range of conditions of hydrothermal alteration (e.g. Abu El-Rus, Mohamed, & Lindh, 2017; Middleburg, Van der Weijden, & Woittiez, 1988), are used to unravel the petrogenesis of these enclaves.

On the normative An-Ab-Or diagram, most granitoid rocks straddle the field boundaries of natural TTG gneisses and experimental melts from basaltic precursors (Fig. 6). However, some samples plot in the monzogranite field close to the two-feldspars cotectic at low water-vapour pressures (James & Hamilton, 1969; Fig. 6). This chemical

discrimination largely agrees with microscopic observations that the tonalite and granodiorite samples are distinctly lower in alkali feldspar contents compared to the monzogranite samples, and the trondhjemite samples exhibit the lowest mafic content within the SGC. However, all granitoid samples are sub-alkaline (Fig. 7a), with contents of SiO_2 and total alkalis (Na_2O wt% + K_2O wt%) ranging from 63 to 76 wt% and 3.7 to 7.7 wt% respectively (Appendix III, Supplementary Material). The Al_2O_3 content ranges from 11.2 to 16.5 wt%, resulting in alumina saturation indexes placing the granitoids within the metaluminous field or along the boundary between the metaluminous and peraluminous fields (Fig. 7b). All metaluminous samples usually exhibit normative diopside (Appendix III, Supplementary Material). On the variation diagrams, samples of tonalite, granodiorite and trondhjemite display quasi-linear trends, whereas the monzogranite samples show more scattered trends (Figs. 4, 5).

While the tonalite, trondhjemite and granodiorite samples display nearly flat chondrite normalized - REE patterns ($(\text{La}/\text{Yb})_N = 0.9-1.3$), the monzogranite samples exhibit higher LREE abundances with fractionated patterns from La to Sm ($(\text{La}/\text{Sm})_N = 1.9-2.7$) and rather flat patterns from Dy to Lu ($(\text{Dy}/\text{Yb})_N = \sim 1$). All samples display moderate negative Eu anomalies ($\text{Eu}/\text{Eu}^* = 0.3-0.9$) as well as irregular patterns on primitive mantle-normalized multi-element diagrams, commonly with large negative anomalies in Nb-Ta, La-Ce, P and Ti (Fig. 8a). Compared with worldwide Archean TTG and their modern equivalent adakites, the SGC rocks show less fractionated REE patterns, and generally have multi-element patterns with that lack a positive anomaly in Ba and exhibit sharper negative anomalies in Ti and P (Fig. 8b).

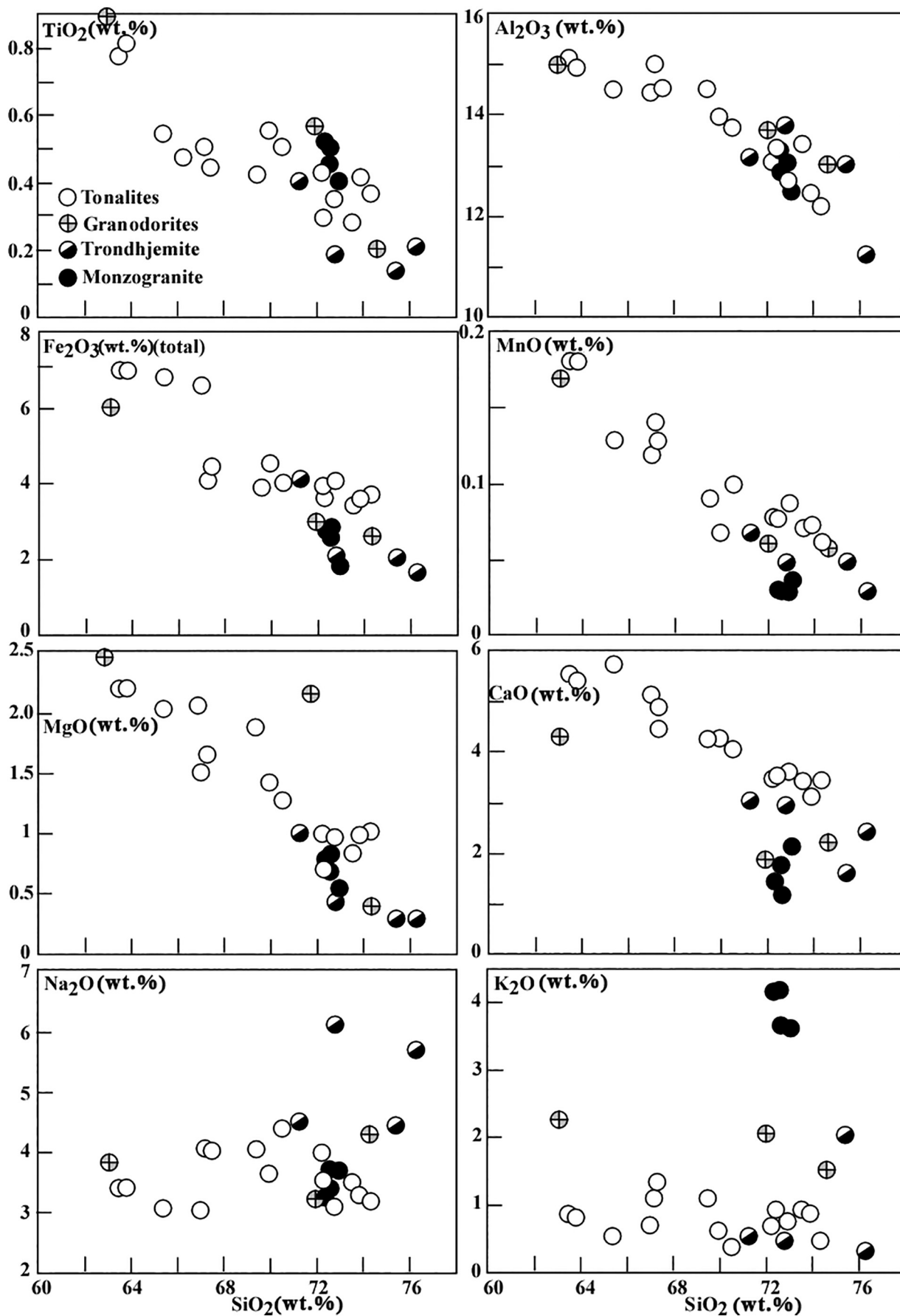


Fig. 4. Bivariate diagrams showing the variation of the measured major elements versus SiO₂ within the SGC. Mafic xenolith samples exhibit low silica content (<44 wt%) and are omitted from plots for simplicity.

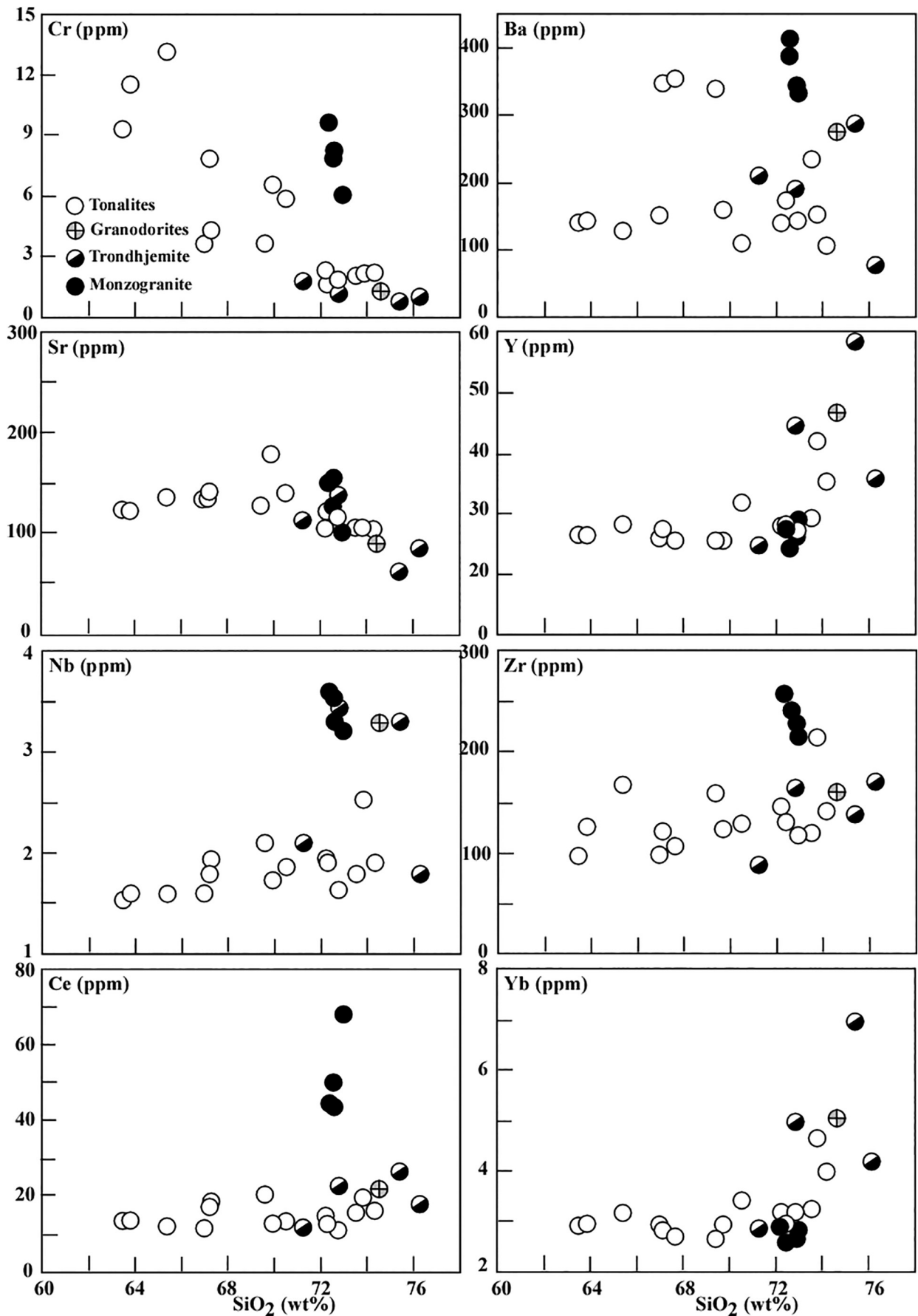


Fig. 5. Bivariate diagrams showing the variation of selected trace elements (ppm) versus SiO₂ (wt%) within the SGC. Mafic xenolith samples are omitted from plots for simplicity.

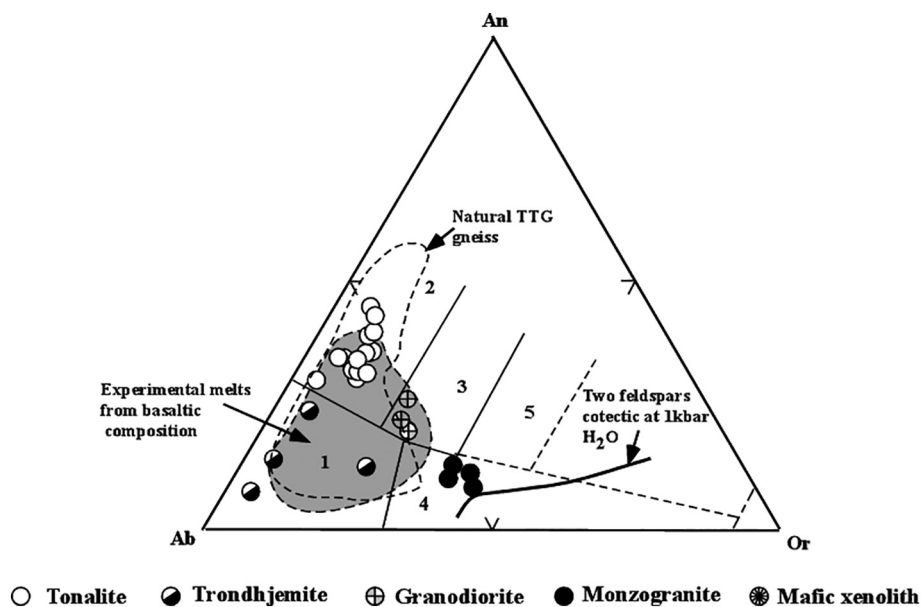


Fig. 6. The SGC samples plotted on the normative An-Ab-Or diagram (Barker, 1979; O'Conner, 1965). Fields: 1 to 5 are trondhjemite, tonalite, granodiorite, granite, Qz-monzonite, respectively. The solid line is the two feldspars boundary cotectic in the quartz-saturated feldspar system at 1 kb water vapour after James and Hamilton (1969). Fields of natural TTG and experimental melts are from basaltic precursors are from Wyman, Hollings, and Biczok (2011).

The meta-basalt enclaves exhibit low contents of silica (c. 44 wt%) and alkalis ($\text{Na}_2\text{O} + \text{K}_2\text{O} < 3.7$ wt%) placing them in the basalt field on total alkalis versus silica (TAS) diagram (Fig. 7a). Compared to the host tonalite, the mafic enclave samples exhibit considerably higher MgO, Ni, Co, V, Cr and Sc and lower abundances in some incompatible elements such as Rb, Ba, Y, Zr and REE (Appendix III, Supplementary Material). On the chondrite-normalized REE plot, the mafic enclaves exhibit REE patterns similar to MORB with flat MREE-HREE ($(\text{Sm}/\text{Lu})_N = 1.1$) and no Eu anomaly. While mafic enclave S-24B exhibits depletion in LREE ($(\text{La}/\text{Sm})_N = 0.6$) similar to N-MORB, mafic enclave S-122A shows enrichment in LREE ($(\text{La}/\text{Sm})_N = 4.5$). On normalized multi-element plots, the mafic enclaves exhibit lower concentrations of most elements compared to the host tonalite, except for Cs, P and Ti, and in the case of sample S-122A also La and Ce (Fig. 8a).

6.2. Multi-crystallization ages

Zircon from tonalite sample M23A ($24^\circ 40' 32.5''\text{N}$, $34^\circ 9' 39.8''\text{E}$) mostly occur as relatively short prismatic and clear crystals, dominated by pyramidal terminations, with a length/width (l/w) ratio less than 2.5. 19 zircon grains and parts of broken grains were analyzed for their U–Pb isotope composition (Appendix VII, Supplementary Material). Zircon grain no. 8 plots considerably below the concordia line with a discordancy of about 11% and thus it is discarded from the age estimation of sample M23A (Fig. 9a). In contrast, zircon grain no. 19 gave a concordia age of 796 ± 10 Ma with MSWD (mean square weighted deviation) of 1.05 and a concordance value of 0.31. The remaining 17 zircon grains are 1%–4% discordant (Fig. 9a), and define a discordia-line with an upper intercept at 800 ± 18 Ma (MSWD = 1.9), which is consistent with the concordant zircon grain no 19.

Zircon from trondhjemite sample H32A ($24^\circ 40' 6.5''\text{N}$, $34^\circ 10' 23.8''\text{E}$) are transparent and display euhedral to subhedral prisms (length/width ratio of about 3), occasionally with multiple zoning and pyramidal terminations. Thirty-four zircon grains were analyzed for their U–Pb isotopes (Appendix VII, Supplementary Material). The zircon grains combine to a concordia age of 754.4 ± 3.9 Ma (MSWD = 1.2; Fig. 9b).

Zircon from granodiorite sample S3A ($24^\circ 40' 36.7''\text{N}$, $34^\circ 10' 36.7''\text{E}$) occur as transparent, euhedral to subhedral prisms (length/width ratio of about 3–4), occasionally with pyramidal terminations. Thirty-

five zircon grains were analyzed for their U–Pb isotopes (Appendix VII, Supplementary Material). Uranium contents are rather low for zircon hosted in granites, mostly ranging between 50 and 100 ppm, and Th/U ratios of 0.2–0.4. Three grains (Zr 12, Zr 19 and Zr 58) are discordant due to Pb-loss (Fig. 9c). The remaining zircon grains are concordant and define a concordia age of 738 ± 3.8 Ma (MSWD = 0.51; Fig. 9c).

Thirty-five zircon grains from the monzogranite sample M40 ($24^\circ 39' 12.8''\text{N}$, $34^\circ 9' 18.3''\text{E}$) were analyzed Appendix VII, Supplementary Material). The zircon grains are clear, transparent, and commonly with wide cores surrounded by multiple zonation at margins. Twenty-six zircon grains produce a concordia age of 717.3 ± 3.2 Ma with MSWD = 0.58 (Fig. 9d). The other zircon grains plot below the concordia line with discordance up to 14%. These zircon grains are generally cracked and less transparent compared to the concordant zircon grains and their discordance most probably reflects Pb-loss.

6.3. Radiogenic isotope ratios

When considering the initial Sr and Nd isotope ratios calculated for the zircon U–Pb age (Table 1), the SGC display a wide range of Sr_i from 0.6845 to 0.7197 (Table 1). This wide range in Sr_i cannot be attributed to the contribution from crust due to the weak correlations between Sr_i and incompatible elements ratios that are sensitive to crustal contamination/mingling (e.g. Ce/Pb, U/Nb, Nb/Th, and K/P; Leeman & Hawkesworth, 1986; Hofmann & Jochum, 1996; Abu El-Rus, Chazot, Vannucci, & Paquette, 2018) (Appendix IX, Supplementary Material). Since Rb and Sr are relatively mobile elements and might readily be disturbed either by the influx of fluids or by later thermal events (even modest) (e.g. Barovich & Patchett, 1992; Paoli, Dini, Petrelli, & Rocchi, 2019), the large scatter of Sr_i isotope ratios within SGC might be attributed to later tectonic event(s) that led to the deformation of the SGC. The Sr isotope ratios are therefore not used in probing the genesis of SGC. Similar conclusions have been made regarding the wide range of Sr_i values observed in the corresponding gneissose granites of the other parts of Nubian shield in Egypt (Khudeir, Abu El-Rus, et al., 2006; Khudeir, Bishara, et al., 2006; Khudeir et al., 2008).

In contrast, since Sm and Nd undergo only slight fractionation during the post-crystallization metamorphic processes (e.g. Champion, 2013; Dickin, 1995), their isotopic ratios can be used to make inferences to

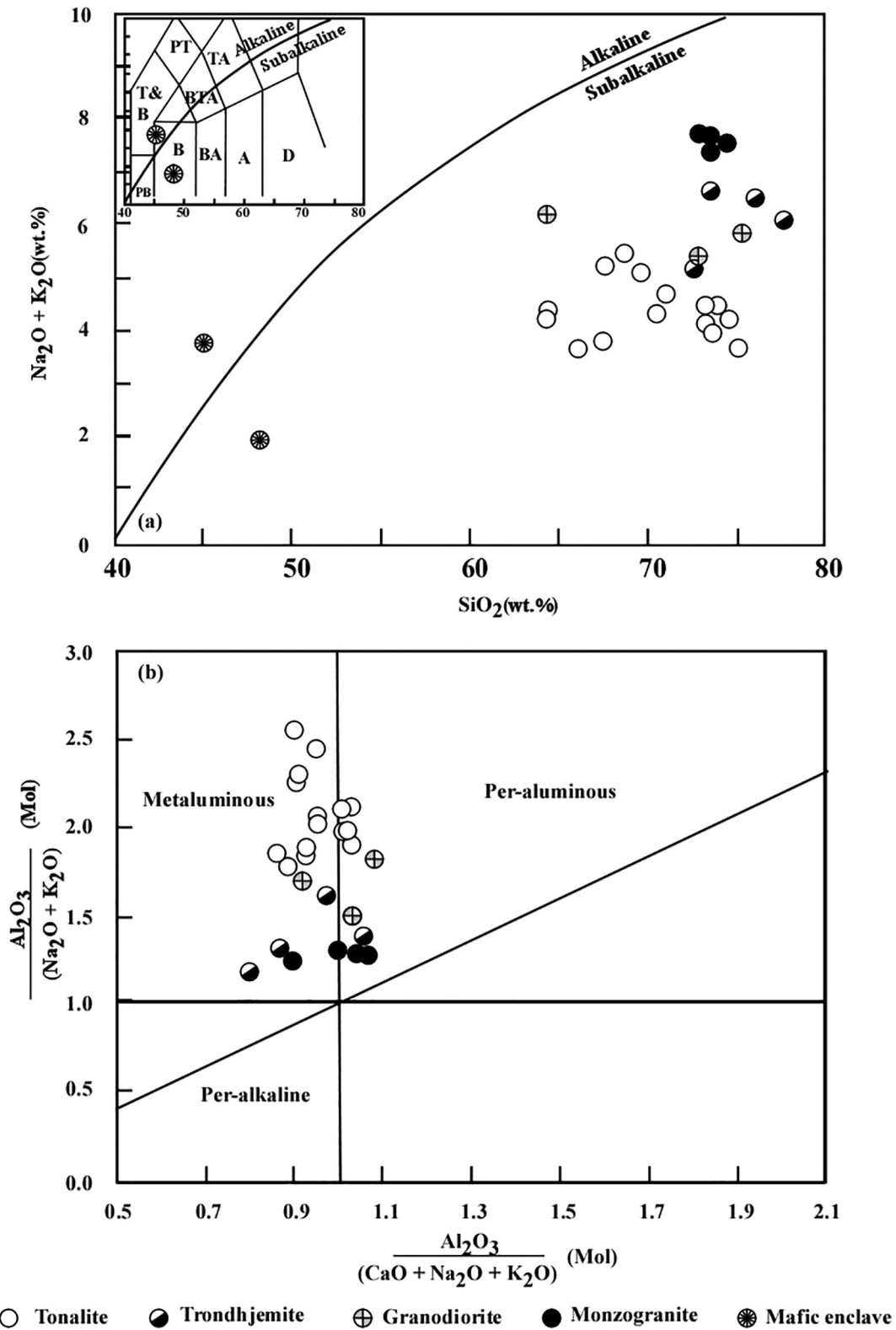
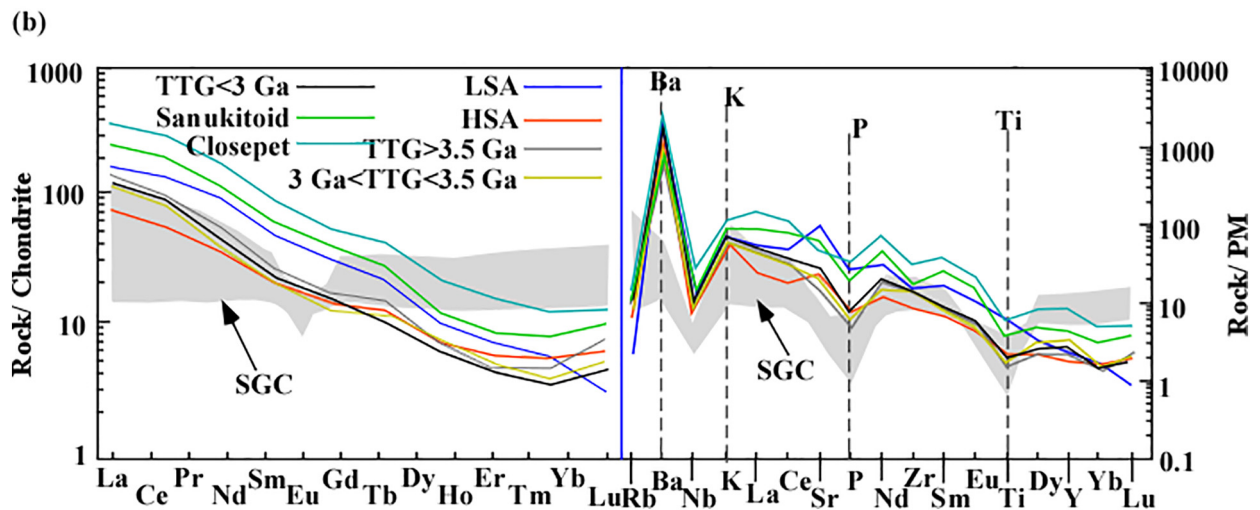
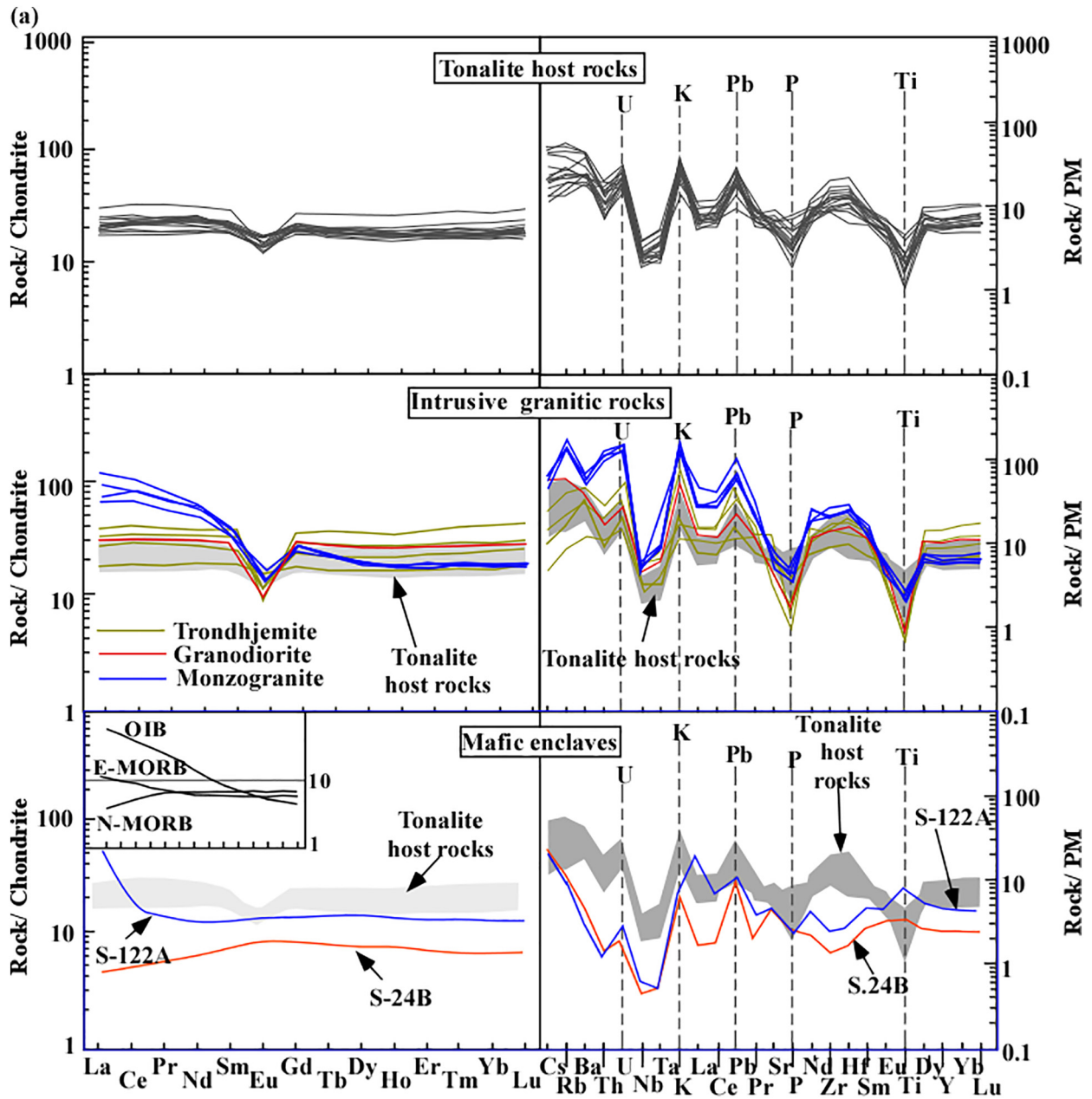


Fig. 7. Composition of the SGC plotted on: (a) the $(\text{Na}_2\text{O} + \text{K}_2\text{O})$ versus SiO_2 (TAS) diagram after *Le Bas, Le Maitre, Streckeisen, and Zanettin (1986)*. The boundary line between the alkaline and subalkaline fields is after *Irvine and Barager (1971)*. Inset shows the field boundaries for nomenclature of the fine grained mafic enclaves (B = basalt, BA = basaltic andesite, A = andesite, D = Dacite, TA = trachy-andesite, BTA = basaltic trachy-andesite, TB = trachy-basalt, PB = picro-basalt, T&B = tephrite and basanite, PT = phono-teprite). (b) Shand's index diagram (the alumina saturation indexes) after *Maniar and Piccoli (1989)*. Mafic enclaves have Al/NK index ~5.1 and are not shown. All samples are plotted on a volatile-free basis.

the melting source. The SGC shows limited variation of initial $^{143}\text{Nd}/^{144}\text{Nd}$ ratios corresponding to positive $\epsilon_{\text{Nd}i}$ values with a range of +6 and +8 (Table 1).

The calculated single-stage $T_{\text{DM-1}}$ model ages for most granitoid samples relative to the depleted-mantle evolution curve are widely scattered (Table 1) and is thus inconsistent with the juvenility of the



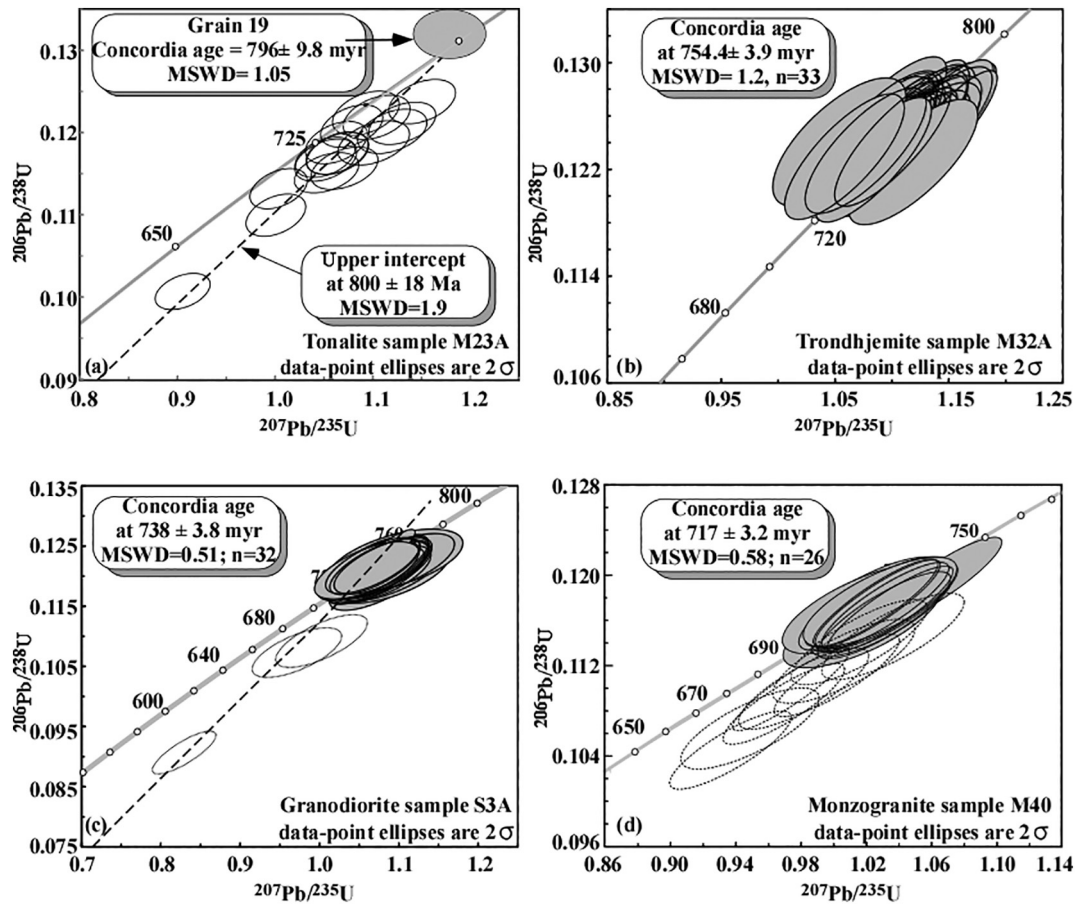


Fig. 9. Concordia plots of U-Pb zircon results for (a) tonalite samples M23A, (b) trondhjemite sample H32A, (c) granodiorite sample S3A, and (d) monzogranite sample M40. Open and closed ellipses represent the points exhibiting discordant and concordant (or near-concordant) ages, respectively.

ANS (e.g. Hargrove, Stern, Kimura, Manton, & Johnson, 2006; Johnson et al., 2011). Furthermore, the two mafic enclave samples have Nd evolution lines sub-parallel to the mantle Nd-evolution curves of Goldstein, O’Nions, and Hamilton (1984) (Fig. 10a), since they have $^{147}\text{Sm}/^{144}\text{Nd}$ ratios similar to the depleted mantle (0.2187 and 0.2195, respectively). Because of that, their $T_{\text{DM-1}}$ model ages, determined by the intersection of these lines with the respective mantle curve, become unreasonably high or low (negative, i.e. future ages). Such uncertainty is widely reported for rock samples that exhibit $^{147}\text{Sm}/^{144}\text{Nd}$ ratios >0.14 (e.g. Champion, 2013; Jahn et al., 2001; Milisenda, Liew, Hofmann, & Köhler, 1994). Because of this, a two-stage model age ($T_{\text{DM-2}}$) is adopted (e.g., Liew & McCulloch, 1985; Milisenda et al., 1994), in which the Nd evolution lines are calculated in two stages: (a) in the interval from the present time to the crystallization age, using the measured $^{147}\text{Sm}/^{144}\text{Nd}$ ratios of the samples and (b) in the interval from the crystallization age back to the Depleted mantle curve, using the average $^{147}\text{Sm}/^{144}\text{Nd}$ ratio (i.e. 0.134) of the amphibolites within the Meatiq core complex that represent the lower crust of the Arabian-Nubian Shield in the Eastern Desert (Khudeir, Abu El-Rus, et al., 2006; Khudeir, Bishara, et al., 2006; Khudeir et al., 2008). The two-stage model yields model ages for granitoid rocks ranging from 0.86 to 1.0 Ga, based on the depleted mantle model of Goldstein et al. (1984)

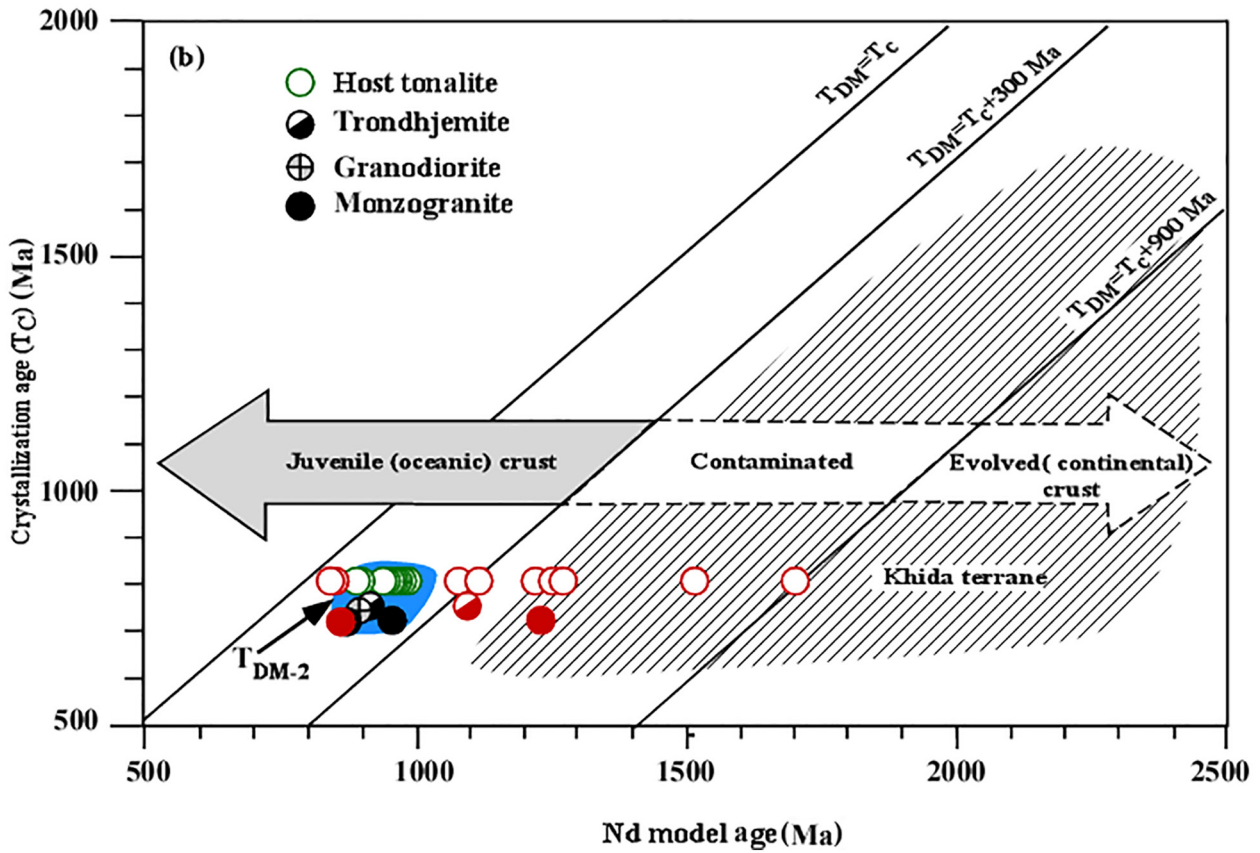
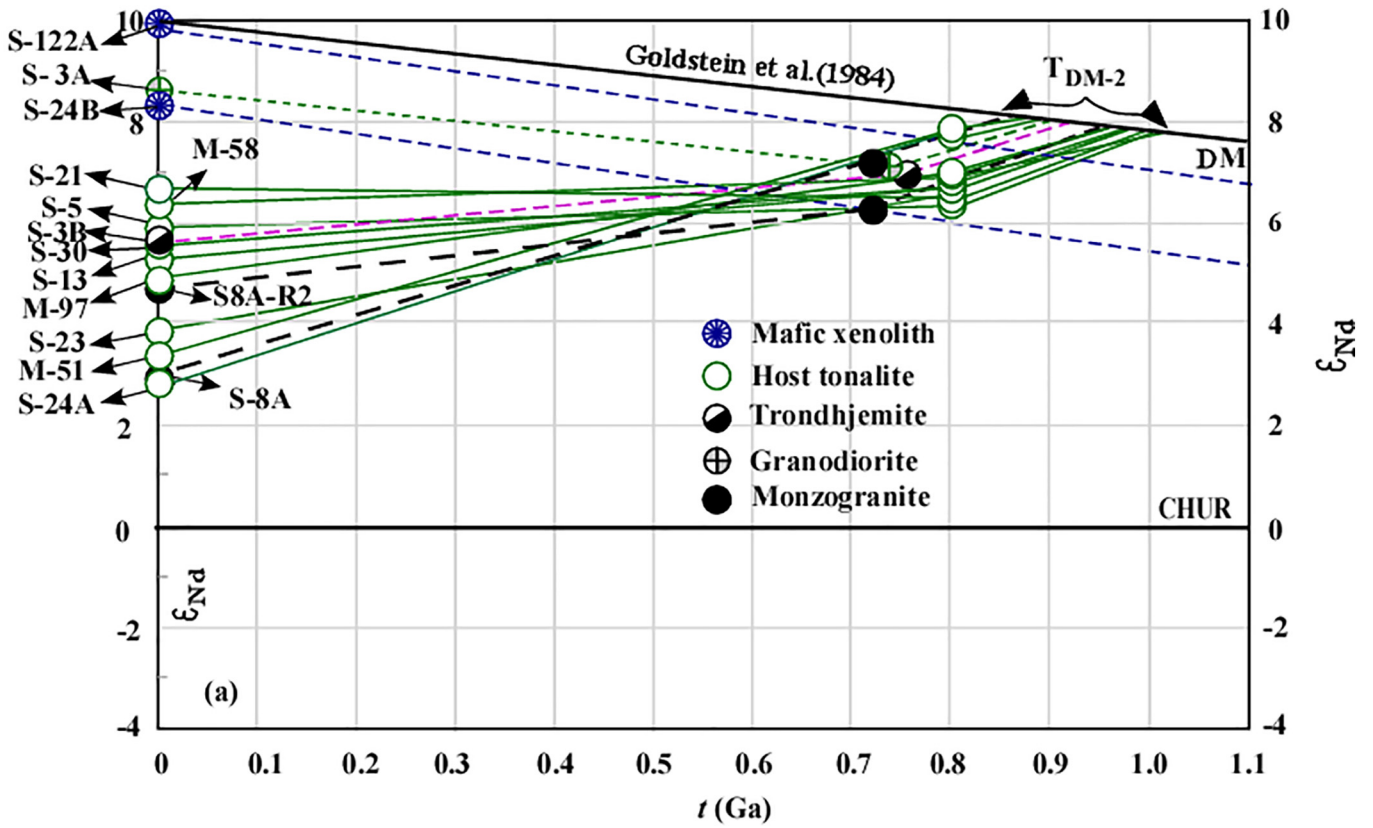
(Table 1). This is between 77 and 230 million years older than their crystallization ages (Fig. 10b). This finding confirms that the Neoproterozoic crust in the Wadi Shait area is a juvenile addition, having formed either from fractional crystallization of the mantle-generated magmas or from re-melting of juvenile crust, consistent with the hypothesis that the ANS dominantly consists of juvenile Pan-African crust (900–550 Ma) (e.g. Andresen et al., 2009, 2010; Béeri-Shlevin, Katzir, Blichert-Toft, Kleinhanns, & Whitehouse, 2010; Hargrove et al., 2006; Johnson et al., 2011).

7. Discussion

7.1. Assessment of volatiles in the evolution of SGC

Crystallization of significant amounts of amphibole and biotite in most granitic samples is robust evidence that the melt achieved water-saturation during some stages of crystallization (Maaløe & Wyllie, 1975; Müller, Thomas, Wiedenbeck, Seltmann, & Breiter, 2006). High normative albite characterizes all granitic samples in the SGC is also consistent with the hydrous nature of the melt (e.g. Holtz, Behrens, Dingwell, & Johannes, 1995; McMillan & Holloway, 1987). The presence of aqueous fluids within the granitic magmas may play

Fig. 8. (a) Chondrite - normalized rare earth element and primitive mantle - normalized multi-element patterns of the various rock units and mafic enclaves within the SGC. For comparison, the averages of N- and E-type MORB and oceanic alkali basalts (OIB) are also shown (data from Sun & McDonough, 1989). Normalization values are those of McDonough and Sun (1995). (b) Comparison between the tonalite-trondhjemite-granodiorite association within the SGC and average compositions of subducted slab-derived melts such as high-silica adakites (HSA) and Archaean TTG suites, or melts derived from metasomatized peridotite mantle wedge such as low-silica adakites (LSA) and Late Archaean sanukitoids and Closepet-type granites (data from Martin et al., 2005).



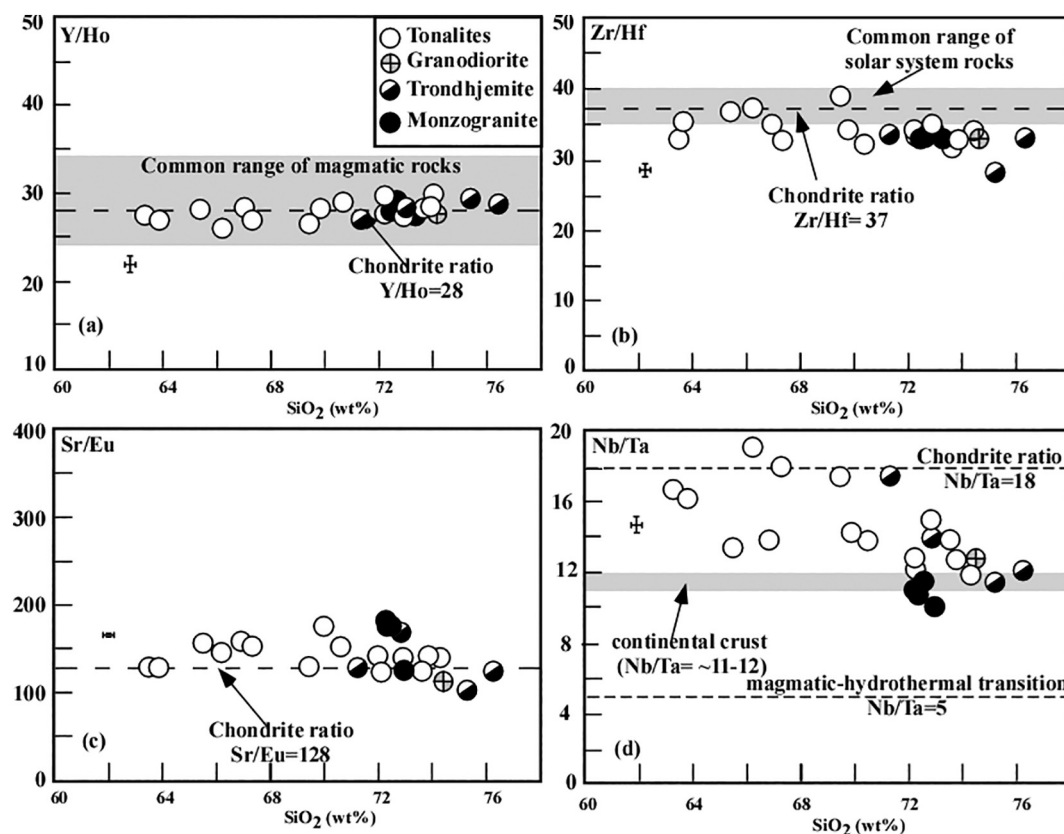


Fig. 11. Bivariate diagrams showing the relations between ratios of some elements that exhibit Charge-And-Radius-Controlled behaviour (CHARAC, Bau, 1996) and SiO_2 . Grey bands in a and b represent Y/Ho ratio in common magmatic rocks and the common Zr/Hf ratios of the solar system rocks, respectively (data after Jahn et al., 2001), whereas the grey band in (d) represents the Nb/Ta ratio in continental crust (Rudnick & Fountain, 1995). The Nb/Ta magmatic-hydrothermal transition boundary in d is after Ballouard et al. (2016). Chondrite values in all plots are from McDonough and Sun (1995). Error bars are 2σ .

an important role in changing both physical properties and the primary chemical composition of the melt by exsolving fluids, which bear mobile elements (e.g. Ballouard et al., 2016; Holtz et al., 1995).

The insignificant role of fluids in the evolution of the SGC is shown by the weak lanthanide tetrad effects (Bau, 1996; Irber, 1999), typically below the level of analytical significance ($\pm 10\%$ of the abundance of lanthanides in the present study) ($t_{1,3} \sim 1$, Appendix III, Supplementary Material). Also, the CHARGE-AND-RADIUS-CONTROLLED (CHARAC) behaviour of trace element pairs (Bau, 1996) that retain their respective chondritic ratios such as Zr/Hf, Y/Ho and Sr/Eu (Fig. 11a–c), provides further evidence of a purely magmatic system rather than a system dominated by melt–fluid interaction during its evolution. Excluded from this generalization are the Nb/Ta ratios which range from chondritic values (17.6, McDonough & Sun, 1995) to as low as ~ 10 , but still are distinctly higher than the magmatic-hydrothermal marker (Nb/Ta ~ 5 , Ballouard et al., 2016) (Fig. 11d). Several studies attribute the fractionation between Nb and Ta in evolving melts to interaction with late magmatic fluids (e.g. Abu El-Rus et al., 2017; Ballouard et al., 2016; Tartèse & Boulvais,

2010). However, we exclude this hypothesis because the correlation between Nb/Ta and SiO_2 (Fig. 11d) is not conformable with the insignificant role of fluids in the evolution of SGC. Instead, we attribute the wide variation of Nb/Ta values within the SGC to either the crystallization of mineral phase(s) with different Kd_{Nb} and Kd_{Ta} such as rutile (e.g. Klemme, Blundy, & Wood, 2002; Linnen & Keppler, 1997) and/or amphibole (Foley, Tiepolo, & Vannucci, 2002), or to the presence of these minerals in the melting sources. This hypothesis is consistent with the apparent lack of miarolitic cavities, genetically related skarns, greisens and pegmatite bodies and solidus/subsolidus replacement textures within the SGC.

7.2. Island arc setting

The insignificant lanthanide tetrad effects and the CHARAC behaviour of trace element pairs are robust evidence that the initial trace element abundances have not been modified due to interaction with fluids during the evolution of the SGC magma. This implies that applying

Fig. 10. (a) The evolution of ϵ_{Nd} with time in individual samples within the SGC compared to the ϵ_{Nd} evolution of the chondritic mantle (CHUR) and depleted mantle (DM) according to the models of Goldstein et al. (1984). The single-stage depleted-mantle model ages (not shown for simplification) following Goldstein et al. (1984) ($T_{\text{DM-1}}$) (i.e. extrapolations of the evolution lines of the individual samples back to the DM line of Goldstein et al. (1984) using their present-day $^{147}\text{Sm}/^{144}\text{Nd}$ ratios) scatter widely. In the two-stage model ($T_{\text{DM-2}}$), the evolution lines for the individual samples from their time of crystallization to present time (corresponding to the second stage in the two-stage T_{DM} model of Milisenda et al., 1994) are based on their measured $^{147}\text{Sm}/^{144}\text{Nd}$ ratios, whereas the evolution lines from the time of crystallization to the intersection with the depleted mantle line of Goldstein et al. (1994) assuming an average crustal $^{147}\text{Sm}/^{144}\text{Nd}$ ratio of 0.134 (corresponding to the first stage in the two-stage T_{DM} model of Milisenda et al., 1994). The two-stage depleted-mantle model ages ($T_{\text{DM-2}}$) fall between 860 and 1000 Ma. The two-stage TDM for the mafic enclaves are not calculated since they resulted from melting of mantle wedge directly. (b) Plot showing the difference between Nd model age and the crystallization age (TC) for the Shaitian rocks. Data that yield $T_{\text{DM}} = \text{Tc Ma}$ or $< \text{Tc} + 300 \text{ Ma}$ are considered to come from juvenile (oceanic) crust, those producing $> \text{Tc} + 900 \text{ Ma}$ are considered to come from evolved (continental) crust, and those with $\text{Tc} + 300 \text{ Ma} < T_{\text{DM}} < \text{Tc} + 900 \text{ Ma}$ are from juvenile crust contaminated by evolved crust (Hargrove et al., 2006). Field of Paleoproterozoic to Archean continental crust of Khida terrane is based on the data Hargrove et al. (2006). Red symbols are TDM-1 ages. Unrealistic high $T_{\text{DM-1}}$ ages of samples S-24B and S-3A and the negative $T_{\text{DM-1}}$ age of sample S-122A are not shown.

tectonic setting discrimination diagrams to infer the geologic setting of SGC is reasonable. Using ratios of trace elements that are insensitive to secondary processes such as weathering, shearing and/or dynamic metamorphism, the diagrams of Pearce, Harris, and Tindle (1984), indicate a volcanic arc setting for the SGC (Fig. 12a, b). Given that the ANS is a group of island-arc terranes developed in the Mozambique Ocean at ~800–670 Ma, which converged and amalgamated as a result of intraoceanic subduction-driven arc–arc and ultimately arc–continent collisions at ~650–600 Ma (Johnson et al., 2011), the zircon ages of the SGC (~800 Ma to 717 Ma) most likely represent the early stages of the ANS magmatism.

7.3. Temperature estimation

Apatite and zircon are two mineral phases for which saturation temperatures have been calibrated experimentally as a function of melt composition (Watson, 1979; Watson & Harrison, 1984). The P_2O_5 content of all samples from the SGC are within analytical uncertainty, making application of apatite saturation thermometry inappropriate. In contrast, the high Zr contents (Appendix III, Supplementary Material), together with the presence of ubiquitous early crystallized zircon grains in all granite samples, suggest that the melt was saturated in Zr at the magma generation stage (Miller, Meschter-McDowell, & Mapes, 2003). Solubility of zircon is extremely sensitive to temperature, whereas, it is weakly sensitive to other factors such as pressure, low grade metamorphism and/or weathering (Miller et al., 2003; Watson, 1979; Watson & Harrison, 1984). Applying the zircon saturation geothermometry method of Watson and Harrison (1984), the tonalite yielded a T_{Zr} in the range from 701 to 804 °C with a mean of 745 ± 31 °C (2σ). This is significantly lower than those estimated for the trondhjemite samples (773–823 °C with a mean of 810 ± 25 °C) and the granodiorite samples (832–851 °C with a mean of 840 ± 10 °C, including two samples from El-Gaby, 1975). Monzogranite samples yield T_{Zr} values of 855 to 878 °C with a mean of 868 ± 10 °C (Appendix III, Supplementary Material; Fig. 13a).

It is noteworthy that there is an obvious correlation between the zircon saturation temperatures and the age of crystallization within the SGC (Fig. 13b). Using the T_{Zr} temperatures as a proxy for the source melting temperatures (Miller et al., 2003), the tonalite phase was apparently produced by partial melting at relatively lower temperatures (~800 Ma) compared to the other granitic phases within the SGC, which would place the tonalite in the intriguing group of ‘cold granite’

that is characterized by $T_{Zr} < 800$ °C (Miller et al., 2003). In contrast, the other granitic phases, trondhjemite, granodiorite and monzogranite, were generated at relatively higher temperatures placing them in the ‘hot granite group’ ($T_{Zr} > 800$ °C) of Miller et al. (2003). ‘Hot’ felsic magmas require advective heat input into the crust, whereas ‘cold’ magmas require only fluid influx (Miller et al., 2003).

7.4. Fractional crystallization versus partial melting

Felsic plutons with continuous compositional variations emplaced within subduction zones, such as Archean TTG suites and Phanerozoic high-Al tonalite-trondhjemite suites are usually interpreted as the result of: (1) extensive intracrustal fractional crystallization of melts derived from a metasomatized mantle wedge (e.g. Arth, Barker, Peterman, & Friedman, 1978; Tatsumi, 1989, 2) partial melting of either a subducted oceanic slabs (e.g. Defant & Drummond, 1990; Martin, 1999), or (3) overlying continental/arc crusts (e.g. Petford & Atherton, 1996; Smithies, 2000), or melting at the base of thick oceanic plateaus (e.g. Bédard, 2006; Martin, Moyen, Guitreau, Blichert-Toft, & Le Pennec, 2014). We will therefore briefly examine these hypotheses to constrain the origin of the SGC.

7.4.1. Extensive fractional crystallization hypothesis

7.4.1.1. Crystallization within closed system. Despite the SGC samples exhibiting linear or curvilinear trends between SiO_2 and several major and trace elements (Figs. 4 and 5), these trends cannot be attributed to simple crystal fractionation within a closed magma chamber because modelling of the liquid line of descent from the least siliceous sample cannot reproduce the variation trends observed in the complex (Fig. 14). Furthermore, all granite samples contain variable, but considerable, amounts of hornblende and biotite (up to 20 vol%, El-Fadly et al., 2018). Fractionation of such high amounts of these minerals from an siliceous melt would lead to strong depletion of the evolving melts in Nb, Zr, and Y due to their high compatibility in amphibole (Pearce & Norry, 1979) and in Rb and Cs owing to their high compatibility in biotite (Bea, Pereira, & Stroh, 1994). These trends are not observed in the SGC, which instead display weakly positive correlations of these elements with SiO_2 contents (Fig. 5). The flat REE patterns with relatively constant negative Eu anomalies in the tonalite, granodiorite and trondhjemite samples (Fig. 8) are evidence against plagioclase and K-feldspar fractionation; given Kd_{La} is ~4 and ~2.5 times that of Kd_{Lu} for plagioclase and K-

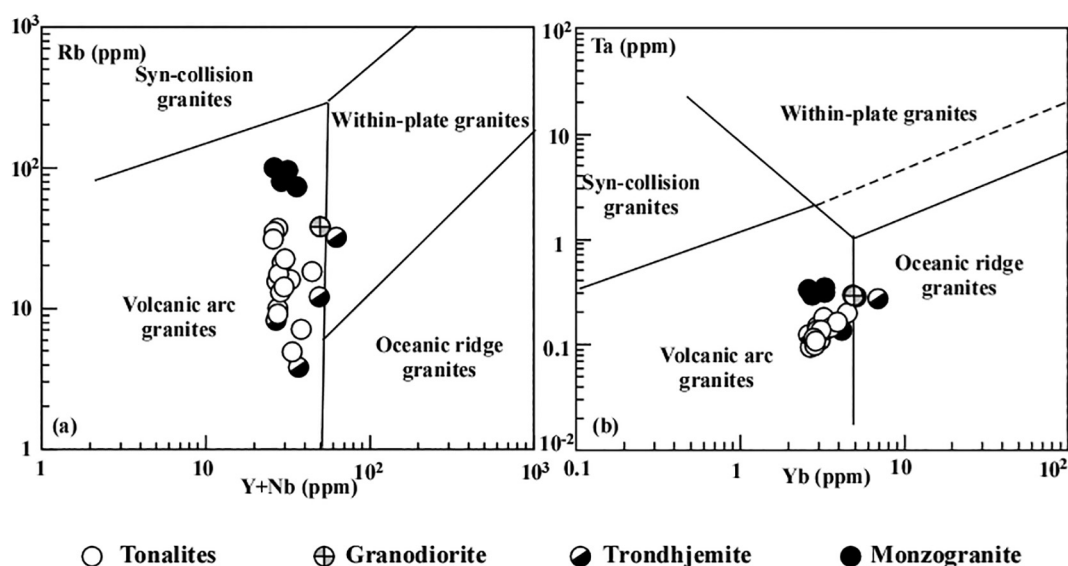


Fig. 12. (a, b) Tectonic discrimination diagrams of Pearce et al. (1984) illustrating the volcanic arc setting of the SGC. This setting is supported in diagrams.

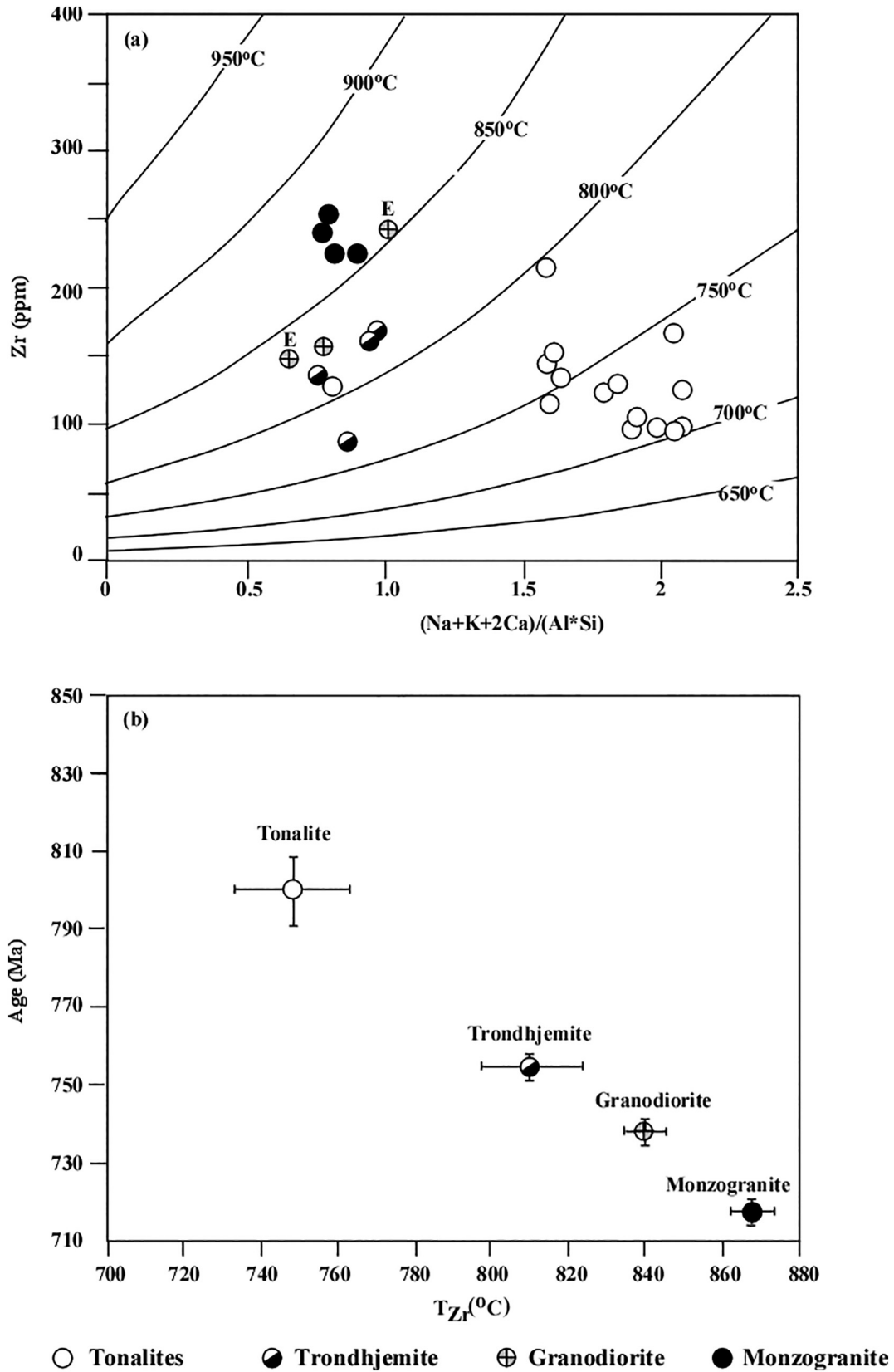


Fig. 13. (a) Temperature estimated from the relationship between the Zr (ppm) content and cation ratio $(Na + K + 2Ca)/(Al*Si)$ in the granite system (Watson & Harrison, 1984). Granodiorite samples labelled with E are from El-Gaby (1975). (b) Correlation between the mean zircon saturation temperatures and the age of crystallization within the SGC. Error bars are 2σ of the estimated ages and temperatures.

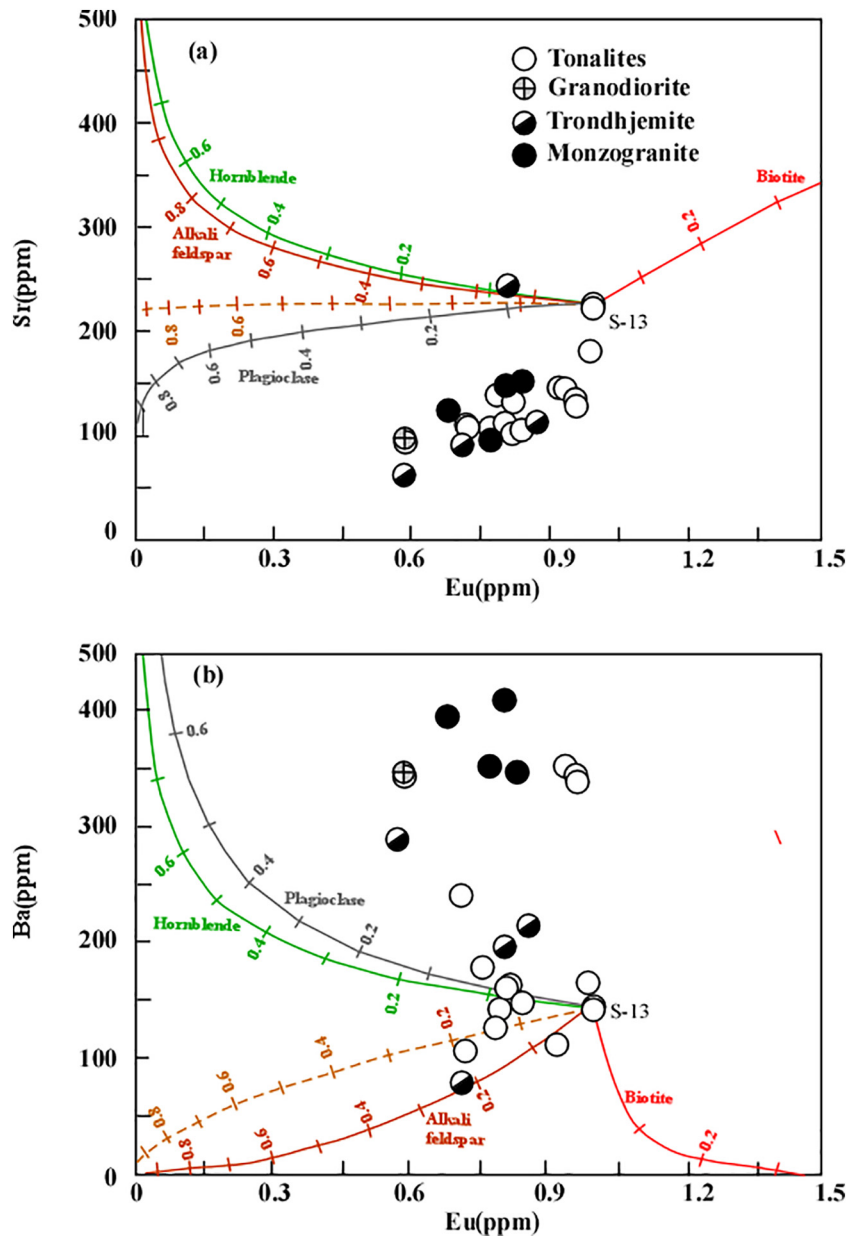


Fig. 14. Sr and Ba vs Eu variation diagrams comparing the Shaitian gneissose granites with liquid lines of descents calculated via Rayleigh fractionation from the least siliceous sample S-13 as a starting composition. Mineral vectors calculated for biotite, plagioclase and alkali feldspar are according to partition coefficients of Bea et al. (1994), whereas mineral vectors calculated for hornblende are based on partition coefficients of Klein, Stosch, and Seck (1997). The dashed lines represent the liquid line of descent if the fractionated assemblage consists of 50% plagioclase and 50% alkali feldspar. Tick marks represent 10% increments of the fractionating mineral.

feldspar, respectively (Nash & Crecraft, 1985). All of these lines of evidence, together with the difficulties of a single magma batch surviving over 80 million years (i.e. the time interval of crystallization of the SGC) without solidification, and the inverse time-temperature relations seen in Fig. 13B, make us rule out a closed magma chamber model.

7.4.1.2. Crystallization within open system. Despite the field observations and zircon U-Pb age dating that show that the SGC is a composite batholith formed of at least four granitic pluses emplaced intermittently over 80 million years, the tonalite, trondhjemite and granodiorite samples display coherent evolution trends for most major and trace elements, with only the monzogranite samples showing strong deviations (Figs. 4, 5). Furthermore, the similar initial ϵ_{Nd} values (Table 1) and ratios of several element pairs (Fig. 12) in these granite phases suggest a genetic-relationship. One possible explanation for these chemical features is the crystallization of magmatic pulses tapped from a deeper

long-lived magma chamber (Abu El-Rus, 1991; Hildreth & Wilson, 2007; Khudeir et al., 1996). Since thermal models reveal the difficulty of generating and sustaining magma in a large autonomous molten chambers in the crust for long periods without supply of a new magma and heat (e.g. Hildreth & Wilson, 2007; Schöpa & Annen, 2013), an alternative model would be that a deep-seated magma chamber grew incrementally over time through repeated recharging with disparate hotter magma batches, presumably derived from the underlying mantle (e.g. Abu El-Rus, 2003; Coleman, Gray, & Glazer, 2004; Hildreth & Wilson, 2007). The floor of the magma chamber in this case works as a hot plate, not as a heat sink.

Some lines of evidence, however, are not compatible with the secular tapping of a recharged, long-lived deep magma chamber paradigm. Firstly, it is difficult to reconcile that the ϵ_{Nd} values do not show any correlations with the crystallization ages nor with the crystallization temperature. Longer-lived and hotter magma batches are most likely

subjected to crustal contamination/mingling and hence would be expected to exhibit lower $\varepsilon_{\text{Nd}_i}$. Secondly, even if the injection of hot magma pulses was continuous, the resident magma within the chamber would always cool greatly below the injection magma temperature and, therefore, the temperature averaged over the total volume of the magmatic system will be lower than the initial magma injection temperature. This means an intrinsic decline in the temperature of the tapped melt pulses from the deeper magma chamber with time, which is inconsistent with the negative correlation between the T_{Zr} °C and the crystallization ages within the SGC (Fig. 13). Thirdly, the lack of disequilibrium features, such as alternating crystallization and resorption episodes, or hiatuses in the appearance of the constituent minerals either at the scale of thin sections, or on the pluton scale, renders any model of repeated replenishment unlikely. Lastly, it is hard to reconcile heating the magma chamber by injecting melt pulses without varied amounts of mingling with the resident magma, even in higher parts of the chamber (Hildreth & Wilson, 2007). The composition of the resident melt in the magma chamber therefore would be modified with time, which is inconsistent with the identical trace element patterns of tonalite, trondhjemite and granodiorite samples (Fig. 8). These factors lead to the conclusion that the model of a long-lived and complex zoned magma chamber in the lower crust is unlikely in the case of the SGC. Instead, we suggest that the different granite phases within the SGC most likely resulted from sporadic fusion of a melting source comprising a mineral assemblage buffering the trace element patterns of the melt fractions.

7.4.2. Melting source hypothesis

7.4.2.1. Characterization of the melting source.

The geochemistry of SGC samples can provide some constraints on the nature of the melting source. The flat HREE patterns on the chondrite-normalized diagrams (Fig. 8), and the relatively low Sr/Y ratios (<6) are evidence for the absence of garnet in the melting source, given K_{Lu} is ~7 times that of K_{Dy} and K_{Y} is ~7000 times of K_{Sr} (Bea et al., 1994). The sharp negative Eu anomalies in the chondrite-normalized REE patterns (Fig. 8) indicate the presence of plagioclase within the melting source. The presence of plagioclase in the source is also supported by the narrow range of Sr contents and the absence of negative correlation between Sr and (Na₂O + CaO) throughout the SGC (Fig. 15). The presence of plagioclase in the melting source would buffer Sr in the melts whereas its absence would produce melts with Sr contents reaching up to 10 times that in the melting source within the oceanic crust and correlate negatively with (Na₂O + CaO) (minus signs in Fig. 15; Zamora, 2000). Also, the relatively low Nb and Ta contents compared to La in chondrite-normalized trace elements patterns (Fig. 8) are usually taken as evidence for the presence of residual minerals with high Kd for Nb and Ta, such as rutile ($K_{\text{rut/liq}}$ for Nb and Ta are >20; Green & Pearson, 1987; Foley, Barth, & Jenner, 2000) or amphibole ($K_{\text{amph/liq}}$ for Nb and Ta in intermediate to felsic liquids are ~4, Pearce & Norry, 1979; Lemarchand, Villemant, & Calas, 1987). Yet melting of rutile bearing-protoliths would lead to melts with superchondritic Nb/Ta ratios (e.g. Foley et al., 2000; Klemme et al., 2002), whereas, the presence of residual amphibole in the melting source would lead to melts to subchondritic Nb/Ta ratios (e.g. Tiepolo, Bottazzi, Foley, Oberti, & Zanetti, 2001), as is the case in the SGC (Fig. 11d). The existence of residual Fe-Ti oxides within the melting source is inferred from the low TiO₂ (<0.78 wt%) and the sharp negative Ti anomalies in the multivariate trace element patterns (Fig. 8). Similarly, the existence of apatite (or other P-bearing minerals such as monazite) in the source is inferred from the low P₂O₅ concentrations in these rocks (below 0.16 wt%, except one sample at 0.3 wt%) and very deep negative P anomalies in the multivariate diagrams (Fig. 8), whereas Zr does not show any negative anomaly, indicating that Zr-bearing minerals (e.g. baddeleyite; zircon) were not a residual phase. In summary, the different granite phases within the SGC were derived from a protolith formed essentially of plagioclase, amphibole and Fe-Ti

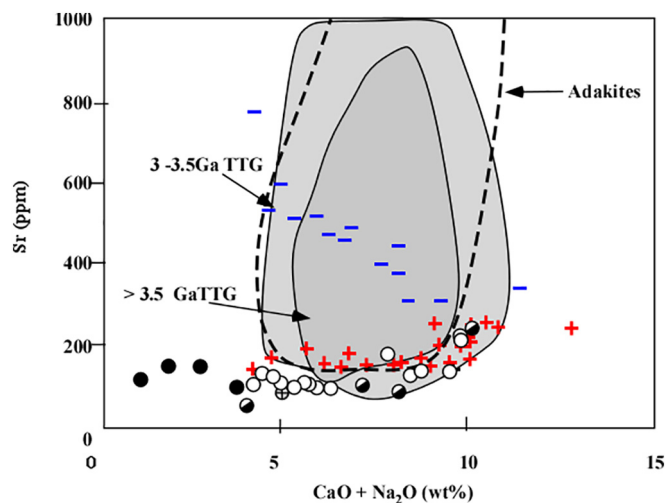


Fig. 15. (a) Sr (ppm) vs. Na₂O + CaO (wt%) diagram comparing the granitoid samples of the SGC with the compositions of experimental melts obtained with (+ signs) or without (- signs) residual plagioclase (Plg) (after Zamora, 2000) and with compositions of intermediate to acidic subduction-related TTGs and adakites (after Martin & Moyen, 2002).

oxides whereas garnet was absent. The high positive ε_{Nd} values and low Sr_i of the all SGC sample (excluding sample S-24A, Table 1) and the lack of old inherited zircons strongly suggest a mantle origin, or juvenile mafic rather than a crustal metasedimentary origin for the melting protolith.

7.4.2.2. Melting within the lower crust.

Generation of arc-related TTG melts is usually attributed to either differentiation of contaminated mantle wedge magmas within the lower continental crust (e.g. Castillo, Janney, & Solidum, 1999; Feeley & Hacker, 1995) or to partial melting, either within the subducted oceanic slab due to a high geothermal gradient (e.g. Drummond & Defant, 1990; Martin et al., 2005), or within overlying continental/island arc crust (e.g. Foley et al., 2002; Smithies, 2000; Zhang et al., 2009). However, the complete absence of genetically related fractionated mafic rocks, the lower Nb content within the SGC (<4 ppm) compared with Nb abundance in melts derived from the mantle-wedges (7–20 ppm; Defant et al., 1992), and the almost flat REE patterns exhibited by all tonalite, trondhjemite and granodiorite samples, argue against the highly fractionated mantle wedge magmas as possible source for the SGC. Furthermore, the following evidence supports a model of melting within the arc crust rather than melting within subducted oceanic crust:

- (1) The melts derived from the subducted slab must interact with and be contaminated by the overlying mantle wedge during their ascent, contrary to melts derived from continental/arc crust that avoid this fate (e.g. Rapp et al., 2003; Smithies, 2000). Interaction between slab-derived melts and the mantle wedge would certainly raise the MgO, Ni, and Cr contents of the melts, without changing their incompatible elements signature (e.g. Defant & Drummond, 1990; Foley et al., 2002; Rapp et al., 2003; Wolf & Wyllie, 1989). The granitic samples within the SGC exhibit low contents of MgO (<2.2 wt%), Ni (<8 ppm) and Cr (<13 ppm) (Appendix III Supplementary Material, Fig. 16a), which is inconsistent with equilibration, or reaction, with the mantle wedge (e.g. 20 ppm Ni and 41 ppm Cr mean values for High-SiO₂ adakites which represent subducted slab-melts interacted with mantle peridotite during ascending, Martin et al., 2005).
- (2) Melting of a subducted oceanic slab typically takes place under high pressure resulting in magma with high La/Yb_N and Sr/Y

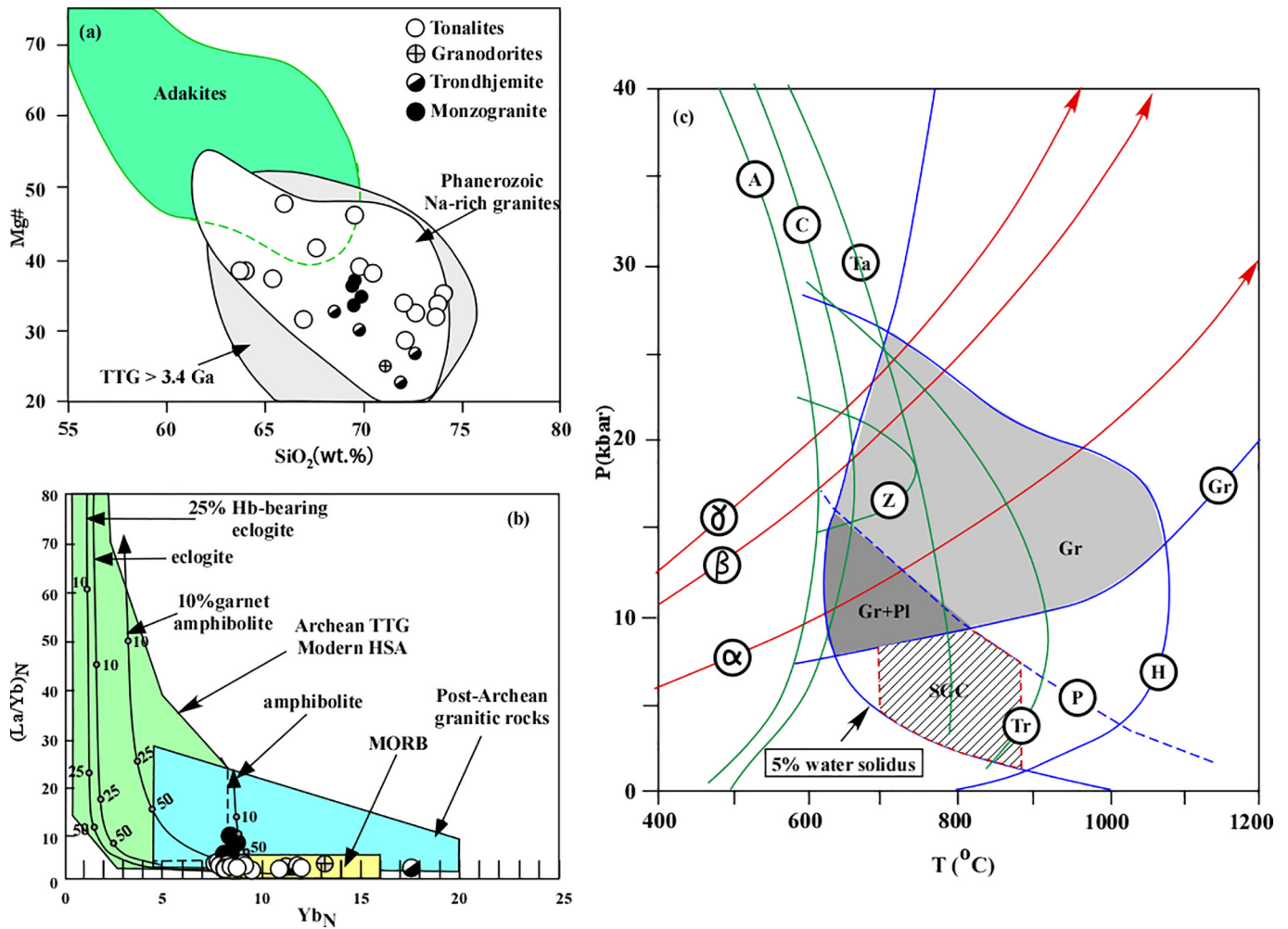


Fig. 16. (a) Mg# vs. SiO₂ variation diagram composed of the SGC with the compositional field of Phanerozoic Na-rich granitoid rocks, >3.4 Ga TTG and Cenozoic adakites. All fields are after Smithies (2000). (b) Chondrite-normalized (La/Yb)_N versus Yb_N diagram, modified after Jahn et al. (1981) and Martin (1986) showing the compositions of the granitoid phases within the SGC relative to the Archean trondhjemite-tonalite-granodiorite (TTG) field, post-Archean granitic rocks and the range of MORB values. Four partial melting curves are displayed two of which represent melting of amphibolite and 10% garnet amphibolite assuming a MORB source having Yb_N = 10 and (La/Yb)_N = 1, and the other two represent melting of eclogite and 25% hornblende eclogite, assuming a MORB source with Yb_N = 12 and (La/Yb)_N = 1 (after Drummond & Defant, 1990). Percent of partial melt values are listed on each of the model curves. (c) Pressure-temperature (P-T) diagram (after Martin & Moyen, 2002) showing the dehydration melting curves of the possible hydrous phases within oceanic crust as well as the geothermal gradients at various times and the stability fields of plagioclase and garnet. In the Early Archean (4.0 Ga), the geothermal gradient (α) was high and any subducted slab melted at shallow depth with plagioclase as a residual phase. At 2.5 Ga, the Earth was cooler and the geothermal gradient (β) was lower and slab melting occurred at greater depth without residual plagioclase. Overlying mantle wedge was thick and hot, and interactions may have occurred between slab melts and mantle peridotite. Geothermal gradient (γ) refers to modern adakites. P-T diagram shows solidus of tholeiite with 5% water as well as main dehydration reactions of oceanic lithosphere. H is hornblende out, A is anthophyllite out, C is chlorite out, Ta is talc out, Tr is tremolite out, Z is zoisite out. G and P outline stability fields of garnet and plagioclase, respectively. Grey field is P-T domain where slab melts can coexist with hornblende- and garnet-bearing residue. Striped area marked SGC represents the possible P-T melting conditions for melts forming the SGC; the melting temperatures are estimated from zircon saturation geothermometry (T_{zr} °C) whereas the upper and lower melting pressure as inferred from the absence of garnet and the presence of residual amphibole in the melting source, respectively.

ratios, leaving behind a residual assemblage involving garnet (e.g. Atherton & Petford, 1993; Martin et al., 2005). All SGC samples lack evidence for residual garnet in the melting source (Fig. 16b). The absence of garnet and the presence of plagioclase and amphibole within the melt source are consistent with melting at relatively shallower depths (Keller, Wunder, Rhede, & Abart, 2006) within the lower crust rather than melting of a subducted oceanic slab that occur at greater depth.

- (3) Thermal modelling of the Earth's interior indicates a reduction in the potential temperatures of the interior of the Earth with time. The potential temperatures were hot enough during Archean times to melt the descending oceanic crust within subduction zones even at shallower depths, whereas during the post-Archean times, the potential temperatures were normally not hot enough to produce whole-scale melting of subducted oceanic

lithosphere, but instead caused its dehydration (e.g. Defant & Drummond, 1990; Foley et al., 2002; Stern & Kilian, 1996). Exceptions to this rule occur when either the subducted oceanic crust is young, or the surrounding mantle is anomalously warm (e.g. Rapp, Watson, & Miller, 1991; Winther, 1996; Wolf & Wyllie, 1994). Based on this concept, the Earth's interior during post-Archean times is cool enough, and the geothermal gradient along Benioff zones is too low to induce slab melting except at depths beyond the plagioclase stability field (Martin & Moyen, 2002) (Fig. 16c), which is contrary to the compelling evidence for the existence of residual plagioclase and not garnet within the melting source of the SGC.

- (4) The compositional overlap between the granite lithologies within the SGC and the Phanerozoic Na-rich granitoids (Smithies, 2000; Fig. 16b) indicate partial melting of hydrated

basaltic materials at the base of magmatically or tectonically thickened crust (e.g. Kay, Godoy, & Kurtz, 2005; Petford & Atherton, 1996).

7.5. Acidic vs basaltic protolith

A large number of melting experiments demonstrate that the TTG melts can be reproduced from a wide range of igneous rocks formed essentially of plagioclase, amphibole and Fe-Ti oxides such as metatonalite and metadacite (e.g. Patiño Douce, 2005; Watkins et al., 2007) or amphibolite/eclogite of basaltic compositions (e.g. Beard & Lofgren, 1991; Qian & Hermann, 2013). Compared to the experimental melts, it is evident that the SGC tonalite and trondhjemite samples have too low K/Na and K/Ca ratios to be reproduced from melting of rocks with siliceous compositions (Fig. 17 a-c). In contrast, the samples are consistent with glasses produced from partial melting of basaltic rocks in the experiments of Rapp et al. (1991), Beard and Lofgren (1991), and Winther (1996) (Fig. 17 d-e). Granodiorite samples, on the other hand, can be reproduced either from melting tonalitic or basaltic composition (Fig. 17c, e). However, the identical chondrite-normalized trace element patterns of granodiorite, tonalite and trondhjemite samples (Fig. 8) and the formation of residual garnet in the melting

experiments of tonalite (Carroll & Wyllie, 1990), suggest that basaltic, and not a tonalitic protolith is most likely source. Furthermore, Fig. 18 shows that the tonalite-trondhjemite-granodiorite association within the SGC exhibit a trend more consistent with the partial melting of a basaltic protolith within the amphibolite facies rather than in the eclogite facies.

None of the partial melts from basaltic compositions can reproduce the K-rich melts that resemble the monzogranite phase within the SGC (Fig. 17d-f). The monzogranite samples, in contrast, fall within or close to the compositional fields of melts produced from fusion of the tonalites under various melting conditions (Fig. 17a, b). Furthermore, the melting experiments of Watkins et al. (2007) show that the formation of residual garnet only at $P > 10$ kbar, if the melting protolith is hornblende-bearing tonalite and $P > 8$ kbar in the case that the melting protolith is biotite-bearing tonalite. The unfractionated HREE in all monzogranite samples therefore strongly suggests that the melting of their protolith occurred at depth < 30 km.

7.6. Do the amphibolite enclaves represent the un-melted protolith?

The existence of basaltic (now amphibolitic) enclaves within the core of the SGC with distinct texture and mineral constituents away

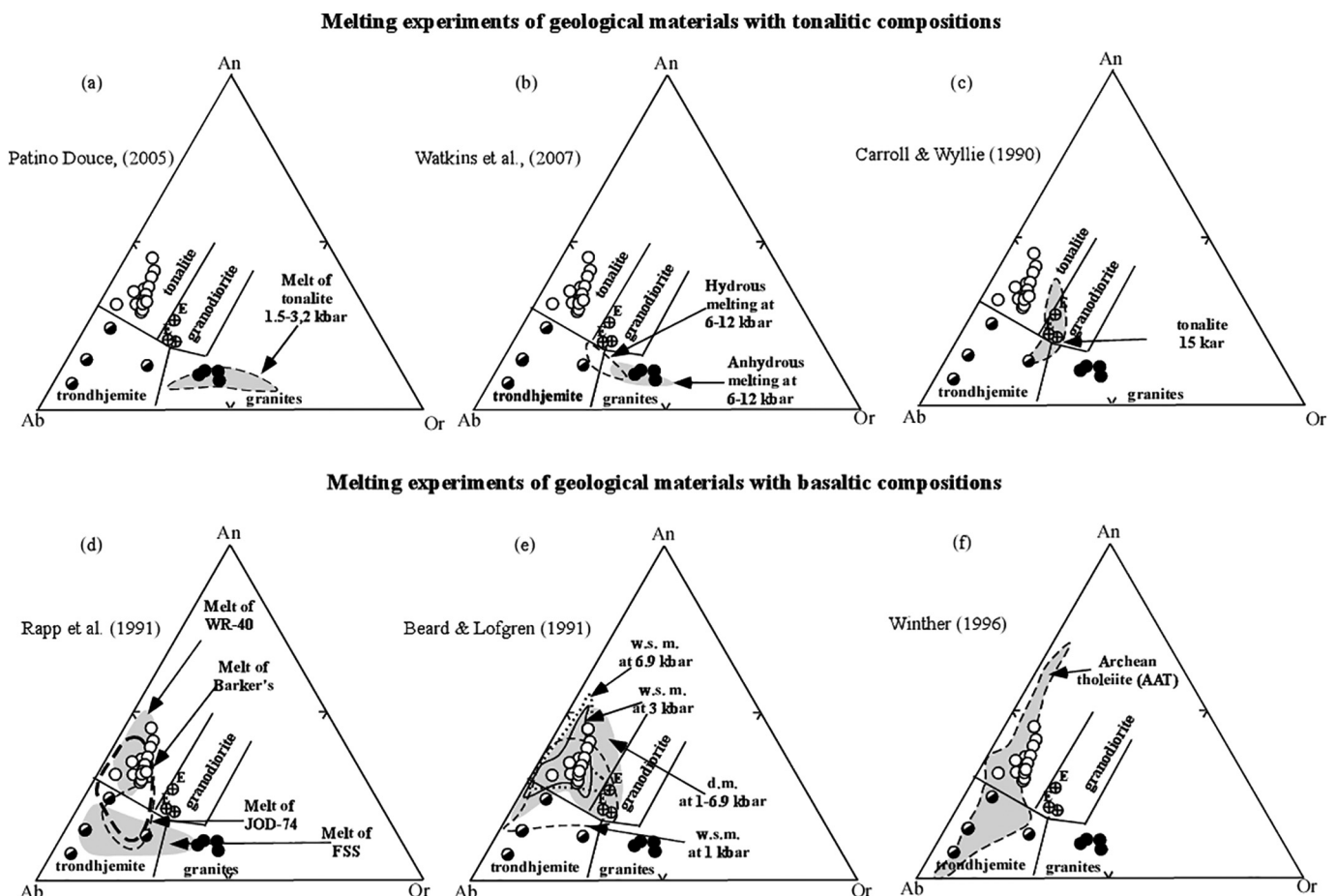


Fig. 17. Normative Ab-An-Or compositions of the SGC rocks compared with some experimental melts produced from felsic and basaltic compositions: (a) vapour-absent partial melting of tonalite, containing equal amounts of biotite and hornblende, at pressures of 15–32 kbar (Patiño Douce, 2005); (b) fluid-absent and fluid-present melting of hornblende- and biotite-bearing tonalitic gneisses at pressure 0.6–1.2 kbar (Watkins et al., 2007); (c) partial melting of tonalite with 2.5 to 10 wt% H₂O added at 15 kbar and 850 to 1100 °C (Carroll & Wyllie, 1990); (d) vapour-absent melting of natural basaltic compositions at pressure of 8–32 kbar (Rapp et al., 1991). Field labelled: JOD-74 is the melts derived from the uppermost pillow lava of Josephine ophiolite, California; FSS is the melts derived from Post Pond volcanics, Vermont; Barker's is the melts derived from amphibolitic oceanic tholeiite, Alaska, USA; and WR-40 is the melts derived from pillow lava of Roundtop Mtn. greenstone Wyoming; (e) partial melting of metamorphosed basalts (greenstones and amphibolites from Smartville arc complex of California) at pressures of 1–6.9 kbars (Beard & Lofgren, 1991). The experimental melting was carried out either under water saturated conditions ($P_{H_2O} = P_{total}$; w.s.m. field) or under vapour-absent conditions ($P_{H_2O} < P_{total}$; dehydration melting, d.m. field); and (f) partial melting of average Archean tholeiite (AAT) under pressure up to 30 kbar and temperature 750–1200 °C (Winther, 1996). Granodiorite samples labelled with E letter are from El-Gaby (1975). Nomenclature is after Barker (1979).

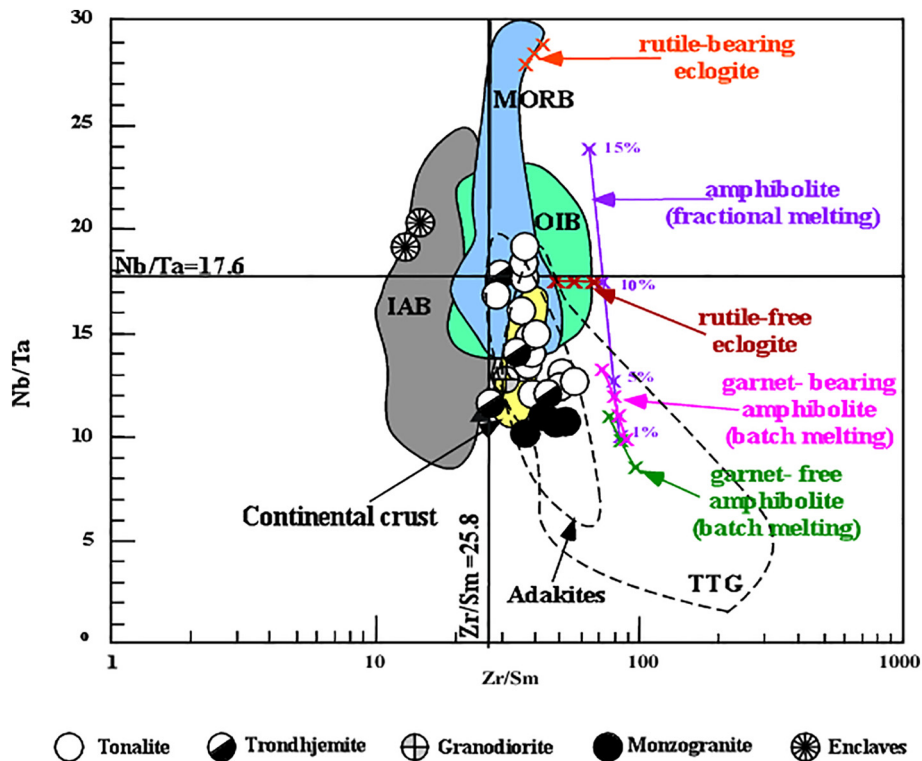


Fig. 18. Nb/Ta versus Zr/Sm within the SGC, compared to results of modeled melting of eclogites and amphibolites (after Foley et al., 2002). Trace-element modelling of partial melting of eclogite shows that batch and fractional melts of rutile-bearing eclogite lie in the upper right quadrant, and melt eclogites without rutile have unfractionated Nb/Ta. Trajectories of partial melting (1%–15%) of amphibolite are shown: batch melting of garnet-free amphibolite at 0.8 GPa, batch melting of garnet-bearing amphibolite at 1.6 GPa and pure fractional melting at 1.0 GPa. Note that only a few percent of fractional melting of amphibolite could result in the trace-element signature of the SGC as well as Archean TTG and modern adakites. For comparison are shown the fields of Archean trondhjemite–tonalite–granodiorite gneisses (TTG), modern adakites, modern mid-ocean-ridge basalts (MORBs), ocean-island basalts (OIB) and island-arc basalts (IAB) (Adapted from Foley et al., 2002). Chondrite reference lines are Nb/Ta = 17.6 and Zr/Sm = 25.8 (after McDonough & Sun, 1995).

from the surrounding rocks exclude the hypothesis that these mafic enclaves might be incorporated from the country rocks during magma emplacement, and instead suggests that these enclaves are possibly un-melted portions of the protolith. This hypothesis was evaluated using the equilibrium batch melting equation of Shaw (1970) and the trace element composition of the mafic enclaves S-24 and S-122A. The calculations were performed based on the following: (1) melting of the SGC protolith occurred at a pressure < 10 kbar in the absence of residual garnet (Rapp et al., 1991; Wolf & Wyllie, 1994; Zamora, 2000), but >3 kbar in the presence of residual amphibole (Beard & Lofgren, 1991); (2) the generation of SGC melts occurred at temperatures of 700–830 T_{Zr} °C (Appendix III, Supplementary Material), considerably below the dehydration-melting point of amphibolites (~900 °C at 5 to 10 kbar e.g. Beard & Lofgren, 1991; Wolf & Wyllie, 1994), but consistent with water saturated melting of amphibolites (~620 °C at 10 kbar; Thompson, 2001). Based on these arguments, the composition of melts derived from the amphibolite enclaves were calculated using the water-saturated melting reaction of Beard and Lofgren (1991) at 3 kbar:

9 quartz +4 amphibole+16 plagioclase +1 magnetite = 5 clinopyroxene+1 ilmenite +23 melt.

The results of modelling show that the TTG association within the SGC could not be modeled successfully by partial melting of the mafic enclaves (Fig. 19). The calculated melts exhibit more fractionated REE patterns with a distinct negative Eu anomaly compared with the TTG association (Fig. 19). Similarly, the calculated melts in equilibrium with the mafic enclaves exhibit different trace element abundances and patterns to those shown by the host tonalites (Fig. 19), which rules out the possibility that the enclaves are refractory residues. On the other hand, the complete absence of large crystals and cumulate textures in the

mafic enclaves are not fully consistent with the enclaves being fragments of early settled cumulates disrupted during magma moving upward. In addition, the contrasting modal and chemical composition of the mafic enclaves to the host tonalites are not consistent with the mafic enclaves representing clots of quickly-cooled upper zone fragments dragged downwards and randomly distributed in the magma chamber during the chaotic convection stage (e.g. Barbarin, 2005; Bea, 2010). Because neither textural evidence nor chemical composition supports the cognate origin of the mafic enclaves and the host tonalite, it is reasonable to suggest that the mafic enclaves represent a hot basaltic magma injected into a cooler tonalitic magma chamber. Given that the viscosities of the two magmas are sufficiently different to permit only mingling, the mafic magma would break up into blobs and be scattered in the granite magma to form mafic enclaves (e.g. Barbarin, 2005; Deyhimi et al., 2019). The limited occurrence of mafic enclaves in the tonalitic phase of ~800 Ma crystallization age and their absence in later granite phases that crystallized from 754 to 717 Ma, indicate that the addition of the mafic melt was not continuous and occurred only in the early stages of generation of granite melts within the SGC. This scenario is consistent with the role of mafic magmas in the initiation and evolution of calc-alkaline granitoid magmas related to subduction zones (e.g. Barbarin, 2005; Collins, Richards, Healy, & Ellison, 2000).

8. Evolution model of the SGC

Based on the field observations, bulk chemistry and zircon age constraints of the SGC rocks, we propose a four-stage evolution model for the emplacement of the SGC (Fig. 20): Stage 1: The creation of a mafic arc crust by partial melting of an mantle wedge above a subduction zone (Fig. 20a); Stage 2: Thickening of the new crust by intrusion and

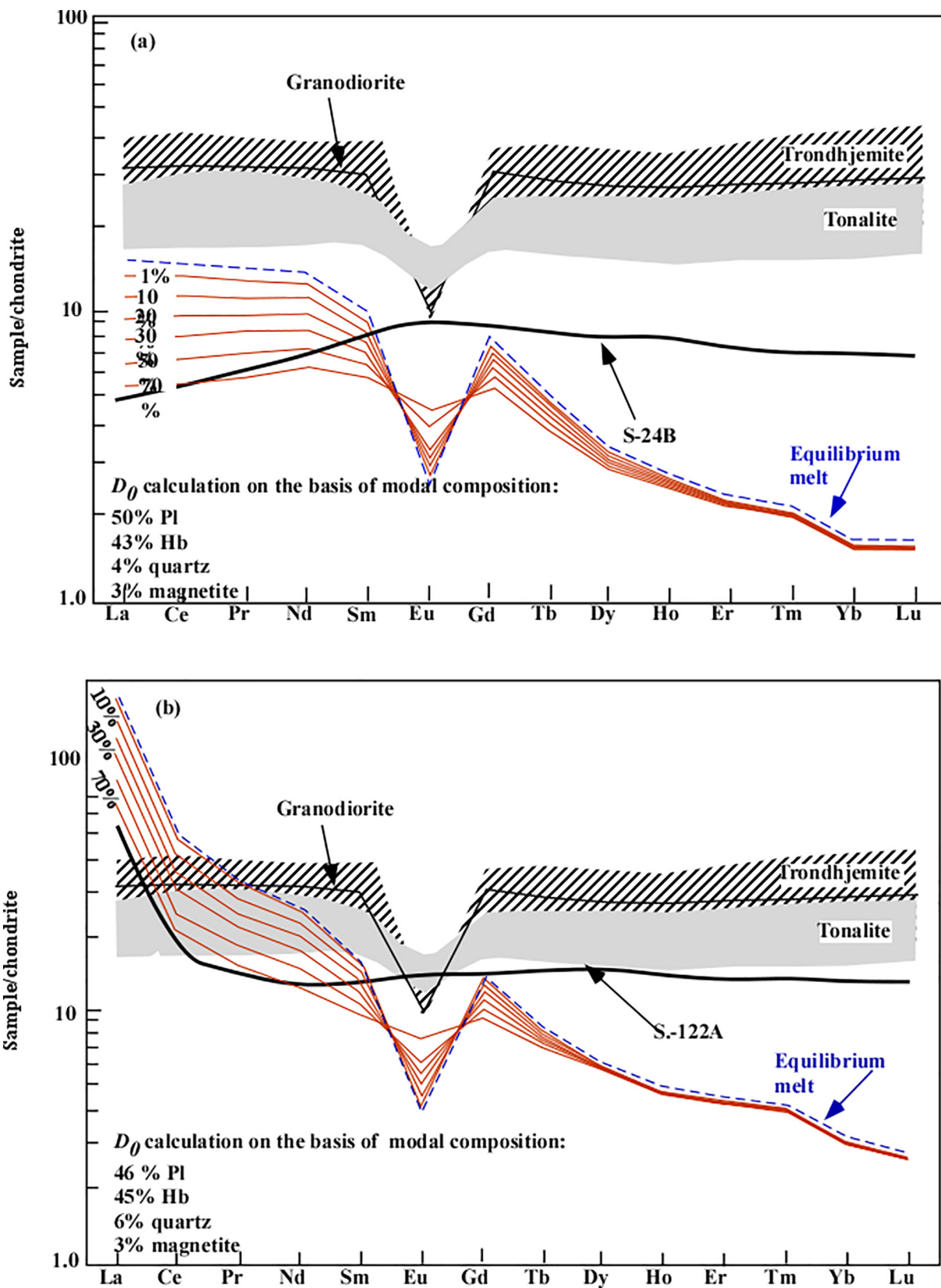


Fig. 19. The tonalite-trondhjemite-granodiorite samples within the SGC compared to the REE patterns (red colour) of the non-modal batch melts of mafic enclave S-24.B (a) and mafic enclave S-122-A(b). Figures on the lines represent the degree of partial melting. Blue line represents the equilibrium melt with the mafic enclaves at $F = 0$ (i.e. $C_{residual}/C_{melt} = D_{residual}$). The calculations were carried out using the partition coefficient in Appendix X (Supplementary Material) and modal and chemical analyses of the mafic enclaves. Normalization values are those of McDonough and Sun (1995).

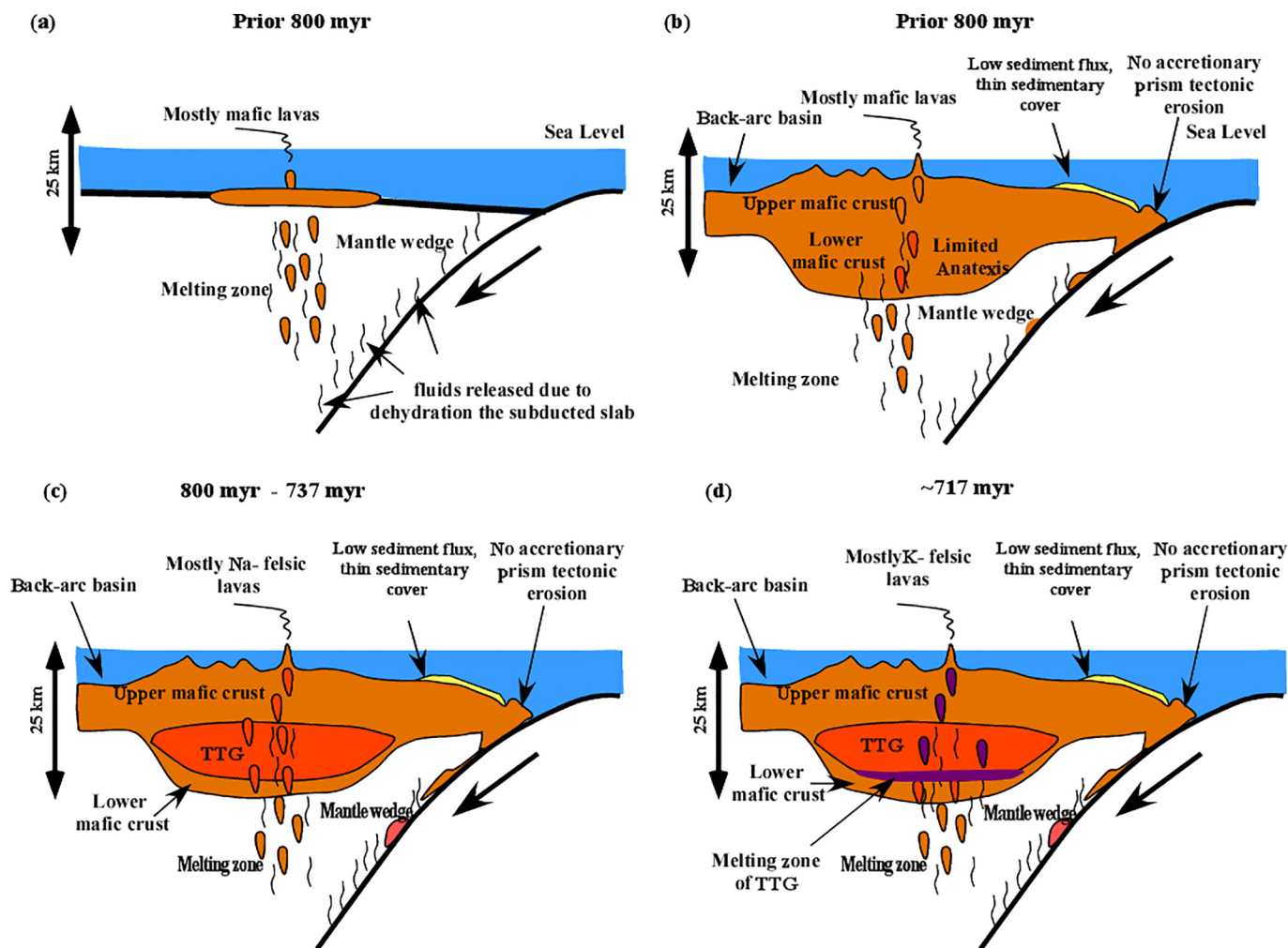


Fig. 20. Schematic geodynamic model (modified after Stern, 2002) showing the four-stages of the evolution of the SGC. (a) Subduction zones resulting from collision between young, hot buoyant oceanic slab and old, cold, dense oceanic slab. The latter is sinking into the hot mantle peridotites. The free water carried by the subducting oceanic slab as well as fluids released from breakdown of hydrous phases within it would metasomatize the overriding mantle wedge, lowering its solidus, and resulting in partial melting of it yielding basaltic magmas. (b) The ascending mafic magmas from the mantle wedge result in crustal thickening of the overriding oceanic crust forming island arc crust that is made essentially of basaltic rocks. Due to accumulation of heat from the underlying mantle wedge. (c) the newly accreted material itself undergoes episodic partial melting, giving rise to a sequence of tonalite (~800 Ma), trondhjemite (~754 Ma) and granodiorite (~737 Ma). (d) later on, the lower part of the newly formed TTG undergoes a partial melting event giving rise the monzogranite melt.

underplating of basaltic magma resulting from continuing partial melting within the upper mantle (Fig. 20b). Stage 3: Episodic partial melting of the accreted of basaltic material at the base of the island arc crust, giving rise to the sequence tonalite (~800 Ma), trondhjemite (~754 Ma) and granodiorite (~737 Ma) (Fig. 20c). Stage 4: Partial melting of the newly formed tonalite to yield monzogranite (~717 Ma) (Fig. 20d).

The presence of mafic enclaves of MORB affinity within the tonalites indicates that melting within the underlying mantle wedge was also occurring during the generation of the tonalite melt. The absence of interaction between most mafic enclaves and host tonalite indicates that the mingling between the tonalitic and basaltic melts may be due to either the injection of basaltic melt as the tonalite melt moved upward and therefore did not have enough time to thoroughly mix, or due to the relatively low volume of basaltic melt compared to the host felsic melt and therefore they chill rapidly with limited equilibration (Sparks & Marshall, 1986), or due to the wide contrast in temperature and density between the tonalitic and mafic melts. Given that the monzogranite samples fall within the field of experimental melts produced from partial melting of tonalites (Fig. 17) and the initial isotopic ratios of the monzogranite overlap with those of tonalite, trondhjemite and granodiorite samples (Table 2), we suggest that the monzogranitic magmas were formed by partial melting of the solidified TTG association due to

the basaltic underplating process. However, the heating of arc crust was not sufficient for complete breakdown of the amphibole and/or biotite in the protolith, as shown by the lower Nb/Ta ratios exhibited by the monzogranite samples compared to the TTG samples (Fig. 11d).

Eventually, after complete consolidation, the whole SGC was subjected to regional deformation, most probably during accretion of this island arc terrane to the Saharan Metacraton (arc-continent collisions) in the late Cryogenian-Ediacaran (650–542 Ma, Johnson et al., 2011).

9. Tectonic significance

The evolution of the SGC records more than 80 million years of crustal growth in the ANS, covering the period between 800 Ma and 717 Ma. It thus describes early to late Cryogenian (Neoproterozoic) events during the Pan African orogeny, which is a cycle of tectonic events (Johnson et al., 2011), extending from the breakup of Rodinia (870–800 Ma; e.g. Li et al., 2008) to the final amalgamation of the east and west Gondwana blocks in the Cambrian (e.g. Barbey et al., 2018; Johansson, 2014; Pisarevsky, Murphy, Cawood, & Collins, 2008).

The emplacement of the SGC as well as other synorogenic granite complexes within the ANS exhibiting island arcs traits (e.g. El-Gaby et al., 1988; Khudier, Abu El-Rus, et al., 2006; Khudier, Bishara, et al.,

2006; Khudeir et al., 2008; Andresen et al., 2010) corroborates the hypothesis of the formation of island arcs within the Mozambique Ocean, separating eastern and western Gondwana before their assembly during the late Cryogenian–Ediacaran (650–542 Ma Johnson et al., 2011). These island arc terranes resulted from subduction of older oceanic plates beneath younger oceanic lithospheres (e.g. Abu El-Rus, 1991; El-Gaby et al., 1988). Given that the post-Archean subducted oceanic lithosphere no longer intersected the wet basalt solidus before dehydration (as the Earth starts to cool around ~3.2 Ga, Gamal EL Dien, Doucet, Li, Cox, & Mitchell, 2019), it is reasonable to assume that the subducted oceanic slabs during the Pan-African Orogeny were dehydrated before melting, resulting in hydration of the overlying mantle wedge. The addition of water to the already hot mantle rocks lowered their melting temperature resulting in partial melting of ultramafic mantle rocks to yield mafic magma. Magma formed above a subducting plate slowly rising into the overlying crust and finally to the surface forming volcanic arc terranes.

With continuous melting within the mantle wedge, many magma pulses do not make their way to the surface before crystallizing within the crust or at the crust-mantle boundary (i.e. underplating basaltic layers). This hypothesis is consistent with the direct observations of exposed cross-sections of the lower crust and the crust-mantle transition, (e.g. Boudier, Nicolas, Kienast, & Mevel, 1988; Seyler & Bonatti, 1988), as well as the study of xenoliths from the lower crust (e.g. Abbo, Avigad, & Gerdes, 2018; Al-Mishwat & Nasir, 2004; McGuire & Stern, 1993), which show that the lower crust in the ANS is generally mafic in composition. At first, the underplating mafic layer presumably would be metamorphosed to plagioclase-bearing amphibolites (hydrated facies) due to conductive heat and fluid fluxes from the underlying mantle. By that time, the underplated mafic layer would have been subjected to partial melting due to the advective heat transported by large convection cells from the back-arc region, the heat flux from the asthenosphere mantle, the heat generation by decay of radionuclides within fluids released from subducted oceanic crust, the heat released from phase transformations within subducted oceanic crust, and/or the frictional or viscous heat release at the interface between the subducted oceanic slab and the overlying mantle wedge (e.g. Davies & Stevenson, 1992; Iwamori, 1997).

The emplacement of potassic granite melts subsequent to the emplacement of Na-rich granites is usually considered evidence of major crustal thickening following arc collision (Dong et al., 2018; Moyer et al., 2017). Therefore, we consider the emplacement of potassium-rich granite melts in the ANS as evidence that the island arcs terranes were mutually accreted and amalgamated into overthickened proto-crust of the Arabian-Nubian microcontinent (PANS; Johnson et al., 2011). The PANS was ultimately accreted to the Saharan Metacraton (arc-continent collisions) in the late Cryogenian to Ediacaran (650–542 Ma) during closure of the Mozambique Ocean and assembly of eastern and western Gondwana (Johnson et al., 2011).

10. Cessation of subduction stage versus initiation of the post-collisional extension

Granitic plutonism was extensive throughout the formation period of the ANS. Initially, it was characterized by arc-related magmatism of adakitic composition, then by collisional-related calc-alkaline assemblages and eventually by post-collisional and within-plate A-type granitoids that formed in extensional regimes (e.g. Abdel-Rahman, 2020; Cox, Foden, & Collins, 2019; Johnson et al., 2011). Some of these granitic suites have been identified as TTG suites of adakitic composition: Mons Claudianus Batholith (MCB) (664.12 ± 0.38 Ma; Abdel-Rahman, 2019) and Abu Fannani Igneous Complex (FIC) (607.4 ± 1.95 Ma; Abdel-Rahman, 2020) in the northern Arabian-Nubian Shield; Jebel Tays adakitic granites in the Ad Dawadimi Basin Terrane in the eastern Nubian-Arabian Shield (633.2 ± 9.0 Ma; Cox et al., 2019) and Birbir TTG in western Ethiopia (>800 Ma, Wolde & Team, 1996). Questions

remain as to the origin of these TTG magmatism and various hypotheses have been proposed: (1) partial melting of mafic material under-plating the lower crust (e.g. present study; Wolde & Team, 1996, 2) melting of mafic material delaminated from the lower crust of the overriding plate (Cox et al., 2019, 3) melting of the subducted slab (Abdel-Rahman, 2020; Cox et al., 2019); or (4) melting of contemporary subducted forearc mafic rocks (i.e. boninites) (e.g.; Abdel Rahman, 2018). These hypotheses would require heating of basaltic materials beyond their solidus in either the lower crust (800–950 °C at 10–12.5 kbar Qian & Hermann, 2013) or the downgoing oceanic slab (~1000 °C at 15 kbar, Peacock, Rushmer, & Thompson, 1994). Considering that the mantle potential temperature of the ambient upper mantle during post-Archean times typically insufficient to produce melting of the lower crust of the overriding plate or the downgoing subducted oceanic (e.g. Cox et al., 2019; Defant & Drummond, 1990; Foley et al., 2002; Stern & Kilian, 1996), we conceive that a tearing or break-off in the subducted slab would have opened a window allowing inflow from underlying oceanic asthenosphere into the mantle wedge. The influx of hot asthenosphere would heat the mantle wedge, cease the subduction stage and initiate the post-collisional and extensional regime in ANS. This hypothesis would explain the emplacement of A-type magmatism postdating island-arc magmatism in the ANS (e.g. Abdel-Rahman, 2020; Abu El-Ela, Abu El-Rus, Mohamed, & Gahlan, 2017; Cox et al., 2019; El-Gaby et al., 1988; Johnson et al., 2011). A similar mechanism has been proposed by Harris, Pearce, and Tindle (1986), Robinson, Foden, and Collins (2015a, 2015b) and Cox et al. (2019) to explain the transition from the early sub-arc mantle wedge, to a relatively enriched asthenospheric mantle under the Arabian-Nubian Shield. The presence of TTGs in the ANS can therefore pinpoint the timing of the slab breaking-off, thereby marking the terminal stages of arc magmatism, terrane accretion and the influx of hot asthenosphere mantle. Furthermore, the presence of TTG of age ~ 607.4 Ma (Abdel-Rahman, 2020) is robust evidence that the subduction and associated arc-magmatism continued beyond ~620 Ma, an age that is proposed for the cessation of subduction stage and initiation of the post-collisional extensional regime in the ANS (e.g. Jarrar et al., 2013; Eyal, Beéri-Shlevin, Eyal, Whitehouse, & Litvinovsky, 2014; Eyal et al., 2019; Elisha, Kylander-Clark, & Katzir, 2017; Elisha, Katzir, Kylander-Clark, Golan, & Coble, 2019).

11. Future work

The present study demonstrates that the Neoproterozoic TTGs within the ANS are produced due to the influx of hot asthenospheric mantle within mantle wedge, contrary to those of Archean-Palaeoproterozoic age that produced due to the steep geothermal gradient within mantle wedge (e.g. Defant & Drummond, 1990; Foley et al., 2002; Martin, 1986; Stern & Kilian, 1996). However, generalization this hypothesis needs a detailed comparative study of TTG of various ages from different orogenies, which could be a subject for further study in future.

12. Summary and conclusions

- (1) Zircon U-Pb dating indicates crystallization of the granitic phases within the SGC from disparate magma pulses over a period extending from ~800 Ma to 717 Ma. The low Sr_i and high positive ϵ_{Nd_i} indicate that the source of the magmas was juvenile material without any significant input from older crust.
- (2) Major and trace element compositions indicate the emplacement of the SGC within a subduction zone setting from melting of a lower crust of an island arc terrane overlying a mantle wedge.
- (3) Comparison to melt glasses reproduced experimentally suggests that amphibolite of basaltic composition is the best candidate as a melting source for the tonalite, trondhjemite and granodiorite

phases, whereas the monzogranite phase, can be produced from fusion of a tonalite protolith.

- (4) The emplacement of potassic granite (monzogranite) subsequent to the emplacement of Na-rich granites (tonalite-trondhjemite-granodiorite) is consistent with major crustal thickening following arc collision and amalgamation into overthickened proto-crust of the Arabian-Nubian microcontinent (PANS).
- (5) The emplacement of TTG massifs in the ANS marks the time of cessation of subduction stage and initiation of post-collisional and/or extensional regime.

Declaration of interests

The authors declare that they have no known competing financial interests or personal relationships that could have appeared to influence the work reported in this paper.

Declaration of Competing Interest

None.

Acknowledgments

The present manuscript is the outcome of a joint research project between Assiut University, Université Clermont- Auvergne, Ball State University, Swedish Museum of Natural History, Michigan State University and Notre Dame University. Field work was carried out with logistical and financial support from the Geology Department, Assiut University. Major and trace elements analyses were carried out with a grant from Science & Technology Development Fund (STDF) to Ali Abu El-Rus (contract no. 6107). U-Pb analyses of zircons were funded through a Ball-State University internal grant to K. Nicholson and S. Malone. Constructive comments by A. Abbo, H. Gamal El Dien, an anonymous reviewer, associate editor C. Spencer and editorial advisor M Santosh contributed to improving the original manuscript.

Appendix A. Supplementary data

Supplementary data to this article can be found online at <https://doi.org/10.1016/j.gsf.2021.101148>.

References

- Abbo, A., Avigad, D., Gerdes, A., 2018. The lower crust of the Northern broken edge of Gondwana: Evidence for sediment subduction and syn-Variscan anorogenic imprint from zircon U-Pb-Hf in granulite xenoliths. *Gondwana Res.* 64, 84–96.
- Abdel-Rahman, A.M., 2019. Geochemistry, age and origin of the Mons Claudianus TTG batholith (Egypt): Insight into the role of Pan-African magmatism in uniting plates of Gondwana. *Geol. Mag.* 156, 969–988.
- Abdel-Rahman, A.M., 2020. Petrogenesis of a rare Ediacaran tonalite-trondhjemite-granodiorite suite, Egypt, and implications for Neoproterozoic Gondwana assembly. *Geol. Mag.* <https://doi.org/10.1017/S0016756820000795>.
- Abu El-Ela, F.F., Abu El-Rus, M.A., Mohamed, M.A., Gahlan, H.A., 2017. Cold plutonism in the Arabian-Nubian Shield: evidence from the Abu Diab garnet-bearing leucogranite, central Eastern Desert, Egypt. *J. Geol. Soc. London* 174, 1031–1047.
- Abu El-Rus, M.A., 1991. Geological studies on Abu Ghalaga area, Eastern Desert, Egypt. M.S. thesis. Assiut University 255 pp.
- Abu El-Rus, M.A., 2003. Trace element modelling of magma evolution in the Fongen-Hyllingen Intrusion, Trondheim region. *Norway J. Mineral. Petrol. Sci.* 98, 47–76.
- Abu El-Rus, M.A., Chazot, G., Vannucci, R., Paquette, J., 2018. Tracing the HIMU component within Pan-African lithosphere beneath northeast Africa: Evidence from Late Cretaceous Natash alkaline volcanics, Egypt. *Lithos* 300–301, 136–153.
- Abu El-Rus, M.A., Mohamed, A.M., Lindh, A., 2017. Mueilha rare metals granite, Eastern Desert of Egypt: An example of a magmatic-hydrothermal system in the Arabian-Nubian Shield. *Lithos* 294–295, 362–382.
- van Achterbergh, E., Ryan, C.G., Jackson, S.E., Griffin, W.L., 2001. Data reduction software for LA-ICP-MS. In: *Sylvester, P. (Ed.), Laser ablation-ICPMS in the earth science*. 29. Mineralogical Association of Canada, pp. 239–243.
- Akaad, M.K., Noweir, A.M., 1980. Geology and lithostratigraphy of the Arabian Desert orogenic belt of Egypt between latitudes 25°35'N and 26°30'N. *Inst. Appl. Geol. Bull. (King Abdulaziz Univ. Jeddah)* 3, 127–135.
- Al-Mishwat, A.T., Nasir, S.J., 2004. Composition of the lower crust of the Arabian Plate: A xenolith perspective. *Lithos* 72, 45–72.
- Andresen, A., Abu El-Rus, M.A., Myhre, P.L., Boghdady, G.Y., Corfu, F., 2009. U-Pb TIMS age constraints on the evolution of the Neoproterozoic Meatiq Gneiss Dome, Eastern Desert, Egypt. *Int. J. Earth Sci.* 98, 481–497.
- Andresen, A., Augland, L., Boghdady, G., Lundmark, A., Elnady, O., Hassan, M., Abu El-Rus, M.A., 2010. Structural constraints on the evolution of the Meatiq gneiss dome (Egypt). *East-African Orogen. J. Afr. Earth Sci.* 57, 413–422.
- Arndt, N., 2013. Formation and evolution of the continental crust. *Geochem. Perspect. Lett.* 2, 405–533.
- Arth, J.G., Barker, F., Peterman, Z.E., Friedman, I., 1978. Geochemistry of the gabbro-diorite-tonalite-trondhjemite suite of south-west Finland and its implications for the origin of tonalite and trondhjemite magmas. *J. Petrol.* 19, 289–316.
- Atherton, M.P., Petford, N., 1993. Generation of sodium-rich magmas from newly underplated basaltic crust. *Nature* 362, 144–146.
- Balouard, C.M., Poujol, M., Boulvais, P., Branquet, Y., Tartèse, R., Vigneresse, J.L., 2016. Nb-Ta fractionation in peraluminous granites: A marker of the magmatic-hydrothermal transition. *Geology* 44, 231–234.
- Barbarin, B., 2005. Mafic magmatic enclaves and mafic rocks associated with some granitoids of the central Sierra Nevada batholith, California: Nature, origin, and relations with the hosts. *Lithos* 80, 155–177.
- Barbey, P., Denèle, Y., Paquette, J.L., Berger, J., Ganne, J., Roques, D., 2018. The Marbat metamorphic core-complex Southern Arabian Peninsula: Reassessment of the evolution of a Tonian island-arc from petrological, geochemical and U-Pb zircon data. *Pre-cambrian Res.* 305, 91–110.
- Barker, F., 1979. Trondhjemite: Definition, environment and hypotheses of origin. In: *Barker, F. (Ed.), Trondhjemites, Dacites and Related Rocks*. Elsevier, Amsterdam, pp. 1–12.
- Barovich, K.M., Patchett, P.J., 1992. Behavior of isotopic systematics during deformation and metamorphism: A Hf, Nd and Sr isotopic study of mylonitized granite. *Contrib. Mineral. Petrol.* 109, 386–393.
- Bau, M., 1996. Controls on the fractionation of isoivalent trace elements in magmatic and aqueous systems: Evidence from Y/Ho, Zr/Hf, and lanthanide tetrad effect. *Contrib. Mineral. Petrol.* 123, 323–333.
- Bea, F., 2010. Crystallization dynamics of granite magma chambers in the absence of regional stress: Multiphysics modeling with natural examples. *J. Petrol.* 51, 1541–1569.
- Bea, F., Pereira, M.D., Stroh, A., 1994. Mineral/leucosome trace-element partitioning in a peraluminous migmatite (a laser ablation-ICP-MS study). *Chem. Geol.* 117, 291–312.
- Beard, J.S., Lofgren, G.E., 1991. Dehydration melting and water-saturated melting of basaltic and andesitic greenstones and amphibolites at 1, 3 and 6.9 kb. *J. Petrol.* 32, 465–501.
- Bédard, J.H., 2006. A catalytic delamination-driven model for coupled genesis of Archaean crust and sub-continental lithospheric mantle. *Geochem. Cosmochim. Acta.* 70, 1188–1214.
- Béeri-Shlevin, Y., Katzir, Y., Blichert-Toft, J., Kleinhanns, I.C., Whitehouse, M.J., 2010. Nd-Sr-Hf-O isotope provinciality in the northernmost Arabian-Nubian Shield: Implications for crustal evolution. *Contrib. Mineral. Petrol.* 160, 181–201.
- Boudier, F., Nicolas, A.J.S., Kienast, J.R., Mevel, C., 1988. The gneiss of Zabargad Island: Deep crust of a rift. *Tectonophysics* 150, 209–227.
- Brown, G.C., 1986. Processes and problems in the continental lithosphere: Geological history and physical implications. In: *Snelling, N.J. (Ed.), Geochronology and geological record*. *Geol. Soc. Lond. Mem* 10, pp. 326–346.
- Carroll, M.R., Wyllie, P.J., 1990. The system tonalite-H₂O at 15 kbar and the genesis of calc-alkaline magmas. *Amer. Miner.* 75, 345–357.
- Castillo, P.R., Janney, P.E., Solidum, R.U., 1999. Petrology and geochemistry of Camiguin Island, southern Philippines: Insights to the source of adakites and other lavas in a complex arc setting. *Contrib. Mineral. Petrol.* 134, 33–51.
- Cawood, P.A., Hawkesworth, C.J., Dhuime, B., 2013. The continental record and the generation of continental crust. *Geol. Soc. Am. Bull.* 125, 14–32.
- Champion, D., 2013. Neodymium depleted mantle model age map of Australia Explanatory notes and user guide. *Geosci. Aus. Res.* 44, 209.
- Coleman, D.S., Gray, W., Glazer, A.F., 2004. Rethinking the emplacement and evolution of zoned plutons: Geochronologic evidence for incremental assembly of the Tuolumne Intrusive Suite, California. *Geology* 32, 433–436.
- Collins, W.J., Richards, S.R., Healy, B.E., Ellison, P.L., 2000. Origin of heterogeneous mafic enclaves by two-stage hybridization in magma conduits (dykes) below and in granitic magma chambers. *Trans. R. Soc. Edinburgh. Earth Sci.* 91, 27–45.
- Cox, G.M., Foden, J., Collins, A.S., 2019. Late Neoproterozoic adakitic magmatism of the eastern Arabian Nubian Shield. *Geosci. Front.* 10, 1981–1992.
- Davies, J.H., Stevenson, D.J., 1992. Physical model of source region of subduction zone volcanics. *J. Geophys. Res.* 97, 2037–2070.
- Defant, M.J., Drummond, M.S., 1990. Derivation of some modern arc magmas by melting of young subducted lithosphere. *Nature* 347, 662–665.
- Defant, M.J., Jackson, T.E., Drummond, M.S., De Boer, J.Z., Bellon, H., Feigenson, M.D., Maury, R.C., Stewart, R.H., 1992. The geochemistry of young volcanism throughout western Panama and southeastern Costa Rica: An overview. *J. Geol. Soc. London* 149, 569–579.
- Deyhimi, M., Kananiana, A., Mirnejad, H., Sepidbar, F., Vlastelic, I., Paquette, J.L., Barbarin, B., 2019. Zircon U-Pb geochronology, major-trace elements and Sr-Nd isotope geochemistry of Mashhad granodiorites (NE Iran) and their mafic microgranular enclaves: Evidence for magma mixing and mingling. *Int. Geol. Rev.* <https://doi.org/10.1080/00206814.2019.1600435>.
- Dickin, A.P., 1995. *Radiogenic Isotope Geology*. Cambridge University Press, Cambridge 452 pp.
- Dong, G., Luo, M., Mo, X., Zhao, Z., Dong, L., Yu, X., Wang, X., Li, X., Huang, X., Liu, Y., 2018. Petrogenesis and tectonic implications of early Paleozoic granitoids in East Kunlun

- belt Evidences from geochronology, geochemistry and isotopes. *Geosci. Front.* 9, 1383–1397.
- Drummond, M.S., Defant, M.J., 1990. A model for trondhjemite \pm tonalite \pm dacite genesis and crustal growth via slab melting: Archean to modern comparisons. *J. Geophys. Res.* 95, 21503–21521.
- El-Fadly, M.A., Hamid, S., Abu-El-Rus, M.A., Khudeir, A.A., 2018. An inquiry into the structural evolution of the Neoproterozoic Shait granite complex, South Eastern Desert, Egypt. *J. Geol., Assiut Univ.* 47, 1–16.
- El-Gaby, S., 1975. Petrochemistry of some granites from Egypt. *Neues Jahrb Mineral Abh* 124, 147–189.
- El-Gaby, S., El-Aref, M., 1977. Geological, petrochemical and geochemical studies on the Shait granite at Wadi Shait, Eastern Desert Egypt. *Bull. Fac. Sci. Assiut Univ.* 6, 307–339.
- El-Gaby, S., List, F.K., Tehrani, R., 1988. Geology, evolution and metallogenesis of the Pan-African Belt in Egypt. In: El Gaby, S., Greiling, R. (Eds.), *The Pan-African belt of NE Africa and adjacent areas, tectonic evolution and economic aspects*. Vieweg, Braunschweig, Wiesbaden, pp. 17–68.
- Elisha, B., Katzir, Y., Kylander-Clark, A., Golan, T., Coble, M.A., 2019. The timing of migmatization in the northern Arabian–Nubian Shield: Evidence for a juvenile sedimentary component in collision-related batholiths. *J. Metamorph. Geol.* 37, 591–610.
- Elisha, B., Kylander-Clark, A., Katzir, Y., 2017. Ediacaran (~620 Ma) high-grade regional metamorphism in the northern Arabian Nubian Shield: U-Th-Pb monazite ages of the Elat schist. *Precambrian Res.* 295, 172–186.
- El-Kaluobi, B.A., El-Ramly, M.F., 1991. Nomenclature, origin and tectonic setup of the granite suite at Wadi Shait, South Eastern Desert, Egypt. *Ann. Geol. Surv. Egypt XVII* 1–17.
- Eyal, M., Be'eri-Shlevin, Y., Eyal, Y., Whitehouse, M.J., Litvinovsky, B., 2014. Three successive Proterozoic island arcs in the Northern Arabian–Nubian Shield: Evidence from SIMS U-Pb dating of zircon. *Gondwana Res.* 25, 338–357.
- Eyal, Y., Eyal, M., Litvinovsky, B., Jahn, B.M., Calvo, R., Golan, T., 2019. The evolution of the Neoproterozoic Elat Metamorphic Complex, northernmost Arabian–Nubian Shield: Island arc to synconcolitional stage and post-collisional magmatism. *Precambrian Res.* 320, 137–170.
- Feeley, T.C., Hacker, M.D., 1995. Intracrustal derivation of Na-rich andesite and dacite magmas: an example from Volcán Ollagüe, Andean Central Volcanic Zone. *J. Geol.* 103, 213–225.
- Foley, S., Tiepolo, M., Vannucci, R., 2002. Growth of early continental crust controlled by melting of amphibolite in subduction zones. *Nature* 417, 837–840.
- Foley, S.F., Barth, M.G., Jenner, G.A., 2000. Rutile/melt partition coefficients for trace elements and an assessment of the influence of rutile on the trace element characteristics of subduction zone magmas. *Geochem. Cosmochim. Acta* 64, 933–938.
- Fowler, A.R., Khamees, H., Dowidar, H., 2007. El Sibai gneissic complex, Central Eastern Desert, Egypt: Folded nappes and syn-kinematic gneissic granitoid sheets—not a core complex. *J. Afr. Earth Sci.* 49, 119–135.
- Fritz, H., Dallmeyer, D.R., Wallbrecher, E., Loizenbauer, J., Hoinkes, G., Neumayr, P., Khudeir, A.A., 2002. Neoproterozoic tectonothermal evolution of the Central Eastern Desert, Egypt: A slow velocity tectonic process of core complex exhumation. *J. Afr. Earth Sci.* 34 (3–4), 137–155.
- Gamal EL Dien, H., Doucet, L.S., Li, Z.-X., Cox, G., Mitchell, R., 2019. Global geochemical fingerprinting of plume intensity suggests coupling with the supercontinent Cycle. *Nat. Commun.* 10, 5270. <https://doi.org/10.1038/s41467-019-13300-4>.
- Goldstein, S.L., O'Nions, R.K., Hamilton, P.J., 1984. A Sm–Nd isotopic study of atmospheric dusts and particulates from major river systems. *Earth Planet Sci. Lett* 70, 221–236.
- Green, T.H., Pearson, N.J., 1987. An experimental study of Nb and Ta partitioning between Ti-rich minerals and silicate liquids at high pressure and temperature. *Geochem. Cosmochim. Acta* 51, 55–62.
- Halla, J., 2020. The TTG-amphibolite terrains of arctic fennoscandia: Infinite networks of amphibolite metatexite - diatexite transitions. *Front. Earth Sci.* 8, 252. <https://doi.org/10.3389/feart.2020.00252>.
- Hargrove, U.S., Stern, R.J., Kimura, J.I., Manton, W.I., Johnson, P.R., 2006. How juvenile is the Arabian–Nubian Shield? Evidence from Nd isotopes and pre-Neoproterozoic inherited zircon in the Bi'r Umq suture zone, Saudi Arabia. *Earth Planet Sci. Lett* 252, 308–326.
- Harris, N.B.W., Pearce, J.A., Tindle, A.G., 1986. Geochemical characteristics of collision zone magmatism. In: Coward, M.P., Ries, A.C. (Eds.), *Collision Tectonics*. Geol. Soc. Lond. Spec. Publ. 19, pp. 67–81.
- Hart, W.K., Wolde Gabriel, G., Walter, R.C., Mertzman, S.A., 1989. Basaltic volcanism in Ethiopia: Constraints on continental rifting and mantle interactions. *J. Geophys. Res.* 94, 7731–7748.
- Hiess, J., Condon, D.J., McLean, N., Noble, S.R., 2012. $^{238}\text{U}/^{235}\text{U}$ systematics in terrestrial uranium-bearing minerals. *Science* 335, 1610–1614.
- Hildreth, W., Wilson, C.J.N., 2007. Compositional zoning of the Bishop Tuff. *J. Petrol.* 48, 951–999.
- Hofmann, A.W., Jochum, K.P., 1996. Source characteristics derived from very incompatible trace elements in Mauna Loa and Mauna Kea basalts, Hawaii Scientific Drilling Project. *J. Geophys. Res.* 101, 11,831–11,839.
- Holtz, F., Behrens, H., Dingwell, D.B., Johannes, W., 1995. H_2O solubility in haplogranitic melts: Compositional, pressure, and temperature dependence. *Am. Mineral* 80, 94–108.
- Huang, H., Polat, A., Fryer, B.J., 2013. Origin of Archean tonalite–trondhjemite–granodiorite (TTG) suites and granites in the Fiskensset region, southern West Greenland: Implications for continental growth. *Gondwana Res.* 23, 452–470.
- Hurai, V., Paquette, J.L., Huraiová, M., Konečný, P., 2010. Age of deep crustal magmatic chambers in the intra-Carpathian back-arc basin inferred from LA-ICPMS U-Th-Pb dating of zircon and monazite from igneous xenoliths in alkali basalts. *J. Volcanol. Geotherm.* 198, 275–287.
- Ibrahim, S., Cosgrove, J., 2001. Structural and tectonic evolution of the Umm Gheig/El-Shush region, central Eastern Desert of Egypt. *J. Afr. Earth Sci.* 33, 199–209.
- Irber, W., 1999. The lanthanide tetrad effect and its correlation with K/Rb, Eu/Eu*, Sr/Eu, Y/Ho, and Zr/Hf of evolving peraluminous granite suites. *Geochem. Cosmochim. Acta* 63, 89–508.
- Irvine, T.N., Barager, W.R.A., 1971. A guide to the classification of the common volcanic rocks. *Can. J. Earth Sci.* 8, 523–548.
- Iwamori, H., 1997. Compression melting in subduction zones. *Terra Nova* 9, 9–13.
- Jackson, S.E., Pearson, N.J., Griffin, W.L., Belousova, E.A., 2004. The application of laser ablation-inductively coupled plasma-mass spectrometry to in situ U–Pb zircon geochronology. *Chem. Geol.* 211, 47–69.
- Jacobsen, S.B., Wasserburg, G.J., 1984. Sm–Nd isotopic evolution of chondrites and achondrites. II. *Earth Planet Sci. Lett* 67, 137–150.
- Jahn, B.M., Gikson, A.Y., Peucat, J.J., Hickman, A.H., 1981. REE geochemistry and isotopic data of Archean silicic volcanics and granitoids from the Pilbara Block, Western Australia: Implications for the early crustal evolution. *Geochem. Cosmochim. Acta* 45, 1633–1652.
- Jahn, B.M., Wu, F., Capdevila, R., Martineau, F., Zhao, Z., Wang, Y., 2001. Highly evolved juvenile granites with tetrad REE patterns: The Woduhe and Baerzhe granites from the Great Xing'an Mountains in NE China. *Lithos* 59, 171–198.
- James, R., Hamilton, D., 1969. Phase relations in the system $\text{NaAlSi}_3\text{O}_8$ – KAlSi_3O_8 – $\text{CaAl}_2\text{Si}_2\text{O}_8$ – SiO_2 at 1 kilobar water vapour pressure. *Contrib. Mineral. Petrol.* 21, 111–141.
- Jarrar, G.H., Theye, T., Yaseen, N., Whitehouse, M., Pease, V., Passchier, C., 2013. Geochemistry and P–T evolution of the Abu-Barqa Metamorphic Suite, SW Jordan, and implications for the tectonics of the northern Arabian–Nubian Shield. *Precambrian Res.* 239, 56–78.
- Johansson, Å., 2014. From Rodinia to Gondwana with the 'SAMBA' model – A distant view from Baltica towards Amazonia and beyond. *Precambrian Res.* 244, 226–235. <https://doi.org/10.1016/j.precamres.2013.10.012>.
- Johnson, P., Andresen, A., Collins, A., Fowler, A., Fritz, H., Ghebreab, W., Kusky, T., Stern, R., 2011. Late Cryogenian–Ediacaran history of the Arabian–Nubian Shield: A review of depositional, plutonic, structural, and tectonic events in the closing stages of the northern East African Orogen. *J. Afr. Earth Sci.* 61 (3), 167–232.
- Kay, S.M., Godoy, E., Kurtz, A., 2005. Episodic arc migration, crustal thickening, subduction erosion, and magmatism in the south-central Andes. *Geol. Soc. Am. Bull.* 117, 67–88.
- Keller, L.M., Wunder, B., Rhede, D., Abart, R., 2006. Experiments on the kinetics of the gabbro to eclogite transformation at 18 kbars and 700–900 °C. , conference: DMG LXXXIV, at Hannover, Germany. Volume: Beih. Z. Eur. J. Mineral. 18, 70.
- Khudeir, A.A., Abu, El-Rus M., Hoinkes, G., Mogessie, A., El-Gaby, S., 1996. Petrogenesis of the reversely zoned Akarem mafic-ultramafic intrusion, south Eastern Desert, Egypt. *Proc. Geol. Surv. Egypt, Centennial Conference*, pp. 447–464.
- Khudeir, A.A., Abu El-Rus, M.A., El-Gaby, S., El-Nady, O., 2006. Geochemical and geochronological studies on the infrastructural rocks of Meatiq and Hafafit Core Complexes, Eastern Desert, Egypt. *Egypt. J. Geol.* 50, 2006.
- Khudeir, A.A., Abu El-Rus, M.A., El-Gaby, S., El-Nady, O., Bishara, W.W., 2008. Sr–Nd isotopes and geochemistry of the infrastructural rocks in the Meatiq and Hafafit core complexes, Eastern Desert, Egypt: evidence for involvement of pre-Neoproterozoic crust in the growth of the Arabian–Nubian Shield. *Isl. Arc* 17, 90–108.
- Khudeir, A.A., Bishara, W.W., El-Tahlawi, M.R., Abu El-Rus, M.A., Bogdadi, G.Y., 2006. Wadi Beitan window in the south Eastern Desert of Egypt: Petrography, mineral chemistry and intensive properties of the Beitan gneisses. *Proc. 7th Int. Conf. Geochem.* 1, pp. 17–37.
- Klein, M., Stosch, H.G., Seck, H.A., 1997. Partitioning of high field-strength and rare-earth elements between amphibole and quartz-dioritic to tonalitic melts: An experimental study. *Chem. Geol.* 138, 257–271.
- Klemme, S., Blundy, J.D., Wood, B.J., 2002. Experimental constraints on major and trace element partitioning during partial melting of eclogite. *Geochem. Cosmochim. Acta* 66, 3109–3123.
- Greiling, R.O., Kröner, A., El-Ramly, M., Rashwan, A., 1988. Structural relationships between the southern and central parts of the Eastern Desert of Egypt: Details of a fold and thrust belt. In: El-Gaby, S., Greiling, R.O. (Eds.), *The Pan-African belt of northeast Africa and adjacent areas*. Vieweg & Sohn, Wiesbaden, pp. 121–146.
- Kusky, T., Matsah, M., 2003. Neoproterozoic Dextral Faulting on the Najd Fault System, Saudi Arabia, preceded sinistral faulting and escape tectonics related to closure of the Mozambique Ocean. In: Yoshida, M., Windley, B.F., Dasgupta, S., Powell, C. (Eds.), *Proterozoic East Gondwana: Supercontinent Assembly and Breakup*. Geol. Soc. Lond. Spec. Publ. 206, pp. 327–361.
- Laurie, A., Stevens, G., Van Hunen, J., 2013. The end of continental growth by TTG magmatism. *Terra Nova* 25, 130–136.
- Le Bas, M.J., Le Maitre, R.W., Streckeisen, A., Zanetti, B., 1986. A chemical classification of volcanic rocks based on the total alkalis-silica diagram. *Petrol.* 27, 745–750.
- Leeman, W.P., Hawkesworth, C.J., 1986. Open magma systems: trace element and isotopic constraints. *J. Geophys. Res.* 91, 5901–5912.
- Lemarchand, F., Villemant, B., Calas, G., 1987. Trace element distribution coefficients in alkali series. *Geochem. Cosmochim. Acta* 51, 1071–1081.
- Li, Z.X., Bogdanova, S.V., Collins, A.S., Davidson, A., De Waele, B., Ernst, R.E., Fitzsimons, I.C.W., Fuck, R.A., Gladkochub, D.P., Jacobs, J., Karlstrom, K.E., Lu, S., Natapov, L.M., Pease, V., Pisarevsky, S.A., Thrane, K., Vernikovsky, V., 2008. Assembly, configuration, and break-up history of Rodinia: A synthesis. *Precambrian Res.* 60, 179–210.
- Liew, T.C., McCulloch, M.T., 1985. Genesis of granitoid batholiths of Peninsular Malaysia and implications for models of crustal evolution: Evidence from a Nd–Sr isotopic and U–Pb, zircon study. *Geochem. Cosmochim. Acta* 49, 587–600.
- Linnen, R.L., Keppler, H., 1997. Columbite solubility in granitic melts: Consequences for the enrichment and fractionation of Nb and Ta in the Earth's crust. *Contrib. Mineral. Petrol.* 128, 213–227.

- Loizenbauer, J., Wallbrecher, E., Fritz, H., Neumayr, P., Khudeir, A., Kloetzli, U., 2001. Structural geology, single zircon ages and fluid inclusion studies of the Meatiq metamorphic core complex: Implications for Neoproterozoic tectonics in the Eastern Desert of Egypt. *Precambrian Res.* 110, 357–383.
- Ludwig, K.R., 2001. User's manual for Isoplot/Ex Version 2.49, a geochronological toolkit for Microsoft Excel. BGC Spec. Publ. 55 pp.
- Ludwig, K.R., 2003. User's manual for isoplot 3.00: A geochronological toolkit for Microsoft Excel. BGC Berkeley, CA, USA <https://searchworks.stanford.edu/view/6739593>.
- Lugmair, G.W., Marti, K., 1978. Lunar initial $^{143}\text{Nd}/^{144}\text{Nd}$: Differential evolution of the lunar crust and mantle. *Earth Planet. Sci. Lett.* 39, 349–367.
- Maaløe, S., Wyllie, P.J., 1975. Water content of a granite magma deduced from the sequence of crystallization determined experimentally with water-undersaturated conditions. *Contrib. Mineral. Petrol.* 52, 175–191.
- Maniar, P.D., Piccoli, P.M., 1989. Tectonic discrimination of granitoids. *Geol. Soc. Am. Bull.* 101, 635–643.
- Martin, H., 1986. Effect of steeper Archean geothermal gradient on geochemistry of subduction zone magmas. *Geology* 14, 753–756.
- Martin, H., 1995. The Archean grey gneisses and the genesis of the continental crust. In: Condie, K.C. (Ed.), *The Archean crustal evolution*. Elsevier, Amsterdam, pp. 205–259.
- Martin, H., 1999. Adakitic magmas: Modern analogues of Archean granitoids. *Lithos* 46, 411–429.
- Martin, H., Moyen, J.F., 2002. Secular changes in tonalite–trondhjemite–granodiorite composition as markers of the progressive cooling of Earth. *Geology* 30, 319–322.
- Martin, H., Moyen, J.F., Guitreau, M., Blichert-Toft, J., Le Pennec, J.L., 2014. Why Archean TTG cannot be generated by MORB melting in subduction zones. *Lithos* 198–199, 1–13.
- Martin, H., Smithies, R.H., Rapp, R., Moyen, J.F., Champion, D., 2005. An overview of adakite, tonalite–trondhjemite–granodiorite (TTG), and sanukitoid: Relationships and some implications for crustal evolution. *Lithos* 79, 1–24.
- McCulloch, M.T., Chappell, B.W., 1982. Nd isotopic characteristics of S- and I-type granites. *Earth and Planetary Science Letters* 58, 51–64.
- McDonough, W.F., Sun, S.S., 1995. The composition of the earth. *Chem. Geol.* 120, 223–253.
- McGuire, A.V., Stern, B., 1993. Granulite xenoliths from western Saudi Arabia: The lower crust of the late Precambrian Arabian-Nubian Shield. *Contrib. Mineral. Petrol.* 114, 395–408.
- McMillan, P.F., Holloway, J.R., 1987. Water solubility in aluminosilicate melts. *Contrib. Mineral. Petrol.* 97, 320–332.
- Middleburg, J.J., Van der Weijden, C.H., Woittiez, J.R.W., 1988. Chemical processes affecting mobility of major, minor and trace elements weathering of granitic rocks. *Chem. Geol.* 68, 253–273.
- Milisenada, C.C., Liew, T.C., Hofmann, A.W., Köhler, H., 1994. Nd isotopic mapping of the Sri Lanka basement: Update, and additional constraints from Sr isotopes. *Precambrian Res.* 66, 95–110.
- Miller, C.F., Meschter-McDowell, S., Mapes, R.W., 2003. Hot and cold granites? Implications of zircon saturation temperatures and preservation of inheritance. *Geology* 31, 529–532.
- Moyen, J.-F., Laurent, O., Chelle-Michou, C., Couzinié, S., Vanderhaeghe, O., Zeh, A., Villaras, A., Gardien, V., 2017. Collision vs. subduction-related magmatism: Two contrasting ways of granite formation and implications for crustal growth. *Lithos* 277, 154–177.
- Moyen, J.F., Stevens, G., 2006. Experimental constraints on TTG petrogenesis: Implications for Archean geodynamics. In: Benn, K., Mareschal, J.C., Condie, K.C. (Eds.), *Archean geodynamics and environments*. 164. AGU, pp. 149–175.
- Müller, A., Thomas, R., Wiedenbeck, M., Seltmann, R., Breiter, K., 2006. Water content of granitic melts from Cornwall and Erzgebirge: A Raman spectroscopy study of melt inclusions. *Eur. J. Mineral.* 18, 429–440.
- Nash, W.P., Crecraft, H.R., 1985. Partition coefficients for trace elements in silicic magmas. *Geochim. Cosmochim. Acta.* 49, 2,309–2,322.
- O'Conner, J.T., 1965. A classification for quartz-rich igneous rocks based on feldspar ratios. *U.S. Geol. Surv. Prof. Pap.* 525, 79–84.
- Paoli, G., Dini, A., Petrelli, M., Rocchi, S., 2019. HFSE-REE Transfer Mechanisms During Metasomatism of a Late Miocene Peraluminous Granite Intruding a Carbonate Host (Campiglia Marittima, Tuscany). *Minerals* 9. <https://doi.org/10.3390/min9110682>.
- Paquette, J.L., Médard, E., Francomme, J., Bachèlery, P., Hénot, J.M., 2019. LA-ICP-MS U/Pb zircon timescale constraints of the Pleistocene latest magmatic activity in the Sancy stratovolcano (French Massif Central). *J. Volcanol. Geotherm.* 374, 52–61.
- Paquette, J.L., Piro, J.L., Devidal, J.L., Bosse, V., Didier, A., 2014. Sensitivity enhancement in LA-ICP-MS by N₂ addition to carrier gas: application to radiometric dating of U-Th-bearing minerals. *Agilent ICP-MS J.* 58, 4–5.
- Patiño Douce, A.E., 2005. Vapor-Absent Melting of Tonalite at 15–32 kbar. *J. Petrol.* 46, 275–290.
- Peacock, S.M., Rushmer, T., Thompson, A.B., 1994. Partial melting of subducting oceanic crust. *Earth Planet. Sci. Lett.* 121, 227–244.
- Pearce, J.A., Harris, N.B.W., Tindle, A.G., 1984. Trace element discrimination diagrams for the tectonic interpretation of granitic rocks. *J. Petrol.* 25, 956–983.
- Pearce, J.A., Norry, M.J., 1979. Petrogenetic implications of Ti, Zr, Y, Nb variations in volcanic rocks. *Contrib. Mineral. Petrol.* 69, 33–47.
- Petford, N., Atherton, M., 1996. Na-rich partial melts from newly underplated basaltic drust: The Cordillera Blanca Batholith. *Peru. J. Petrol.* 37, 1491–1521.
- Pisarevsky, S., Murphy, J., Cawood, P., Collins, A., 2008. Late Neoproterozoic and Early Cambrian palaeogeography: Models and problems. *Geol. Soc. Lond. Spec. Publ.* 294, 9–31.
- Qian, Q., Hermann, J., 2013. Partial melting of lower crust at 10–15 kbar: Constraints on adakite and TTG formation. *Contrib. Mineral. Petrol.* 165, 1195–1224.
- Rapp, R.P., Shimizu, N., Norman, M.D., 2003. Growth of early continental crust by partial melting of eclogite. *Nature* 425, 605–609.
- Rapp, R.P., Watson, E.B., Miller, C.F., 1991. Partial melting of amphibolite/eclogite and the origin of Archean trondhjemites and tonalites. *Precambrian Res.* 51, 1–25.
- Robinson, F.A., Foden, J.D., Collins, A.S., 2015a. Geochemical and isotopic constraints on island arc, synorogenic, post-orogenic and anorogenic granitoids in the Arabian Shield, Saudi Arabia. *Lithos* 220–223, 97–115.
- Robinson, F.A., Foden, J.D., Collins, A.S., 2015b. Zircon geochemical and geochronological constraints on contaminated and enriched mantle sources beneath the Arabian Shield, Saudi Arabia. *J. Geol.* 123, 463–489.
- Rooney, T.O., Morell, K.D., Hidalgo, P., Fraceschi, P., 2015. Magmatic consequences of the transition from orthogonal to oblique subduction in Panama. *Geochim. Geophys. Geosy.* 16, 4178–4208.
- Rudnick, R.L., Fountain, D.M., 1995. Nature and composition of the continental crust: A lower crustal perspective. *Rev. Geophys.* 33, 267–309.
- Schöpa, A., Annen, C., 2013. The effects of magma flux variations on the formation and lifetime of large silicic magma chambers. *J. Geophys. Res.* 118, 926–942.
- Seyler, M., Bonatti, E., 1988. Petrology of a gneiss-amphibolite lower crustal unit from Zabargad Island, Red Sea. *Tectonophysics* 150, 177–207.
- Simonetti, A., Neal, C.R., 2010. In-situ chemical, U-Pb dating, and Hf isotope investigation of megacrystic zircons, Malaita (Solomon Islands): Evidence for multi-stage alkaline magmatic activity beneath the Ontong Java Plateau. *Earth Planet. Sci. Lett.* 295, 251–261.
- Sláma, J., Košler, J., Condon, D.J., Crowley, J.L., Gerdes, A., Hanchar, J.M., Horstwood, M.S.A., Morris, G.A., Nasdala, L., Norberg, N., Schaltegger, U., Schoene, B., Tubrett, M.N., Whitehouse, M.J., 2008. Plešovice zircon - A new natural reference material for U-Pb and Hf isotopic microanalysis. *Chem. Geol.* 249, 1–35.
- Smithies, R.H., 2000. The Archean tonalite–trondhjemite–granodiorite (TTG) series is not an analogue of Cenozoic adakite. *Earth Planet. Sci. Lett.* 182, 115–125.
- Sparks, R., Marshall, L., 1986. Thermal and mechanical constraints on mixing between mafic and silicic magmas. *J. Volcanol. Geotherm. Res.* 29, 99–124.
- Stern, C.R., Kilian, R., 1996. Role of the subducted slab, mantle wedge and continental crust in the generation of adakites from the Andean Austral Volcanic Zone. *Contrib. Mineral. Petrol.* 123, 263–281.
- Stern, R., 1985. The Najd fault system, Saudi Arabia and Egypt: A late Precambrian rift-related transform system? *Tectonics* 4, 497–511.
- Stern, R.J., 2002. Subduction zones. *Rev. Geophys.* 40, 3.1–3.38.
- Sun, S., McDonough, W.F., 1989. Chemical and isotopic systematics of oceanic basalts: Implications for mantle composition and processes. In: Saunders, A.D., Norry, M.J. (Eds.), *Magmatism in the ocean basins*. *Geol. Soc. Lond. Spec. Publ.* 42, pp. 313–345.
- Tartèse, R., Boulvais, P., 2010. Differentiation of peraluminous leucogranites “en route” to the surface. *Lithos* 114, 353–368.
- Tatsumi, Y., 1989. Migration of fluid phases and genesis of basalt magmas in subduction zones. *J. Geophys. Res.* 94, 4697–4707.
- Thompson, A.B., 2001. Partial melting of metavolcanics in amphibolite facies regional metamorphism. *Proc Indian Acad Sci, Earth Planet Sci* 110, 287–291.
- Tiepolo, M., Bottazzi, P., Foley, S.F., Oberti, R., Zanetti, A., 2001. Fractionation of Nb and Ta from Zr and Hf at mantle depths: The role of titanite–pargasite and kaersutite. *J. Petrol.* 42, 221–232.
- Van Kranendonk, M.J., 2010. Two types of Archean continental crust: Plume and plate tectonics on early earth. *Am. J. Sci.* 310, 1187–1209.
- Villa, I.M., De Bièvre, P., Holden, N.E., Renne, P.R., 2015. IUPAC-IUGS recommendation on the half-life of ^{87}Rb . *Geochim. Cosmochim. Acta* 164, 382–385.
- Watkins, J.M., Clemens, J.D., Treloar, P.J., 2007. Archean TTGs as sources of younger granitic magmas: Melting of sodic metatonalites at 0.6–1.2 GPa. *Contrib. Mineral. Petrol.* 154, 91–110.
- Watson, E.B., 1979. Zircon saturation in felsic liquids: Experimental data and applications to trace element geochemistry. *Contrib. Mineral. Petrol.* 70, 407–419.
- Watson, E.B., Harrison, T.M., 1984. Accessory minerals and the geochemical evolution of crustal magmatic systems: A summary and prospectus of experimental approaches. *Phys. Earth Planet. In.* 35, 19–30.
- Weaver, B.L., Tarney, J., 1983. Elemental depletion in Archean granulite facies rocks. In: Atherton, M.P., Gribble, C.D. (Eds.), *Migmatite, Melting and Metamorphism*. Nantwich, Shiva, pp. 250–263.
- Wiedenbeck, M., Allé, P., Corfu, F., Griffin, W.L., Meier, M., Oberli, F., von Quadt, A., Roddick, J.C., Spiegel, W., 1995. Three natural zircon standards for U-Th-Pb, Lu-Hf, trace element and REE analyses. *Geostandard Newslett.* 19, 1–23.
- Winther, K.T., 1996. An experimentally based model for the origin of tonalitic and trondhjemitic melts. *Chem. Geol.* 127, 43–59.
- Wolde, B., Team, G.G.G., 1996. Tonalite–trondhjemite–granite genesis by partial melting of newly underplated basaltic crust: An example from the Neoproterozoic Birbir magmatic arc, western Ethiopia. *Precambrian Res.* 76, 3–14.
- Wolf, M.B., Wyllie, P.J., 1989. The formation of tonalitic liquids during the vapor-absent partial melting of amphibolite at 10 kb. *Trans. Am. Geophys. Union (EOS)* 70, 506.
- Wolf, M.B., Wyllie, P.J., 1994. Dehydration melting of amphibolite at 10 kbar: The effects of temperature and time. *Contrib. Mineral. Petrol.* 115, 369–383.
- Wyman, D.A., Hollings, P., Biczok, J., 2011. Crustal evolution in a cratonic nucleus: Granitoids and felsic volcanic rocks of the North Caribou Terrane, Superior Province Canada. *Lithos* 123, 37–49.
- Yarmolyuk, V.V., Kovach, V.P., Kozakov, I.K., Kozlovsky, A.M., Kotov, A.B., Rytsk, E.Yu., 2012. Mechanisms of continental crust formation in the Central Asian foldbelt. *Geotectonics* 46, 251–272.
- Zamora, D., 2000. Fusion de la croûte océanique subductée: approche expérimentale et géochimique. Ph.D. dissertation. Université Blaise Pascal, Clermont-Ferrand, France 248 pp.

- Zhai, M.G., 2011. Cratonization and the Ancient North China Continent: A summary and review. *Sci. China Earth Sci.* 54, 1110–1120.
- Zhang, C.L., Li, H.K., Santosh, M., Li, Z.X., Zou, H.B., Wang, H., Ye, H., 2012. Precambrian evolution and cratonization of the Tarim Block, NW China: Petrology, geochemistry, Nd-isotopes and U–Pb zircon geochronology from Archaean gabbro-TTG–potassic granite suite and Paleoproterozoic metamorphic belt. *J. Asian Earth Sci.* 47, 5–20.
- Zhang, S.B., Zheng, Y.F., Zhao, Z.F., Wu, Y.B., Yuan, H., Wu, F.Y., 2009. Origin of TTG-like rocks from anatexis of ancient lower crust: Geochemical evidence from Neoproterozoic granitoids in South China. *Lithos* 113, 347–368.